Combinatorial and Off-Shell Effects in New Physics Cascades

Dissertation

zur Erlangung des Doktorgrades

des Department Physik

der Universität Hamburg

vorgelegt von

Daniel Wiesler
aus
Offenburg

Hamburg
2012

Gutachter der Dissertation:	Dr. Jürgen Reuter
	Prof. Dr. Gudrid Moortgat-Pick
Gutachter der Disputation:	Dr. Jürgen Reuter
	Prof. Dr. Peter Schleper
Datum der Disputation:	15.10.2012
Vorsitzender des Prüfungsausschusses:	Prof. Dr. Günter Sigl
Vorsitzender des Promotionsausschusses:	Prof. Dr. Peter Hausschildt
Dekan des Fachbereichs Physik:	Prof. Dr. Heinrich Graener

"If we take everything into account, not only
what the ancients knew, but all of what we know
today that they didn't know, then I think that
we must frankly admit that we do not know."
Richard P. Feynman

Abstract

Up to now, the Standard Model of elementary particle physics is in very good agreement with most data. However, it has various shortcomings which motivate the presence of new physics at the TeV scale. The first major step following a potential discovery of new particles at the Large Hadron Collider (LHC) is the determination of their intrinsic properties, foremost masses and spins. Event topologies of new physics signals with a conserved parity motivated by precision data and the dark matter paradigm require for sophisticated measurement procedures, which have been developed in recent years. These techniques often rely on simplifying assumptions, albeit they need not necessarily be fulfilled. In this thesis we investigate the impact of combinatorial and off-shell effects on new physics cascades in three different contexts. A detailed understanding of these effects is essential for the topic of model parameter determination of new physics signatures at the LHC. First, we study the non-resonant contributions of a broad gluino on mass and spin measurements as a prime example for the importance of off-shell effects. A phenomenological scan over the gluino's width-to-mass ratio yields a severe smearing of invariant mass distributions and as a consequence thereof drastically shifted endpoint positions. Spin determinations, on the other hand, are barely affected and a model discrimination of the two prime candidates SUSY and UED is not at risk. In the second part, we assess the feasibility of the gluino dijet endpoint measurement in three fully inclusive scenarios at the LHC to investigate the impact of combinatorial and SUSY backgrounds on its precise determination. We develop a method to disentangle two major signal contributions and extract their associated edges with good accuracy. For this we use existent kinematic variables and propose new ones to overcome the former's deficiencies. The last part governs the issue of so-called 'fake combinatorics', where distorted mass edges originate from additional particles with non-standard quantum numbers instead of false assignments of decay configurations. We study the contributions of exotic fermions within standard SUSY cascades, highlight their impact on affected invariant mass variables and discuss how their presence may be distinguished from ordinary, plain SUSY signals.

Zusammenfassung

Das Standardmodell der Elementarteilchenphysik stimmt bisher sehr gut mit den meisten gemessenen Daten überein. Es hat jedoch mehrere Unzulänglichkeiten, welche die Existenz neuer Physik an der TeV Skala implizieren. Der erste große Schritt nach einer Entdeckung neuer Teilchen ist die Bestimmung ihrer spezifischen Eigenschaften, allen voran Masse und Spin. Die Ereignistopologien von Signalen neuer Physik mit erhaltener Parität, begründet durch Präzisionsmessungen und die Existenz Dunkler Materie, benötigen ausgefeilte Messmethoden, welche in den letzten Jahren entwickelt wurden. Allerdings basieren diese Techniken oft auf vereinfachenden Annahmen, die nicht notwendigerweise erfüllt sein müssen. In der vorliegenden Arbeit wird der Einfluss von kombinatorischen und off-shell Effekten auf Zerfallskaskaden neuer Physik in drei unterschiedlichen Zusammenhängen untersucht. Ein genaues Verständnis dieser Effekte ist essentiell für die Modellparameterbestimmung von Signaturen neuer Physik am LHC. Zunächst werden die Effekte von off-shell Beiträgen eines breiten Gluinos auf Massen- und Spin-Messungen als Musterbeispiel für die Wichtigkeit von off-shell Effekten analsyiert. Ein phänomenologischer Scan des Breite-zu-Masse Verhältnisses des Gluinos ergibt eine starke Verschmierung von invarianten Massenverteilungen und als Konsequenz dessen drastisch verschobene Endpunktpositionen. Spinbestimmungen sind andererseits kaum betroffen und eine Modellunterscheidung zwischen den zwei Paradebeispielen SUSY und UED ist nicht in Gefahr. Im zweiten Teil wird die Möglichkeit der Gluino Dijet Endpunktmessung in drei inklusiven Szenarien am LHC abgeschätzt um den Einfluss von kombinatorischen und supersymmetrischen Untergründen zu untersuchen. Eine Methode zur Trennung des Signals in zwei Hauptbestandteile wird entwickelt und die dazugehörigen Endpunkte werden mit großer Genauigkeit bestimmt. Aus diesem Grund benutzen wir existierende kinematische Variablen und führen neue ein, um die Nachteile der vorhergehenden zu überwinden. Der letzte Teil handelt von falscher Kombinatorik, wenn verzerrte Massenkanten von zusätzlichen Teilchen mit ungewöhnlichen Quantenzahlen, anstelle von falschen Zuordnungen von Zerfallskonstellationen, herrühren. Die Beiträge exotischer Fermionen in normalen SUSY Kaskaden werden untersucht, ihr Einfluss auf betroffene invariante Massenvariablen wird herausgestellt und es wird diskutiert, wie ihre Präsenz von gewöhnlichen SUSY Signalen unterschieden werden kann.

Contents

Chapter 1

Introduction

The Standard Model (SM) of elementary particle physics [1, 2, 3] is an extraordinary successful effective quantum field theory with an experimental validation covering more than twelve orders of magnitude ranging from a few electronvolt to energies above the Z boson mass [4, 5]. Moreover, its remarkable success is demonstrated by precision measurements conducted at the LEP collider at CERN and Tevatron at Fermilab, which confirm theoretical predictions well beyond leading order. The very recent discovery of a novel particle at the LHC [6, 7], supposedly the highly anticipated Higgs boson [8, 9, 10], further supports the SMs framework of electroweak symmetry breaking. In spite of these triumphs the SM has several shortcomings obstructing its existence as a truly fundamental theory.

One deficit is the missing incorporation of neutrino masses. Empiric evidence of solar and atmospheric neutrinos is subject to oscillations and hence requires non-vanishing masses not accounted for in the SM. However, the inclusion of neutrino masses is possible in minimal extensions. Another fundamental downside is the failure to include gravity. While the SM is tested to be valid up to the TeV range, gravity is known to become relevant at the latest at the Planck scale $\Lambda_P \sim 10^{19}$ GeV. A unification of all four interactions in terms of a renormalisable theory is yet to be accomplished.

Further evidence for the deficiency of the SM originate from astrophysical observations and cosmological considerations. Anisotropies of the cosmic microwave background [11, 12], deviations of observed and expected rotational curves of galaxies and results from gravitational micro lensing [13] are all interpreted as a result of

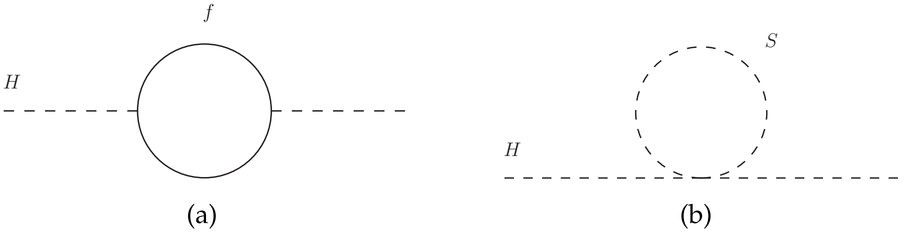

Figure 1.1: Feynman diagram of one-loop contribution to the physical Higgs mass parameter from a fermion f (a) and a scalar S (b).

invisible non-relativistic matter, to be referred to as cold dark matter. Unfortunately, all these observations are in conflict with the SMs predictions. In fact, the SM has no candidate to account for cold dark matter[1] preferred by data.

In addition there exist aesthetic objections of a more theoretical kind. Two questions of fundamental nature not addressed by the SM are 'What is the reasoning behind the particular choice of gauge groups and particle content?' and 'Why are there three generations of fermions and where does their mass hierarchy stem from?'.

One of the major issues however is the *hierarchy problem* or the mere question 'Why is the physical Higgs-mass a parameter at the electroweak scale and not at the Planck scale?'. Quantum corrections of the squared Higgs mass are dominated by contributions from the top quark (cf. Figure 1.1 (a)) which to first order is given by

$$\Delta m_H^2 = -\frac{|\lambda_f|^2}{8\pi^2}\Lambda_{\text{eff}}^2 + \mathcal{O}(\ln\Lambda) \tag{1.1}$$

where λ_f corresponds to the top Yukawa coupling. The cutoff scale Λ_{eff}, introduced to regularise the divergent loop integral, has a natural upper limit given by the Planck scale Λ_P. This allows for a twofold interpretation. On the one hand, the quadratic divergence in (1.1) results in a vast tension of the physical and bare Higgs mass parameter for high values of $\Lambda_{\text{eff}} \gg$ TeV: the stability of the observable Higgs mass at the electroweak scale requires an enormous amount of *fine-tuning* over many orders of magnitude. On the other hand, this argument may be turned upside down in that the SM as an effective theory remains valid up to no more than a few TeV implying new physics possibly in reach of present and future experiments.

The hierarchy problem in particular has inspired many theorists to study mecha-

---

[1] SM neutrinos constitute a candidate for *hot* dark matter due to their ultrarelativistic nature, which is not able to explain all of the observed phenomena.

nisms circumventing the unappealing aspect of fine-tuning. The introduction of new symmetries with associated particles is one potential option to stabilize the Higgs mass. A global symmetry and new particles that cancel the divergences to first order are introduced in the so-called Little Higgs models [14, 15]. Unfortunately, since the divergences reappear at higher orders, these models are still effective theories and merely shift the problem to a slightly larger scale. A more prominent example of a new symmetry that cancels the quadratic divergences to all orders is Supersymmetry (SUSY) [16, 17, 18].

In a nutshell, SUSY relates bosonic and fermionic degrees of freedom through a symmetry transformation generated by spinorial super-charges Q_a, which constitute the most general extension of the Poincaré algebra [19]. Apart from this beautiful fundamental technicality, the hierarchy problem is tackled in a very elegant way: the devastating quadratic divergences in the top quark contributions of the Higgs mass corrections in equation (1.1) are cancelled to all orders by contributions from its scalar counterparts. For instance, at the one-loop level there is a contribution, depicted in Figure 1.1 (b), that reads

$$\Delta m_H^2 = \frac{\lambda_s}{16\pi^2}\Lambda_{\text{eff}}^2 + \mathcal{O}(\ln\Lambda) \tag{1.2}$$

and, hence, equals the contribution of the contribution of the top quark from equation (1.1) provided that $\lambda_s = |\lambda_f|^2$ for the associated dimensionless couplings λ_s and λ_f. Fortunately, this identity is precisely what is predicted by SUSY. However, since up to now superpartners, i.e. the supersymmetric versions of SM particles, have not been observed, SUSY has to be a broken symmetry. Even though only little is known about the actual breaking mechanism[2], it is due to the equality of couplings, which has to persist in order for the cancelation to stay valid, that SUSY must be *softly* broken. More precisely, the quadratic divergences of the Higgs mass corrections are only cancelled up to a factor

$$\Delta m_H^2 \sim m_{\text{soft}}^2 \cdot \ln\left(\Lambda_{\text{eff}}/m_{\text{soft}}\right). \tag{1.3}$$

From this it is obvious that the general superpartner mass scale m_{soft} should not be too large so as not to reintroduce another *little* hierarchy [21]. In fact, the *naturalness* of the theory, which so far is only slightly threatened by moderate superpartner exclusion bounds, motivates the perpetuating vast anticipation to observe experimental

---

[2] for a review of SUSY breaking mechanisms, see e.g. [20].

signatures of supersymmetric nature in the near future at the Large Hadron Collider (LHC).

Alternative, more radical scenarios impose a deeper connection of electroweak and gravitational forces through the existence of extra spatial compact dimensions[3]. In one of those models the large volume of the extra dimension(s) ensures the link of a higher-dimensional theory and the four-dimensional effective theory, where only the gravitational fields are allowed to propagate in all dimensions (i.e. the bulk), while all SM gauge fields are confined to our three-dimensional world [24, 25, 26]. In sum, gravity becomes important at the scale of the extra dimension $\Lambda_D \ll \Lambda_P$ rendering the fine-tuning problem obsolete for $\Lambda_D \sim \mathcal{O}(\text{TeV})$. On the other hand this implies the presence of gravitational effects, black hole production and signatures of Kaluza-Klein (KK) excitations [27, 28] of SM fields at the TeV scale and hence possibly at the LHC.

Higher-dimensional theories in which all SM fields reside in the bulk are generally referred to as *universal* extra dimensions (UED) [29, 30, 31]. In these scenarios an unbroken discrete $\mathbb{Z}_2$ symmetry, the so-called KK-parity, requires TeV-scale KK-resonances to be produced in pairs and forbids tree-level contributions to electroweak precision observables. Besides these vital phenomenological consequences to be discussed in more detail shortly, it may furthermore be possible to achieve electroweak symmetry breaking without the need of massive fine-tuning through a bound-state Higgs doublet in six dimensions [32].

Many of these scenarios beyond the SM (BSM) predict plenty of new particles. In this thesis, their appearance will be studied in terms of rich production and decay patterns in a comprehensive LHC environment. Hence, in the following relevant key aspects of hadron collider physics are briefly reviewed to set the framework for a detailed discussion of new physics signatures at the LHC.

1.1 Physics in an LHC Environment

The Large Hadron Collider is the largest particle physics experiment to date delivering proton-proton collisions at an unprecedented centre-of-mass energy of currently

---

[3] Comprehensive reviews may be found in [22, 23], which concern both model building as well as phenomenological aspects of various extra-dimensional models.

$\sqrt{s} = 8$ TeV with future prospects of up to $\sqrt{s} = 14$ TeV. Four experiments (ALICE, ATLAS, CMS and LHCb) perform a large variety of physics programs. So far, the tremendous efforts of the collaborations from the two big multipurpose experiments ATLAS and CMS result in a validation of the SMs predictions to an astonishing degree. The recently found evidence of a novel boson further emphasizes the outstanding performance of the much-heralded discovery-machine. These achievements are all the more impressive considering the circumstances of a contaminated hadron collider environment under which physics analyses are undertaken.

In a proton-proton collider, one particular specialty is the intrinsic lack of knowledge of the actual hard interaction and its exact kinematics. The colliding proton constituents i inherit only a fraction x_i of the initial beam momentum which yields an a priori unknown reduced center-of-mass (CM) energy $\hat{s} = x_1 x_2 s$. The resulting CM frame of the main interaction is boosted along the beam axis z with respect to the lab frame and the momentum in this direction is not conserved. Hence at the LHC many quantities of relevance are defined in the transverse plane in which momentum conservation is valid. Simple examples of this are the transverse momenta p_T and energies E_T as well as a more prominent candidate: the missing transverse energy $\not{E}_T$, sometimes loosely referred to as missing energy. It is typically defined as the vectorial sum of the transverse momenta of all visible final state objects in the detector:

$$\not{E}_T = \sum_i \vec{p}_T^{(i)}. \tag{1.4}$$

Further transverse observables of this type are e.g. H_T, m_T or M_{T2}, which will be defined later on where needed.

The key feature of LHC physics is its coloured nature. It again starts with the hard interaction which is initiated by colliding quarks or gluons from the proton. Except for some very rare cases, most outgoing particles carry colour charge as well, either from the hard process itself or from additional radiation off coloured partons beforehand or afterwards. Due to the kinematics of massless particles, these radiations are enhanced in the soft and collinear regime of the firstly produced parton[4] and will effectively yield a certain 'spray' of coloured particles centered around the initiator. Since confinement tells us that no isolated colour-charged particle may be observed, the procedure of fragmentation results in a great number of baryons and

---

[4] In fact, in the exact matrix element calculation there are two singularities for both these regimes which have to be regularised.

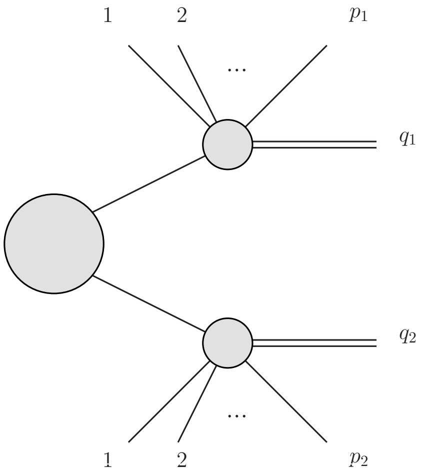

Figure 1.2: Generic event topology of models with conserved discrete parity. Two novel particles with odd parity eigenvalue are pair produced and cascade decay down to an invisible dark matter candidate q_i (denoted by double lines) accounting for p_i visible particle along the way.

mesons which, after further eventual decays, are the *final* particles in the detector.

To be able to make conclusive statements about the underlying hard physics process, the observable particle 'spray' has to be dealt with in a well-defined way. This is accomplished by so-called jet algorithms which collect sets of particles within a predefined distance and transverse momentum or energy to return a single four-momentum object. These *jets* ideally correspond to the original first partons from the hard interaction. Naturally, this is not necessarily always the case and a mismatch of this kind is not an unusual source of error at the LHC.

Although this is a rather short summary of a very comprehensive field, with this outline we lay the foundation for the upcoming discussions of new physics signatures in a hadron collider environment.

1.2 Discrete Parities and Dark Matter

Many models of new physics beyond the SM are augmented by discrete $\mathbb{Z}_2$ symmetries. While in some scenarios the introduction of those is rather ad hoc, in others they follow from cardinal underlying assumptions. Unlike in the SM, its minimal supersymmetric extension (MSSM), maybe the most prominent SUSY example, allows for multiple baryon- and lepton-number violating terms in the most general renormalisable and gauge invariant superpotential[5]. Taking into account constraints from experimental observations, some of these interactions have to be forbidden or at least severely suppressed[6]. More elegantly, the introduction of a $\mathbb{Z}_2$ symmetry, better known as R-parity [35], naturally helps to protect the model from such phenomenologically disastrous operators. On the contrary in models of UED with $n = 4 + \delta$ dimensions, δ-momentum conservation of particles confined to the extra dimensions inevitably implies the conservation of the KK-number or KK-parity in the resulting effective four-dimensional theory. Although the origin of R-parity on the one hand and KK-parity on the other hand is fundamentally different, the drastic phenomenological consequences are common to both: since the usual SM matter content is P-even, where P is either R or KK, novel P-odd particles are produced in pairs and cascade decay down to the lightest P-odd particle (LPP) which, if electrically neutral, is a stable and hence viable dark matter candidate. A generic event topology of this type with long decay chains, many final state particles and missing energy due to the LPP is depicted in Figure 1.2. In most SUSY scenarios the LPP (=LSP, lightest supersymmetric particle) is represented by the lightest neutralino $\tilde{\chi}_1^0$ which, depending upon the soft SUSY breaking mechanism, is a mass-eigenstate constructed from a super-position of the super-partners of Higgs and gauge bosons. In UED models, in contrast, the LPP (=LKP, lightest KK particle) is usually given by the first excitation of the photon $\gamma^{(1)}$. The presence of these invisible dark matter candidates is the reason for the inability to reconstruct the full four-momentum of the initially produced particles at the LHC. Instead, all available information is encoded in the visible decay products emitted along the way down the cascade.

Striking similarities of the two scenarios with discrete parities and a phenomenology that closely resembles each other raise the essential question whether SUSY and UED may be distinguished in an experimental setting at the LHC. The basis for this kind of model discrimination is the determination of fundamental parameters, i.e. masses, spins and couplings. Mass measurements are often considered to be the first step on this way. In supersymmetric theories our lack of knowledge of the underlying SUSY breaking mechanism and thus of the scale of superpartner masses is parameterised through soft-breaking terms [36, 37, 38, 21] while in models of UED the situa-

---

[5] For an introduction to the MSSM and a more comprehensive discussion of SUSY phenomenology, we refer the reader to e.g. [21, 33, 34].

[6] The simultaneous presence of baryon- *and* lepton-number violating terms allows for couplings that mediate a potential decay of the proton in contradiction to its observed stability. Hence, these couplings either have to vanish or they have to be suppressed by many orders of magnitude.

tion is more comfortable in that the masses of all KK-resonances are tightly linked to the compactification scale [29, 30]. Even though in general this amounts to UED mass spectra of near degeneration, in principle it is feasible to have mass patterns in both models that are either completely dissimilar or very much alike. Hence, discriminating these fundamentally different models with similar phenomenology by means of mass determination methods is not viable. This comes about due to the fact that most of these approaches solely rely on endpoints of invariant mass distributions which do not differ if the masses of the models are the same.

On the contrary to these masses which are free parameters in most models, spins of novel SM partners are in general completely determined by underlying model assumptions. By the very nature of SUSY, the superpartners of the SM particle content differ in spin by exactly one half from their SM counterparts: all SM fermions are accompanied by scalars and the gauge and Higgs bosons acquire new fermionic partners with spin 1/2. In the case of UED, the spin of the KK-resonances is equal to the spin of the KK zero-modes which amount to the usual matter, much the same as it is for the different generations in the SM. In particular this difference in spin assignments bears the opportunity to disentangle the signatures of these two scenarios using spin-sensitive observables such as shape asymmetries of invariant mass distributions [39, 40, 41], angular correlations [41, 42, 43] or simply the cross-section itself [44]. The last point might also help shed light upon the last missing piece necessary to gain full knowledge of the underlying model: the precise determination of all couplings, which however will not be addressed any further here. Finally, it is of utmost importance to get a handle on the characteristics of the lightest P-odd particle for another reason: spin measurements at the LHC or a future Linear Collider (LC) possess the discriminative power to tell apart scenarios where the dark matter candidate is either a scalar, a fermion or even a vector and hence they constitute a vital tool in the physics quest of the hunt for dark matter.

1.3 Motivation and Outline

In new physics events with a conserved parity and a lot of transverse missing energy only a fraction of the entire information is concealed within multiple visible decay products, the momenta of which are used for mass and spin measurements. However, many obstacles may emerge between the initial production and the final measurement. For one thing, the simulation of new physics events is a complicated process that involves many computationally intensive steps. Due to the high multiplicity of final state particles a full matrix-element calculation of the complete process is beyond the computational possibilities. Hence, these comprehensive processes have to be factorised into production and decay using the Narrow-Width Approximation (NWA), whether or not necessary prerequisites for its application are fulfilled. The most trivial of these conditions is a small width: a priori it is not clear to what extent a 'broad' new resonance with substantial off-shell contributions affects spin and mass measurements, specifically since the NWA is known to break down in such scenarios [45, 46].

Furthermore, various methods for mass measurements rely on the existence of an exclusive particular decay cascade in order to be successfully applied. Most of them neglect the general inclusive nature of new physics signatures and backgrounds in a hadron collider environment. Let us consider a characteristic SUSY example to emphasize the importance of this point: if we were to build an invariant mass of two jets supposedly originating from a gluino decay in inclusive SUSY event samples with more than six jets, how do we know which combination to pick? While only one *true* choice reproduces the desired correlation and gluino endpoint information, all other connections are considered to be false and thus *backgrounds*. Possible origins of those supplemental interfering jets are initial and final state radiation as well as superpartners other than the desired one (i.e. gluino) either from additional SUSY processes or different decay steps down the cascade. These so-called combinatorial and SUSY backgrounds severely affect the measurements through a considerable smearing of endpoint positions and long tails in invariant mass distributions. Unfortunately, they are often set aside in first phenomenological approaches although they actually deserve special attention.

In addition one might think of scenarios in which a distortion of invariant mass combinations does *not* stem from allegedly false assignments of final state objects, namely fake combinatorics, but rather from ancillary exotic particle content. It is not unusual for this to happen due to a slight extension of the scenario itself (e.g. from particles with non-standard assignments of quantum numbers) instead of a complete change of the underlying model paradigm (e.g. SUSY ↔ UED).

These major difficulties of new physics cascades motivate the study of their effects and the assessment of their importance on the new physics search program at the LHC in three different parts of this thesis. After a brief overview of several mass and spin determination methods in Chapter 2, we start our investigation with the discussion of off-shell effects in Chapter 3. In a quite generic SUSY setting we discuss the impact of non-resonant gluino propagator contributions far off the mass-shell on established mass and spin measurements using a scan of an effective width-to-mass ratio $\gamma = \Gamma/M$ over a set of discrete values. In this part our aim is to quantify the endpoint smearing and examine how far a model discrimination between SUSY and UED is at stake. Next, we discuss combinatorial and SUSY backgrounds in Chapter 4. We study the gluino dijet endpoint measurement at the LHC in three scenarios with distinct phenomenological aspects. To estimate the impact of the backgrounds, our event samples contain all potential SUSY production and decay processes as well as additional effects from initial and final state radiation, hadronisation and detector response. In order to disentangle different signal contributions, we split the inclusive sample and apply existent and novel variables, which we propose to minimize the impact of both combinatorial and SUSY backgrounds. In this way we assess the feasibility of a fundamental SUSY endpoint measurement which is often assumed to be easily obtained yet itself severely suffers from various troubling backgrounds. The third part addresses the issue of fake combinatorics in Chapter 5. We discuss how the existence of additional particles with non-standard quantum numbers drastically alters the appearance of invariant mass distributions and potentially mimics distorting effects of combinatorial backgrounds in standard SUSY scenarios. Through a scan of different exotic masses relative to the underlying SUSY spectrum we analyse to what extent a possible model discrimination is in danger and how these exotic signatures may be disentangled from ordinary superpartners. Finally we summarise our results in Chapter 6 and conclude our discussion with a brief overview and outlook.

Chapter 2

Methods of Mass and Spin Determination at Hadron Colliders

Immediately ensuing a discovery of new phyiscs is the determination of underlying model parameters, two important milestones of which are the measurements of masses *and* spins of novel particles[1].

In the following we will give a brief overview of available techniques that have been introduced in the last years in anticipation of the LHC start-up. First we discuss a set of mass measurements using SUSY as a straw-model, before giving a concise introduction to the so-called Edge-to-Bump method, which will find frequent application throughout this thesis. The last part will cover several spin measurements that aim for a discrimination of SUSY and UED scenarios.

All variables and procedures to be discussed in this chapter are merely a small selection of a comprehensive field in the literature. The aim is not to give a complete summary of this topic but rather to introduce a few important corner stones of these developments and to set up the methods which are to be investigated upon their vulnerability to off-shell contributions in Chapter 3. For a general introduction as well as thorough reviews of both mass and spin determinations we refer the reader to [47, 48] and references therein.

---

[1] As pointed out in the introduction, the precise knowledge of new couplings is also of fundamental interest but will not be covered here.

2.1 Mass Measurements

Many existing studies determine endpoints of invariant mass combinations and subsequently the masses of new particles with great precision using methods of pseudo-experiments among others. However, at this point we will not elaborate on the particular details of such analyses but instead concentrate on the introduction and explanation of the relevant underlying invariant mass variables themselves as well as discuss their connection to theoretically expected endpoint positions.

In general, mass measurement procedures may be divided into two parts: exclusive and inclusive ones. While the former consist of variables that intrinsically assume to have a single exclusive decay chain with no backgrounds and combinatorics at hand, the latter generally take these issues into account and make use of the complete event information, i.e. all visible particles from two distinct cascades. First, we will discuss exclusive variables before turning to a prominent example addressing the inclusive aspects.

As a short outlook, we will introduce a novel *inclusive* method in Chapter 4, which serves to extract gluino dijet endpoints in a fully inclusive environment at the LHC.

2.1.1 Exclusive Cascades

The Golden Decay Chain

A well studied example in the literature is a particular decay chain that has proven to be very useful in determining parameters of the underlying model. Its frequent application in several variables combined with the success of the methods tailored to this specific topology led to the term *golden (decay) chain*. It is given by the decay of a left-handed squark

$$\tilde{q}_L \to q\tilde{\chi}_2^0 \to ql^\pm \tilde{l}_R^\mp \to ql^\pm l^\mp \tilde{\chi}_1^0 \qquad (2.1)$$

into a quark, two leptons and the lightest neutralino via two succesive on-shell decays of a second-to-lightest neutralino and a right-handed slepton (cf. Figure 2.1). All of these decay products allow for several invariant mass combinations to be formed whose endpoints enclose information about the involved particle masses in question. In what follows, we will discuss these possibilities and present their theoretically

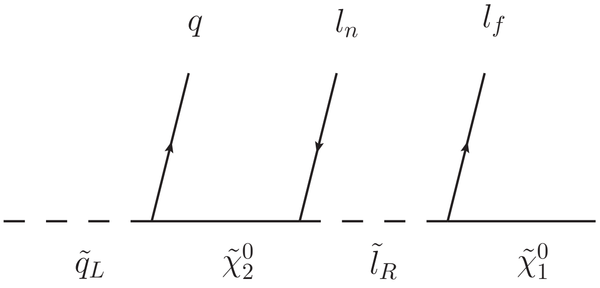

Figure 2.1: The golden decay chain under investigation. Note the indices at the leptons declaring the conceptional difference between near and far decay products (with respect to the quark).

expected endpoint positions as functions of the new particle masses. We begin at the end of the decay cascade.

The dilepton edge m_{ll} The dilepton edge is presumably one of the most studied and most famous endpoints in the literature and the endpoint of one possible invariant mass combination of the golden chain introduced above. Being connected through an intermediate slepton, the kinematics of the two leptons do not posses any form of spin correlation. The result is an invariant mass distribution which is a pure phase space distribution with a triangular shape and a sharp edge at the maximum [49, 50]

$$(m_{ll}^{max})^2 = \frac{(m_{\tilde{\chi}_2}^2 - m_{\tilde{l}}^2)(m_{\tilde{l}}^2 - m_{\tilde{\chi}_1}^2)}{m_{\tilde{l}}^2}, \tag{2.2}$$

where for convenience we used the abbreviations $m_{\tilde{\chi}_i} = m_{\tilde{\chi}_i^0}$, $m_{\tilde{l}} = m_{\tilde{l}_R}$. Hence the dilepton edge encloses information about the outgoing, intermediate and mother particle.

The quark-lepton edge m_{ql} As a next step, one may take into account the quark from the squark decay and form and invariant masses out of either of the two leptons, whose edge positions are given by

$$(m_{ql_n}^{max})^2 = \frac{(m_{\tilde{q}}^2 - m_{\tilde{\chi}_2}^2)(m_{\tilde{\chi}_2}^2 - m_{\tilde{l}}^2)}{m_{\tilde{\chi}_2}^2} \tag{2.3}$$

$$(m_{ql_f}^{max})^2 = \frac{(m_{\tilde{q}}^2 - m_{\tilde{\chi}_2}^2)(m_{\tilde{l}}^2 - m_{\tilde{\chi}_1}^2)}{m_{\tilde{l}}^2} \tag{2.4}$$

where l_n (near) denotes the lepton from the first neutralino decay and l_f (far) the one from the slepton decay. Also take note of the additional abbreviation $m_{\tilde{q}} = m_{\tilde{q}_L}$. As we are not able to tell which of both leptons is near or far on an experimental level, we have to use a workaround to account for the observability. One such possibility is the minimization or maximization over two possible quark-lepton combinations using the lepton charge [49]:

$$m_{ql_{low}} = \min\left[m_{ql^+}, m_{ql^-}\right] \tag{2.5}$$

$$m_{ql_{high}} = \max\left[m_{ql^+}, m_{ql^-}\right] \tag{2.6}$$

whose kinematic endpoints are given by

$$(m_{ql_{low}}^{max})^2 = \min\left[(m_{ql_n}^{max})^2, (m_{ql_{eq}}^{max})^2\right] \tag{2.7}$$

$$(m_{ql_{high}}^{max})^2 = \max\left[(m_{ql_n}^{max})^2, (m_{ql_f}^{max})^2\right] \tag{2.8}$$

where

$$(m_{ql_{eq}}^{max})^2 = \frac{(m_{\tilde{q}}^2 - m_{\tilde{\chi}_2}^2)(m_{\tilde{l}}^2 - m_{\tilde{\chi}_1}^2)}{(2m_{\tilde{l}}^2 - m_{\tilde{\chi}_1}^2)}. \tag{2.9}$$

is adopted from [51]. While the endpoint of $m_{ql_{high}}$ directly follows from equation (2.6), the last definition of $m_{ql_{eq}}$ from [51] is required for $m_{ql_{low}}^{max}$, where the situation is more involved. To find the true maximum of the low-type invariant mass $m_{ql_{low}}$, three different cases ($m_{ql_n} < m_{ql_f}$, $m_{ql_n} = m_{ql_f}$ and $m_{ql_n} > m_{ql_f}$) have to be investigated as in [50, 51] which results in equations (2.7) and (2.9).

The major difference of quark-lepton and dilepton invariant masses is inherent in the intermediate particle: the second-to-lightest neutralino between quark and lepton is of fermionic nature and thus able to carry helicity information, which is directly reflected in the shape of the distributions. This feature will be exploited further later on when we discuss spin measurements in decay cascades.

The quark-dilepton edge m_{qll} The lepton ambiguity discussed above is not present when both leptons are included in addition to the quark. The invariant mass of all three objects benefits from two possible measurements separately: the kinematic threshold m_{qll}^{min} as well as the endpoint m_{qll}^{max}. The latter depends on the precise mass ratios of the spectrum [51]:

$$(m_{qll}^{max})^2 = \begin{cases} \frac{\left(m_{\tilde{q}}^2 - m_{\tilde{\chi}_2}^2\right)\left(m_{\tilde{\chi}_2}^2 - m_{\tilde{\chi}_1}^2\right)}{m_{\tilde{\chi}_2}^2} & \text{for} \quad \frac{m_{\tilde{q}}}{m_{\tilde{\chi}_2}} > \frac{m_{\tilde{\chi}_2}}{m_{\tilde{l}}} \frac{m_{\tilde{l}}}{m_{\tilde{\chi}_1}} \\ \frac{\left(m_{\tilde{q}}^2 m_{\tilde{l}}^2 - m_{\tilde{\chi}_1}^2 m_{\tilde{\chi}_2}^2\right)\left(m_{\tilde{\chi}_2}^2 - m_{\tilde{l}}^2\right)}{m_{\tilde{l}}^2 m_{\tilde{\chi}_2}^2} & \text{for} \quad \frac{m_{\tilde{\chi}_2}}{m_{\tilde{l}}} > \frac{m_{\tilde{l}}}{m_{\tilde{\chi}_1}} \frac{m_{\tilde{q}}}{m_{\tilde{\chi}_2}} \\ \frac{\left(m_{\tilde{q}}^2 - m_{\tilde{l}}^2\right)\left(m_{\tilde{l}}^2 - m_{\tilde{\chi}_1}^2\right)}{m_{\tilde{l}}^2} & \text{for} \quad \frac{m_{\tilde{l}}}{m_{\tilde{\chi}_1}} > \frac{m_{\tilde{q}}}{m_{\tilde{\chi}_2}} \frac{m_{\tilde{\chi}_2}}{m_{\tilde{l}}} \\ \left(m_{\tilde{q}} - m_{\tilde{\chi}_1}\right)^2 & \text{otherwise} \end{cases} \tag{2.10}$$

These are obtained by treating the two leptons as one *effective* particle with a mass $\kappa \cdot m_{ll}^{max}$, where $\kappa \in [0,1]$, and combining this with q. A careful analysis [50] of all possible values of κ then leads to the four cases detailed in equation (2.10).

The threshold, i.e. the minimal value, of m_{qll} is defined as the minimum of the distribution with the two leptons fulfilling the requirement of an opening angle greater than $\pi/2$ ($\theta_{ll} > \pi/2$):

$$\begin{aligned} (m_{qll}^{min})^2 = \Big[& 2m_{\tilde{l}}^2(m_{\tilde{q}}^2 - m_{\tilde{\chi}_2}^2)(m_{\tilde{\chi}_2}^2 - m_{\tilde{\chi}_1}^2) + (m_{\tilde{q}}^2 + m_{\tilde{\chi}_2}^2)(m_{\tilde{\chi}_2}^2 - m_{\tilde{l}}^2)(m_{\tilde{l}}^2 - m_{\tilde{\chi}_1}^2) \\ & -(m_{\tilde{q}}^2 - m_{\tilde{\chi}_2}^2)\sqrt{(m_{\tilde{\chi}_2}^2 + m_{\tilde{l}}^2)^2(m_{\tilde{l}}^2 + m_{\tilde{\chi}_1}^2)^2 - 16 m_{\tilde{\chi}_2}^2 m_{\tilde{l}}^4 m_{\tilde{\chi}_1}^2}\ \Big] / (4 m_{\tilde{l}}^2 m_{\tilde{\chi}_2}^2). \end{aligned} \tag{2.11}$$

Counting all endpoint variables of the golden chain discussed so far, we end up with four (five if we take the threshold into account) which correspond to the four unknown masses $m_{\tilde{\chi}_1}$, $m_{\tilde{\chi}_2}$, $m_{\tilde{l}_R}$ and $m_{\tilde{q}_L}$. In principle, one could thus solve equations (2.2), (2.7), (2.8) and (2.10) for the unknowns and obtain all masses simultaneously.

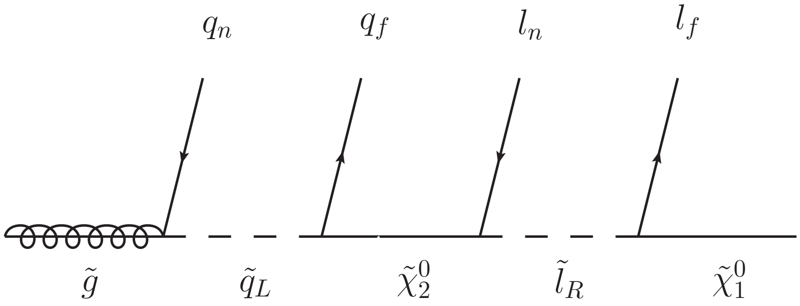

Figure 2.2: The gluino decay chain under investigation. Note the indices at quarks and leptons declaring the conceptional difference between near and far decay products.

The Gluino Decay Chain

Another well studied case [52] is the decay cascade, where a precedent two body decay of a gluino is attached at the beginning of the golden chain (cf. Figure 2.2):

$$\tilde{g} \rightarrow q_n \tilde{q}_L \rightarrow q_n q_f \tilde{\chi}_2^0 \rightarrow q_n q_f l^\pm \tilde{l}_R^\mp \rightarrow q_n q_f l^\pm l^\mp \tilde{\chi}_1^0 \tag{2.12}$$

Notice the introduction of subscripts n (near) and f (far) for the quarks. These are given by means of discrimination between the quark from the gluino decay (q_n) and the one from the squark decay (q_f). In the golden chain, there exists no such quark ambiguity and $q \equiv q_f$ holds in terms of the upper notation.[2] The endpoint values from the last section may also be obtained here when applied to the specific subtopology of the last three decay objects. This might be experimentally feasible for certain spectra where a differentiation between q_n and q_f is possible due to e.g. the difference in transverse momentum p_T. Furthermore, the presence of another final state quark allows for up to seven additional invariant mass combinations to be built, which we will discuss in the following.

The diquark edge m_{qq} An equivalent of the dilepton edge as discussed above is the diquark edge with an intermediate squark. It possesses the same features and thus the same endpoint formula with the substitutions $m_{\tilde{\chi}_2} \rightarrow m_{\tilde{g}}$, $m_{\tilde{l}} \rightarrow m_{\tilde{q}}$ and

---

[2] We will only use subscripts where appropriate, i.e. if a potential quark ambiguity exists.

$m_{\tilde{\chi}_1} \rightarrow m_{\tilde{\chi}_2}$:

$$(m_{qq}^{max})^2 = \frac{(m_{\tilde{g}}^2 - m_{\tilde{q}}^2)(m_{\tilde{q}}^2 - m_{\tilde{\chi}_2}^2)}{m_{\tilde{q}}^2}. \tag{2.13}$$

However, the most important difference is the coloured nature of the visible outgoing decay products, which are thus much harder to identify and discriminate in an LHC environment. Furthermore there is no reliable straightforward way of tagging charges in jets as there is in the leptonic case. Despite this drawback, some studies attempt to measure this endpoint using third generation (bottom) quarks for which a discrimination between particles and anti-particles may be feasible, depending upon the b-tagging algorithm [52]. Moreover, the precise position of this endpoint is of great importance since it contains the first of several decay products and encloses information about the masses of the parent gluino, the intermediate squark as well as the outgoing neutralino[3]. In Chapter 4 we will study the extraction of this particular dijet endpoint with existing and novel variables for the case of heavy scalars and a gluino three-body decay, a scenario favoured by the potential Higgs discovery at the LHC.

The *near*-quark-lepton edge $m_{q_n l}$ The two particle invariant masses involving the gluino mass parameter are very similar to the ones involving the squark one. In the near/far notation, $m_{q_f l_n}$ and $m_{q_f l_f}$ are equivalent to equations (2.3) and (2.4) with $q = q_f$. However, due to the presence of q_n we are now able to build $m_{q_n l_n}$ and $m_{q_n l_f}$ in addition. Their kinematic endpoint values are given by

$$(m_{q_n l_n}^{max})^2 = \frac{(m_{\tilde{g}}^2 - m_{\tilde{q}}^2)(m_{\tilde{\chi}_2}^2 - m_{\tilde{l}}^2)}{m_{\tilde{\chi}_2}^2} \tag{2.14}$$

$$(m_{q_n l_f}^{max})^2 = \frac{(m_{\tilde{g}}^2 - m_{\tilde{q}}^2)(m_{\tilde{l}}^2 - m_{\tilde{\chi}_1}^2)}{m_{\tilde{l}}^2} \tag{2.15}$$

which are identical to equations (2.3) and (2.4) up to the replacment $m_{\tilde{q}} \rightarrow m_{\tilde{g}}$ and $m_{\tilde{\chi}_2} \rightarrow m_{\tilde{q}}$ in the first bracket. To achieve an experimental observation[4], we again construct *high-* and *low-*type distributions of which the endpoints are obtained in

---

[3] One might also consider a short gluino decay cascade, in which a right-chiral squark directly decays to a quark and the lightest neutralino. In such a scenario, the endpoint information is even more valuable since it directly encodes the mass of the LSP, i.e. the dark matter candidate.

[4] under the assumption that a differentiation between q_f and q_n is feasible, i.e. by means of the transverse momentum p_T.

complete analogy to equations (2.7) and (2.8)

$$(m^{max}_{q_n l_{low}})^2 = \min\left[(m^{max}_{q_n l_n})^2, (m^{max}_{q_n l_{eq}})^2\right] \tag{2.16}$$

$$(m^{max}_{q_n l_{high}})^2 = \max\left[(m^{max}_{q_n l_n})^2, (m^{max}_{q_n l_f})^2\right] \tag{2.17}$$

with

$$(m^{max}_{q_n l_{eq}})^2 = \frac{(m^2_{\tilde{g}} - m^2_{\tilde{q}})(m^2_{\tilde{l}} - m^2_{\tilde{\chi}_1})}{(2m^2_{\tilde{l}} - m^2_{\tilde{\chi}_1})}. \tag{2.18}$$

The diquark-lepton edge m_{qql} Extending $m_{q_f l_n}$ and $m_{q_f l_f}$ with the additional quark q_n from the gluino decay, we arrive at m_{qql_n} and m_{qql_f}. The endpoints of these distributions are obtained using the same considerations as for the three-particle invariant mass case of m_{qll}. In fact, m_{qql_n} is an invariant mass with three direct neighbours in the decay chain and is hence given by equation (2.10) with the replacement

$$\left(m_{\tilde{q}}, m_{\tilde{\chi}_2}, m_{\tilde{l}}, m_{\tilde{\chi}_1}\right) \rightarrow \left(m_{\tilde{g}}, m_{\tilde{q}}, m_{\tilde{\chi}_2}, m_{\tilde{l}}\right). \tag{2.19}$$

As for m_{qql_f}, the calculation of the theoretical endpoint position is more involved. Since the far lepton is not a next neighbour of the quark pair, we have to introduce a pseudo-particle Y so as to maximize the invariant mass distribution of our choice [52]. For m_{qql_f} this happens at the end of the decay cascade with $\tilde{\chi}^0_2 \rightarrow l_f Y$ with $m_Y = m_{\tilde{\chi}_1} m_{\tilde{\chi}_2} / m_{\tilde{l}}$. In this way, the introduction of the pseudo-particle Y transforms the problem to a next-neighbour situation and thus we may consequently use the result (equation (2.10)) of m_{qll} from above with the substitutions

$$\left(m_{\tilde{q}}, m_{\tilde{\chi}_2}, m_{\tilde{l}}, m_{\tilde{\chi}_1}\right) \rightarrow \left(m_{\tilde{g}}, m_{\tilde{q}}, m_{\tilde{\chi}_2}, m_{\tilde{\chi}_1} m_{\tilde{\chi}_2} / m_{\tilde{l}}\right). \tag{2.20}$$

To account for observability, we define $m_{qql_{high}}$ and $m_{qql_{low}}$ as above. The high endpoint $m^{max}_{qql_{high}}$ is again given by the larger value of the two variables m_{qql_n} and m_{qql_f}. The lower endpoint $m^{max}_{qql_{low}}$ however is more delicate to obtain due to the inherent complications from the analysis of different cases for three-particle invariant masses along with the kinematical limitations of the minimization procedure of *low*-type endpoints.

While the complete lengthy derivation is given in [52], we quote the final results

$$m_{qql_{high}}^{max} = \max\left[m_{qql_n}^{max}, m_{qql_f}^{max}\right] \tag{2.21}$$

$$m_{qql_{low}}^{max} = \begin{cases} m_{qql_n}^{max} & \text{for} \quad m_{\tilde{\chi}_1}^2 + m_{\tilde{\chi}_2}^2 < 2m_{\tilde{l}}^2 \\ m_{qql_f}^{max} & \text{for} \quad \text{(condition (1))} \\ m_{qql_{eq}}^{max} & \text{otherwise} \end{cases} \tag{2.22}$$

where both (condition (1)) as well as $m_{qql_{eq}}^{max}$ are defined in [52].

The *near*-quark-dilepton edge m_{qll} The presence of the additional near quark q_n yields the possibility to combine it with the two leptons further down the cascade. The particular feasibility on an experimental level is again strongly dependent upon the ability to disentangle q_n from q_f and thus upon the spectrum in question. Nonetheless, for the theoretical endpoint value we reintroduce another pseudo-particle $Y' \to \tilde{\chi}_2^0 q_n$ decaying into the second-lightest neutralino and the *near* quark to reformulate the stituation using only nearest neighbours. Its invariant mass is given by $m_{Y'}^2 = m_{\tilde{g}}^2 - m_{\tilde{q}}^2 + m_{\tilde{\chi}_2}^2$ with the corresponding substitution

$$m_{\tilde{q}} \to m_{Y'} = \sqrt{m_{\tilde{g}}^2 - m_{\tilde{q}}^2 + m_{\tilde{\chi}_2}^2} \tag{2.23}$$

in equation (2.10) to obtain the possible endpoint positions.

The diquark-dilepton edge m_{qqll} The maximum endpoint values of the invariant mass of all gluino decay products (i.e. the complete visible part of the cascade) are constructed similarily to $m_{q_f ll}$. In contrast to the latter however, there exist four regions of mass dominance in the complete parameter space of all potential models owing to the fact that we have one additional decay particle [52]:

$$(m_{qqll}^{max})^2 = \begin{cases} \frac{\left(m_{\tilde{g}}^2-m_{\tilde{q}}^2\right)\left(m_{\tilde{q}}^2-m_{\tilde{\chi}_1}^2\right)}{m_{\tilde{q}}^2} & \text{for} \quad \frac{m_{\tilde{g}}}{m_{\tilde{q}}} > \frac{m_{\tilde{q}}}{m_{\tilde{\chi}_2}} \frac{m_{\tilde{\chi}_2}}{m_{\tilde{l}}} \frac{m_{\tilde{l}}}{m_{\tilde{\chi}_1}} \\ \frac{\left(m_{\tilde{g}}^2 m_{\tilde{\chi}_2}^2-m_{\tilde{q}}^2 m_{\tilde{\chi}_1}^2\right)\left(m_{\tilde{q}}^2-m_{\tilde{\chi}_2}^2\right)}{m_{\tilde{q}}^2 m_{\tilde{\chi}_2}^2} & \text{for} \quad \frac{m_{\tilde{q}}}{m_{\tilde{\chi}_2}} > \frac{m_{\tilde{\chi}_2}}{m_{\tilde{l}}} \frac{m_{\tilde{l}}}{m_{\tilde{\chi}_1}} \frac{m_{\tilde{g}}}{m_{\tilde{q}}} \\ \frac{\left(m_{\tilde{g}}^2 m_{\tilde{l}}^2-m_{\tilde{\chi}_2}^2 m_{\tilde{\chi}_1}^2\right)\left(m_{\tilde{\chi}_2}^2-m_{\tilde{l}}^2\right)}{m_{\tilde{l}}^2 m_{\tilde{\chi}_2}^2} & \text{for} \quad \frac{m_{\tilde{\chi}_2}}{m_{\tilde{l}}} > \frac{m_{\tilde{l}}}{m_{\tilde{\chi}_1}} \frac{m_{\tilde{g}}}{m_{\tilde{q}}} \frac{m_{\tilde{q}}}{m_{\tilde{\chi}_2}} \\ \frac{\left(m_{\tilde{g}}^2-m_{\tilde{l}}^2\right)\left(m_{\tilde{l}}^2-m_{\tilde{\chi}_1}^2\right)}{m_{\tilde{l}}^2} & \text{for} \quad \frac{m_{\tilde{l}}}{m_{\tilde{\chi}_1}} > \frac{m_{\tilde{g}}}{m_{\tilde{q}}} \frac{m_{\tilde{q}}}{m_{\tilde{\chi}_2}} \frac{m_{\tilde{\chi}_2}}{m_{\tilde{l}}} \\ \left(m_{\tilde{g}} - m_{\tilde{\chi}_1}\right)^2 & \text{otherwise} \end{cases} \tag{2.24}$$

Notice the mass ratios of the inequalities, which follow the notational convention of [52]. The reasoning is to highlight the regions with the largest mass gaps between two particles that dominate the endpoint position of the complete decay cascade.

2.1.2 Inclusive Approaches

In general it is rather intricate to disentangle decay products originating from two different cascades. In the leptonic case, e.g. for the dilepton-edge, there exist methods such as the so-called flavour-subtraction in which contributions of the *wrong* backgrounds from opposite-sign different-flavour (OSDF) leptons are subtracted off *correct* contributions from opposite-sign same-flavour (OSSF) leptons yielding the desired triangular shape with a clear-cut endpoint structure. On the other hand, the discrimination of multiple jets from two cascades in a polluted LHC environment is a delicate task, suffering from *combinatorial* backgrounds which recently received much attention [53, 54, 55]. However, the approaches discussed in the last section rely on this information, namely the assignment to one particular decay chain side. A possible solution is to apply such a technique to reduce the *combinatorial* problem before a particular exclusive variable is investigated further.

An alternative approach is the usage of (more) inclusive variables that are to be applied on the complete event including decay products of both cascades. These are less affected by *combinatorics* or ideally have no need for a particular decay cascade side selection depending on the final state and decay topology. In the following paragraphs we will introduce a few such observables based on the Stransverse Mass M_{T2}.

First, however, we have to introduce the transverse mass m_T.

The transverse mass m_T The transverse mass m_T is defined as

$$m_T^2(p_T, q_T) = (p_T + q_T)^2 = m_p^2 + m_q^2 + 2\left(E_{T,p}E_{T,q} - \vec{p}_T \cdot \vec{q}_T\right) \tag{2.25}$$

where p and q denote the momenta of visible and invisible particles, respectively and $E_{T,j}$ is defined as

$$E_{T,j} \equiv \sqrt{j_T^2 + m_j^2} \qquad \text{with} \quad j = p, q. \tag{2.26}$$

m_T has proven to be very useful when applied to events containing a leptonically decaying W boson at Hadron Colliders [4]. More precisely, for p the momentum of the electron and q the momentum of the neutrino alias the missing momentum, the inequality

$$m_T^2 \leq m_W^2 \tag{2.27}$$

holds in the approximation for both massless electron and neutrino.

The Stransverse mass M_{T2} The transverse mass is not particularly useful for mass determination in SUSY events with conserved R-parity or other such examples[5] which feature two invisible particles escaping the detector, where only the sum $\not{p}_T$ of those momenta is an experimental observable. So if it were possible to obtain both of these momenta q_1 and q_2, one would be able to construct two transverse masses $m_T^{(1)}$ and $m_T^{(2)}$, the maximum of which would then serve as an upper bound for the corresponding sparticle mass $m_{\tilde{s}}$ of the mother particle:

$$m_{\tilde{s}} \leq \max\left[m_T^{(1)}, m_T^{(2)}\right]. \tag{2.28}$$

Since, however, we are not able to access the momenta of the two invisible particles individually, a new variable was proposed in [56] defined as

$$M_{T2}^2(m_\chi, \not{p}_T, p_T^{(1)}, p_T^{(2)}) \equiv \min_{\vec{q}_T^{(1)} + \vec{q}_T^{(2)} = \not{\vec{p}}_T} \left[\max\{m_T^2(p_T^{(1)}, q_T^{(1)}), m_T^2(p_T^{(1)}, q_T^{(2)})\}\right], \tag{2.29}$$

---

[5] e.g. UED with KK-parity, little Higgs with T-parity, etc ...

where $m_\chi = m_q$ is the a priori unknown mass of the invisible dark matter candidate and a constant input parameter that has to be regarded as a test or trial mass. The minimization is taken over all possible partitions of three-momenta $\vec{q}_i$ in a way such that their sum is equal to the observed missing momentum $\vec{\not{p}}_T$. Notice that due to the minimization procedure the upper bound is again given by the sparticle mass

$$M_{T2}^2(m_\chi, \not{p}_T, p_T^1, p_T^2) \leq m_{\tilde{s}}^2, \tag{2.30}$$

which allows for a direct observation of new physics masses at the LHC if the correct trial mass m_χ is used. Unfortunately, m_χ is not known from first principles. Considering that the endpoint $M_{T2}^{\max}(m_\chi)$ is a function of the trial mass, a careful analysis of this dependency yields a pronounced kink in the distribution of endpoint positions plotted against both the gluino and the trial mass. In this way, we are able to estimate both masses simultaneously [57]. In a careful analysis of the maximal endpoint shift of $M_{T2}^{\max}(m_\chi)$ as a function of the trial (LSP) mass m_χ returns a pronounced kink in the distribution reflecting the true mass of both the gluino and the dark matter.

Another issue of M_{T2} is the ambiguity in selecting the corresponding visible particle momenta $p_T^{(1)}$ and $p_T^{(2)}$. Initially it was proposed to be applied to slepton production at the LHC, in which case the signature of two leptons and $\not{p}_T$ is free of combinatorical problems. The same holds for squark pair production with prompt decay to quark and LSP. If M_{T2} is however applied to events containing coloured sparticles with more than two hard objects, several complications arise. We will discuss these together with their respective solutions in the next paragraphs.

The inclusive Stransverse Mass M_{T2}^{inc} An important matter is encoded in the grouping of the visible momenta $p_T^{(1)}$ and $p_T^{(2)}$. To be able to obtain the true endpoint, we need to find a way to assign the observable momenta to two sides each of which corresponds to one of the two decay chains. These are then taken as input parameters for M_{T2}. One such realization [58] relies on the hemisphere algorithm [59], which we will review in some detail. The basics are as follows:

In a first step, each event is divided into two distinct hemispheres defined by two seeds. The hardest of all objects, i.e. jets or leptons, $p_T^{(1)}$ is taken as the first seed. Next, the item j which maximizes the product of distance and momentum

$$\Delta R(1,j) \cdot |\vec{p}_j| = \sqrt{\Delta\eta_{1j}^2 + \Delta\phi_{1j}^2} \cdot |\vec{p}_j| \tag{2.31}$$

represents the second seed. These two objects then define the first incarnation of the two hemispheres. All remaining particles are subsequently clustered to one of these spatial areas according to the value which minimizes the Lund distance measure [59]

$$d(p_k, p_j^{(s)}) = (E_j - p_j^{(s)} \cos\theta_{jk}) \frac{E_j}{(E_j + E_k)^2}. \tag{2.32}$$

between the four momentum p_k of the object to be associated and the two seed momenta $p_1^{(s)}$ and $p_2^{(s)}$. After all items have been assigned, the seeds are redefined as the sum of all momenta in the corresponding hemisphere. The last two steps (cluster to and redefine seeds) are iterated until the whole assignment converges, i.e. the momenta of the seeds of the n-th iteration is not changed with respect to the $n+1$-th iteration. More details on the specifics and variations of this algorithm may be found in [59].

The results are two spatially distinct hemispheres represented by two seeds. These we are able to use as input for the visible momenta p_T^1 and p_T^2 required by M_{T2} as was suggested in [58]:

$$M_{T2}^{\text{inc}} \equiv M_{T2}(m_\chi, \not{p}_T, p_1^{(s)}, p_2^{(s)}). \tag{2.33}$$

A comment is in place here: one fundamental assumption for the 'correct' assignment[6] of this algorithm is the presence of a certain hierarchy in the mass spectrum, the result of which are boosts in the decay chains allowing for a spatial separation of particles from different cascades. Since particles produced in rest are known to decay isotropically[7], the hemisphere algorithm is expected to perform badly. Surely such a spectrum may not be realized in nature and hence, other alternatives may be superior to this procedure [53].

The inclusive character of this method is manifest in the fact that no particular decay cascades are analysed but rather a complete set. The signals in this study are dominantly given by squark-gluino associated production for the two benchmark points under investigation [58].

---

[6] With 'correct' assignment we identify a clustering of momenta such that particles originating from a particular decay cascade end up in the same hemisphere group.

[7] discarding helicity informations of mother and daughters

The minimised Stransverse Mass $M_{T2}^{\min}$ Another complication concerning the application of M_{T2} arises from falsely selected jets not originating from the desired new physics particle in question but rather from additional initial and final state radiation. This issue has recently been addressed in [60], where a new variable was introduced that makes inherent use of M_{T2}. However, this study only covers an exclusive[8] sample of five jets which originate from gluino pair production with subsequent decay to two partons and one neutralino per side in conjunction with an additional initial state radiation jet. Since the presence of the latter can drastically smear the distinctive shape in the vicinity of the true endpoint, it is of crucial importance to eliminate its impact. To this extent the following variable was proposed

$$M_{T2}^{\min} \equiv \min_{i=1,\ldots,5} \{M_{T2}(i)\} \tag{2.34}$$

where $M_{T2}(i)$ is defined as

$$M_{T2}(i) \equiv \min_{j=1,\ldots,i-1,i+1,\ldots,5} \left(M_{T2}^{(1)}, M_{T2}^{(2)}\right) \tag{2.35}$$

based on the four-jet M_{T2} variants

$$M_{T2}^{(1)} \equiv M_{T2}((p_{T,1}+p_{T,3}),(p_{T,2}+p_{T,4})), \tag{2.36}$$

$$M_{T2}^{(2)} \equiv M_{T2}((p_{T,1}+p_{T,4}),(p_{T,2}+p_{T,3})). \tag{2.37}$$

Comparing equations (2.33) and (2.34), we notice an important difference to M_{T2}^{inc}: while the inclusive version of M_{T2} is in principle able to handle a large amount of decay products per side to be combined with the help of the hemisphere method, $M_{T2}^{\min}$ relies on a simple pattern of shuffled momenta for (remaining) four-jet event topologies. Nevertheless, the motivation and idea behind the definition of $M_{T2}^{\min}$ is the observation that the transverse momentum p_T^{rad} of the additionally radiated jet is of the same order of magnitude as the $p_{T,i}$ of the gluino decay products.

2.1.3 Edge-to-Bump Method

In the following we briefly introduce a method to quantitatively acquire kinks and endpoints from distributions that will be used frequently throughout this thesis. It is

---

[8] Here exclusive refers to the size of the jet-sample instead of denoting the difference in mass measurement techniques.

based on [61] but extended in use and slightly adapted to the various applications.

The precise position of such cusps in distributions is a non-trivial task of high physical relevance. As discussed in rich detail in the last sections, kinematical endpoints and kinks in invariant mass distributions may serve as a Lorentz-invariant measure of particle masses from new physics processes. Fitting of such distributions is, however, very vulnerable to human bias in several ways. First of all, the fitting range strongly influences the position of kinks and endpoints as a fit value. Second, the fit result additionally depends upon the initial value of the parameters. Furthermore, the chosen fit function also influences the outcome of the measurement to some extent. In a nutshell, these issues lead to systematic uncertainties, which are hard to quantify in a meaningful manner. The result is a strong underestimation of the overall mostly statistical error quoted by traditional fits to invariant mass distributions. To overcome these complications, it was proposed to fit a *basic* linear kink function to a random subrange and position of the overall distribution $\mathcal{O}(1000)$ times [61]. In this way, the error-prone endpoint search has been turned into a situation of bump-hunting in a statistical distribution of fit results. The aforementioned systematic uncertainties of human bias are all transformed to effectively contribute to the width of a peak in the resulting distribution of fits, the position of which may constitute a physically meaningful kink.

In the original work it is proposed that after the distribution of fits is obtained, the next steps are the identification and isolation of potentially meaningful peaks according to their width. For ideal distributions with multiple kinks, this might be a necessary procedure. For this study on the other hand, we will investigate subsets of data which ideally consist of only one exclusive endpoint to be analysed. Moreover, as will be discussed in Chapter 3, we are interested in the actual change of endpoint behaviour for different off-shell contributions and to this extent we replace the original steps with our own technique to be introduced in the following.

The statistical endpoint distribution returned by the Edge-to-Bump method gives rise to some background fluctuations close to, but in addition also far away from the main peak. While the mean value and the standard deviation of such a distribution is a first estimate of an actual edge position, statistical artifacts of the former type give rise to shifted mean values and unreasonably large uncertainties. It is for that reason that we adopt the following steps to return a quantitative result, which is less sensitive to smaller peaks, noise and contributions far off the main bump of interest.

First, we calculate a mean value and its standard deviation for the complete distribution. Then, we redefine the range of the distribution to be centred around the newly obtained mean value including all areas within two times the standard deviation. The third step is to calculate a new mean value and standard deviation inside this new range. In the fourth step these values are again used as a new seed to start over with the second step in an iterative procedure which terminates, if the values remain unchanged. In short, we recall these four steps:

1. calculate mean value $\hat{m}_0$ and standard deviation σ_0 of complete distribution
2. redefine range of distribution according to the last values: $\hat{m}_0 \pm 2\sigma_0$
3. calculate new mean value $\hat{m}_i$ and standard deviation σ_i inside the new range
4. use $\hat{m}_i$ and σ_i as a new *seed* and start over with step 2

Roughly speaking, we iteratively reduce the obtained endpoint distribution to intervals of within two standard deviations around the mean value until the assignment converges.

Some specifics of this method as we implemented it into our analysis framework are important. First of all, we fixed the number of fits for each histogram to $n_{fit} = 1000$ times which turned out to be the best tradeoff between statistics and computational run-time. The naive linear kink fitting function we utilized for this is given by

$$f(x; p_1, p_2, p_3, p_4) = \begin{cases} p_1 + p_2(x - p_4) & \text{for } x \geq p_4 \\ p_1 + p_3(x - p_4) & \text{else} \end{cases} \tag{2.38}$$

where the parameters p_i determine the intercept of axes as well as the slopes. Especially p_4 is of interest, since it is the kink position returned by each of the 1000 fits. The overall fitting range $f_{max} \equiv [m_{y,min}, m_{y,max}]$ of the invariant mass distribution is defined as the interval between the maximum $m_{y,max}$ of the histogram and either (1) the end of the histogram or (2) the position, where the number of events is lower than $y_{min} = y_{max}/n_{min}$ (y_{max} is the number of events in the maximum bin and $n_{min} = N/50$ is a parameter of the method we set to be 2 % of the overall number of events N), whichever is encountered first, denoted by $m_{y,min}$. The subrange f_i for each fit i is then defined as a randomly generated domain in between the overall fitting range f_{max}. What is more, we restricted the allowed parameter range to fulfill the following properties

- $f_i \geq 0.3 f_{max}$ (minimum fitting range)
- $p_4 \in f_i$ (kink position inside fitting range)
- $p_2, p_3 < 0$ (both slopes negative)
- $|p_2| < |p_3|$ (first slope steeper than second)

to account for the sanity of the obtained values.

The method as it stands will find two major applications in this thesis. In Chapter 3, we will extract three out of four possible parameters from the fit-function defined in equation (2.38) and estimate the impact of off-shell contributions with these. Chapter 4 governing the gluino dijet endpoint measurement on the other hand will comprise a 'traditional' use in that only the kink position, i.e. the supposed endpoint, will be extracted to quantitatively assess its precise position.

2.2 Spin Measurements

Measuring the masses of new particles usually considered to be the first important step of parameter determination of new physics models. However, to be able to successfully claim whether these are of supersymmetric or other nature, one also has to determine the spins[9] of the new particles. Again we refrain from giving a complete overview but restrict ourselves to a few important milestones in spin determination. We start with procedures which make use of angular correlations that manifest themselves in invariant mass combinations of decay products of the golden decay chain. Afterwards we discuss and extent spin determinations to gluino decay chain before we investigate methods which directly employ more general distributions of decay products emerging from angular correlations of the initially produced particles.

---

[9] For definite certainty about the nature of the underlying model the couplings have to be determined as well, which, unfortunately, will not be addressed further in this thesis.

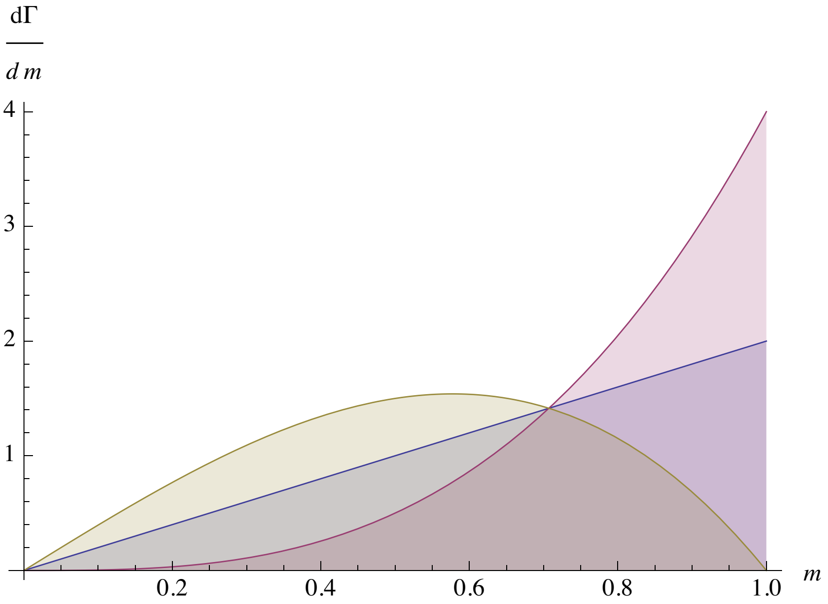

Figure 2.3: Three different anatomies of m_{ql_n}: the blue, red and green shapes correspond to the pure phase space, particle-antiparticle and antiparticle-antiparticle (or particle-particle) distributions, respectively.

2.2.1 Angular Correlations in Cascades

Lepton charge asymmetry An early proposal [39] for spin determination at the LHC is based on an invariant mass combination within the golden decay chain (equation (2.1)). The presence and absence of spin correlations between pairs of decay products in the cascade severely affects kinematics and thus the shapes of invariant mass distributions. In this way, it is possible to get a handle on the spin of the intermediate and mother particles. Let us begin with the invariant mass of the first emitted pair of the quark and the nearer lepton:

$$\left(m_{ql_n}\right)^2 = (p_q + p_l)^2 = 2|\vec{p}_q||\vec{p}_l|(1-\cos\theta^*) = \left(m_{ql_n}^{max}\right)^2 \sin^2(\theta^*/2) \tag{2.39}$$

where $m_{ql_n}^{max}$ was introduced in equation (2.3) and θ^* is the angle of quark and lepton in the rest frame of the second-to-lightest neutralino $\tilde{\chi}_2^0$. The pure phase space distribution of the invariant mass is given by

$$\frac{d\Gamma_{PS}}{d\hat{m}} = 2\sin(\theta^*/2) = 2\hat{m} \tag{2.40}$$

and

$$\hat{m} \equiv m_{ql_n}/m_{ql_n}^{max} = \sin(\theta^*/2) \tag{2.41}$$

is a rescaled quantity. Taking into account spin correlations, the helicities of (anti-) lepton and quark result in additional factors of $\sin(\theta^*/2)$ and $\cos(\theta^*/2)$ in the distribution: while for l^+q and $l^-\bar{q}$

$$\frac{d\Gamma_+}{d\hat{m}} = 4\sin^3(\theta^*/2) = 4\hat{m}^3 \tag{2.42}$$

holds, the case of $l^+\bar{q}$ and l^-q is described by

$$\frac{d\Gamma_-}{d\hat{m}} = 4\sin(\theta^*/2)\cos^2(\theta^*/2) = 4\hat{m}(1-\hat{m}^2). \tag{2.43}$$

The difference in these distributions is apparent in Figure 2.3. While the region around the kinematical endpoint is favoured by particle-antiparticle combinations, the particle-particle (or antiparticle-antiparticle) distributions are suppressed in that regime. This explicit charge asymmetry is due to the intermediate neutralino carrying spin 1/2.

On an experimental level there are issues preventing us from directly measuring these distributions. On one hand in an LHC environment in principle we are not able to distinguish between jets originating from quarks and antiquarks[10]. As a result we will observe the sum of both quark and antiquark contributions which is identical to the phase space distribution from equation (2.40). Nevertheless recalling that the LHC is a proton-proton collider, there is an asymmetry between the possible production of squarks and antisquarks due to the dominance of the valence quark distributions inside the PDFs. On the other hand, we are unable to observe the exclusive variables for quark and charged leptons, m_{ql_n}, irrespective of whether q is a quark or antiquark. What we may analyse however, is m_{ql^+} and m_{ql^-}, which contain both m_{ql_n} and m_{ql_f}. This is the motivation behind the definition of the following lepton charge asymmetry proposed in [39]:

$$A^{\pm} \equiv \frac{m^+ - m^-}{m^+ + m^-} \qquad \text{with} \quad m^{\pm} \equiv \frac{d\sigma}{dm_{ql^{\pm}}} \tag{2.44}$$

Taken as a function of m_{ql}, $A^{\pm}$, plotted in Figure 2.4, shows a distinctive shape not

---

[10] We discard b-tagging methods and third generation quarks for now.

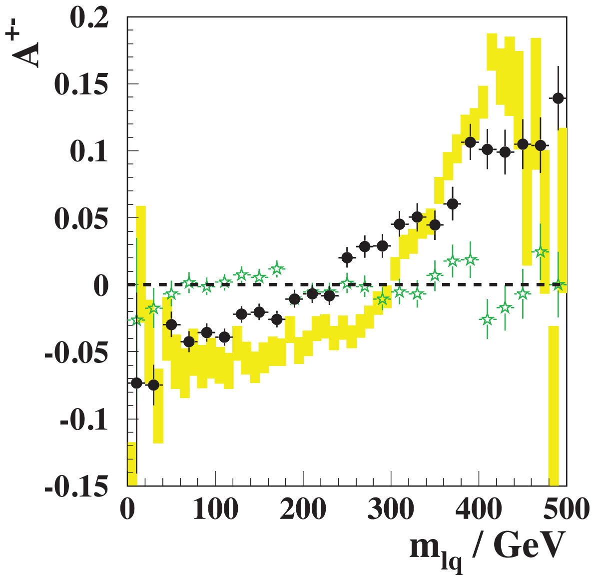

Figure 2.4: The lepton charge asymmetry as a function of m_{ql}. The yellow (black) points denote parton (detector) level results. The green points represent events, where spin correlations are turned off. Figure taken from [39].

consistent with zero on parton level. Furthermore, the included detector level events retain the tendency of the asymmetry and thus allow for a spin determination at the LHC.

The concept of the lepton charge asymmetry $A^{\pm}$ was extended to include a UED model in [40] using two different mass spectra to analyze the discriminative power of the method. In the case of a UED model, the invariant mass distributions of quark and near or far lepton are changed due to the polarisation of the intermediate particle (i.e. the first KK-excitation of the Z boson, the $Z^{(1)}$) and additional spin correlations from the decay of the first excited KK-lepton $l^{(1)}$ (compared to the spin-less slepton $\tilde{l}$). After taking into account the probabilities to observe two different processes for particle-antiparticle invariant mass combinations (and conjugates thereof) as detailed in [40], the lepton charge asymmetry defined in equation (2.44) yields observable differences between a UED and a SUSY model for SUSY like hierarchical mass spectra (cf. Figure 2.5 (b)) but fails to provide sufficient discriminative power for UED like degenerate spectra (cf. Figure 2.5 (a)).

Gluino shape asymmetries A slightly adapted version of the lepton charge asymmetry is used for the discrimination of gluino from KK-gluon signals [41]. Instead of

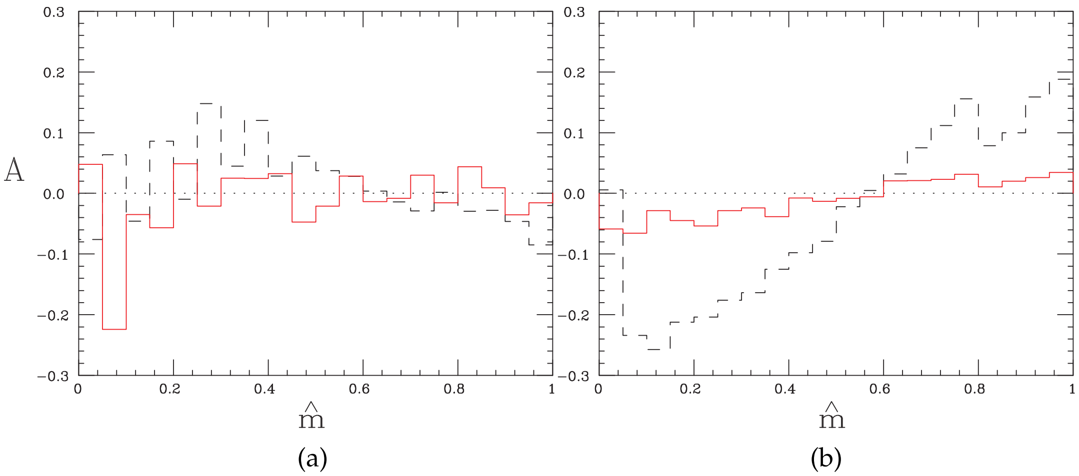

Figure 2.5: Lepton charge asymmetries at detector level for UED (a) and SUSY (b) type mass spectra for the rescaled jet-lepton invariant mass $\hat{m}$. The red solid (black dashed) line corresponds to an underyling UED (SUSY) model. Figures taken from [40].

the golden chain, a longer gluino decay cascade with bottom squarks and leptons is investigated:

$$\tilde{g} \longrightarrow \tilde{b}_i b \longrightarrow \tilde{\chi}_2^0 bb \longrightarrow \tilde{l}_R^{\pm} l^{\mp} bb \longrightarrow \tilde{\chi}_1^0 l^{\pm} l^{\mp} bb. \tag{2.45}$$

It allows for a slightly different application of the method when the invariant mass of a bottom quark combined with one of the two leptons is envisaged to show discrepancies. If the bottom quark stems from the first decay branch, we expect to see differences between a SUSY and UED model. However, since there are two bottom quarks in the sample, there are two options standing to reason for the choice of the corresponding invariant mass combinations. One possibility is based on the b-tagging algorithm: the use of lepton charges from leptonic b-decays allows for a differentiation between bottom and anti-bottom quarks. This defines the following *first* bottom-lepton asymmetry

$$A^{\pm}(m_{bl}) = \frac{d\sigma/dm_{bl^+} - d\sigma/dm_{bl^-}}{d\sigma/dm_{bl^+} + d\sigma/dm_{bl^-}} \tag{2.46}$$

based on the unique choice of a bottom over anti-bottom quark in combination with one of the two leptons. Due to the majorana nature of either the gluino, in 50 % of all cases the bottom quark is emitted in the first decay step. Alternatively we may select one of the bottom quarks through their hardness of the b-jets using the hierarchies of the underlying spectrum. The softer of the two b-tagged jets has a higher probability of supposedly originating from the nearer quark. The resulting *second* bottom-lepton asymmetry is given by

$$A_s^{\pm}(m_{b_s l}) = \frac{d\sigma/dm_{b_s l^+} - d\sigma/dm_{b_s l^-}}{d\sigma/dm_{b_s l^+} + d\sigma/dm_{b_s l^-}}. \tag{2.47}$$

In the upcoming analysis in Chapter 3 we investigate to what extent both of these asymmetries are fragile to off-shell contributions and hence a model discrimination between the two prime examples SUSY and UED is in danger.

Hadronic angular correlations The same study that governed the gluino shape asymmetries also had a closer look upon angular correlations of purely hadronic nature inside a single decay cascade. More precisely the azimuthal angle distance $\Delta\phi_{bb}$ as well as the average pseudo-rapidity $\bar{\eta}_{bb}$ of the two bottom quarks in the decay cascades both are analyzed for discrepancies between the two fundamentally different models of SUSY and UED [41].

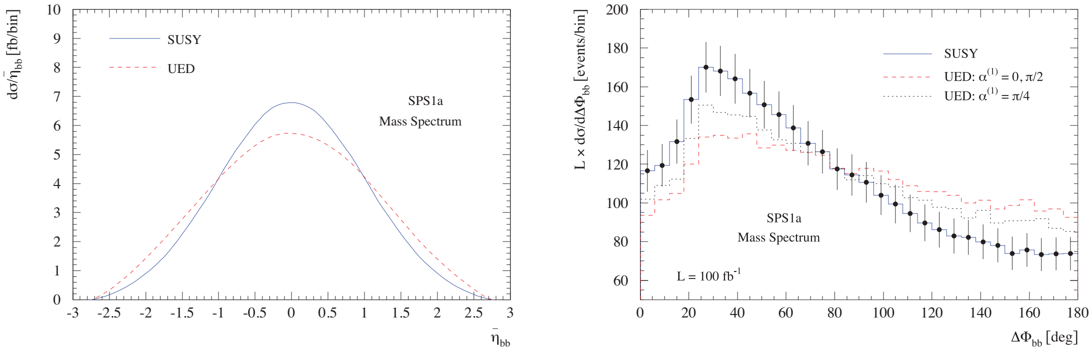

(a) (b)

Figure 2.6: Purely hadronic correlations in a single decay cascade: average pseudo-rapidity (a) and azimuthal distance (b) of two bottom quarks. Blue solid (red dashed) lines denote the SUSY (UED) model both for an underlying SPS1a mass spectrum. Figures taken from [41].

Furthermore as Figure 2.6 already indicates these variables allow for additional asymmetries to be defined, which quantify the deviations between the two scenarios. For the average pseudo-rapidity $\bar{\eta}_{bb}$ the rather central behaviour of SUSY is confronted with a more flat distribution in the UED case. The approximate position of the intersection of both curves at $|\eta| \sim 1$ hence accounts for the definition of the asymmetry

$$A^{\pm}_{\eta} = \frac{N(|\bar{\eta}_{bb}| < 1) - N(|\bar{\eta}_{bb}| > 1)}{N(|\bar{\eta}_{bb}| < 1) + N(|\bar{\eta}_{bb}| > 1)}. \tag{2.48}$$

Equivalently for the azimthual distance one defines

$$A^{\pm}_{\phi} = \frac{N(\Delta\phi_{bb} < \pi/2) - N(\Delta\phi_{bb} > \pi/2)}{N(\Delta\phi_{bb} < \pi/2) + N(\Delta\phi_{bb} > \pi/2)} \tag{2.49}$$

based on the observation from Figure 2.6 (b), that the bottom quarks in the UED sample tend to have a stronger back-to-back behaviour. In Chapter 3 we will analyze both the pseudo-rapidity and azimuthal distance distributions as well as the resulting numerical values for the two asymmetries $A^{\pm}$ and $A^{\pm}_{s}$.

2.2.2 Inclusive Angular Distributions

In this section we present an inclusive method to measure the spin of sparticles based on a longitudinally boost-invariant variable, first introduced for the application to sleptons produced in pairs [42] and later applied to hadronic events of squark and gluino production [43]. The approach itself is inclusive in that it requires no exclusive decay cascade assignment but rather uses just the first two hard objects (leptons in [42] and jets in [43]).

$\cos\theta^*_{ll}$ The predictive power of spin determination methods based on exclusive decay chains (e.g. the golden chain) is reduced by model dependent assumptions such as particular mass hierarchies that allow for decay chains as the golden one to happen. Complementary approaches may help shed additional light upon the underlying fundamental nature of the new physics model in question. One such example is the polar angle of the initially produced particles. In the case of slepton pair production [42] for example, the dependence of the Drell-Yan cross section on the angular distribution is given by

$$\left.\frac{d\sigma}{d\cos\theta^*}\right|_{\mathrm{SUSY}} \propto 1 - \cos\theta^* \tag{2.50}$$

with θ^* defined as the angle between an incoming quark from the proton and an outgoing scalar lepton. For the case of UED, the equivalent process is KK-lepton pair production, whose fermionic nature results in a different angular dependence:

$$\left.\frac{d\sigma}{d\cos\theta^*}\right|_{\mathrm{UED}} \propto 1+\beta\cos\theta^* \tag{2.51}$$

where $\beta = (E^2_{l(1)} - M^2_{l(1)})/(E^2_{l(1)} + M^2_{l(1)})$ and $E_{l(1)}$ as well as $M_{l(1)}$ are the energy and mass of the corresponding first KK-lepton excitation in the centre-of-mass frame.

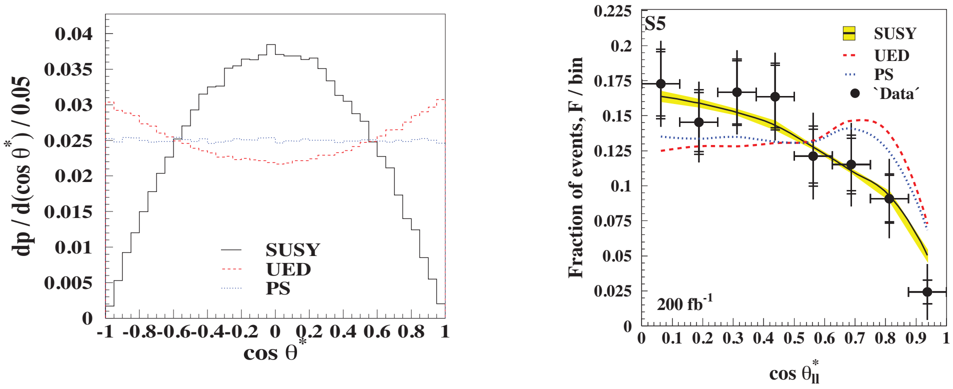

(a) (b)

Figure 2.7: Polar angle distribution (a) of initially produced sleptons and KK-leptons denoted by black solid and red dashed lines, respectively. The blue dotted lines correspond to pure phase space. Distributions of the variable $\cos\theta^*_{ll}$ (b) for SUSY (black-yellow solid line) and UED (red dashed line) cases as well as for a simulated SUSY *data* set for 200 fb^{-1}. Figures taken from [42].

Figure 2.7 (a) illustrates the apparent differences of both distributions. However due to the prompt decay into visible and invisible products, we are not able to reconstruct the complete initial momentum for models with conserved R- or KK-parity rendering these distributions unobservable. Hence in [42] a new variable was proposed for the slepton pair production process with subsequent prompt decay into lepton and LSP:

$$pp \to \tilde{l}\tilde{l}^* \to l^\pm \chi^0_1 l^\mp \tilde{\chi}^0_1. \tag{2.52}$$

This variable is defined as

$$\cos\theta^*_{ll} \equiv \tanh\frac{\Delta\eta_{ll}}{2} \tag{2.53}$$

where $\Delta\eta_{ll}$ is the pseudo-rapidity difference between the two leptons in the event. The motivation behind it is the fact that the first (observable) decay products, in this case the leptons, inherit some of the initially produced characteristics from their mothers, i.e. the scalar leptons or the fermionic KK-partners. It is furthermore longitudinally boost invariant and has an interpretation connecting it to $\cos\theta^*$: after a boost to the frame where both leptons have equal but opposite values of the pseudo-rapidity η, $\cos\theta^*_{ll}$ is the cosine of the angle between the lepton and the initial incoming quark, i.e. the beam axis. In Figure 2.7 (b) we present the distribution of $\cos\theta^*_{ll}$ from [42]. Despite the considerable size of errors, a discrimination of the SUSY from an UED model appears to be manageable.

$\cos\boldsymbol{\theta^*_{jj}}$ Lately the concept of the purely leptonic variable $\cos\theta^*_{ll}$ was adapted to hadronic events in [43]. Since slepton pairs are produced in an electro-weak process, its cross section at the LHC is orders of magnitudes smaller than the ones of coloured sparticles such as squarks and gluinos. Hence the motivation to translate the variable to a hadronic scenario with the initial goal of an early spin determination at 14 TeV and 1 fb^{-1}. The underlying principle is the same as in the electro-weak case discussed above: the initially produced particles exhibit a characteristic behaviour of the polar angle in the centre of mass frame of the hard process with respect to their spin quantum number.

In Figure 2.8 (a) this distribution for inclusive squark and KK-quarks exhibits remarkable discrepancies between the two fundamentally different models. While the SUSY part is rather flat and shows a minor rise in the upper positive regime of $\cos\theta^*$, the UED distribution is much more steep towards the ends and apparently favours the regions of high $|\cos\theta^*| \sim 1$. Unfortunately, again we are not able to observe this distribution. However, in [43] it was proposed to define an observable variable in full analogy to $\cos\theta^*_{ll}$

$$\cos\theta^*_{qq} \equiv \tanh\frac{\Delta\eta_{qq}}{2} \tag{2.54}$$

where $\Delta\eta_{qq} = q_1 - q_2$ is the pseudo-rapidity difference of two final state quarks q_1 and q_2. A parton level distribution of $\cos\theta^*_{qq}$ is depicted in Figure 2.8 (b) and illustrates

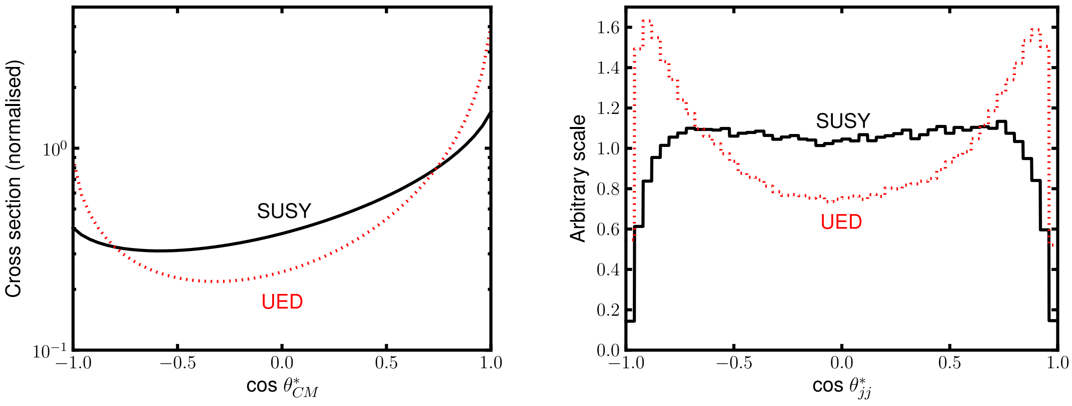

(a) (b)

Figure 2.8: Normalized polar angle distribution (a) of initially produced squark for SUSY (black solid line) and KK-quarks for UED (red dotted line). Inclusive parton level distribution of $\cos\theta^*_{qq}$ in the proton-proton centre of mass frame for SUSY (black solid line) and UED (red dotted line) at a 14 TeV LHC. Figures taken from [43].

the surviving differences of SUSY and UED signals.

This method is then further applied to fully inclusive hadronised SUSY and UED events originating not only from squarks and KK-quarks but also from gluinos and KK-gluons, respectively. Although different, the strength of deviation of the colour-octet signals from gluinos and KK-gluons is somewhat smaller than from squarks and KK-quarks [43]. Nonetheless the inclusive signatures consisting of at least two hard jets allow for a spin discrimination at an early stage of a 14 TeV LHC. In Chapter 3 we will analyse the impact of off-shell contributions on the gluino sub-channel and investigate to what extent a possible distortion can threaten the discriminative power of this method.

Summary

The purpose of this chapter was a brief introduction to the development of some cornerstones of spin and mass determination procedures in recent years. For the mass measurements we discussed several exclusive and inclusive variables and highlighted the connection between their endpoints and the involved masses of new physics particles. Furthermore, we introduced a selection of spin determination methods allowing for the discrimination of two fundamentally different straw-models: SUSY and UED. Where relevant, we also pointed out typical complications that arise with these measurements, both of experimental or more fundamental nature. In the next Chapter we will analyse most of the methods introduced here with respect to their tendency to be affected by off-shell contributions from a fat gluino.

Chapter 3

Off-shell Effects in Decay Cascades

The phenomenological importance of off-shell effects in decay cascades of new physics signals as well as their impact on existing mass and spin determination methods is not to be underestimated, if the width Γ of any intermediate or mother particle is of the order of a few percent of its mass M. In such scenarios these effects do not arise from three-body decays through virtual particle exchange but from non-resonant propagator contributions far away from the mass shell that allow for distorting effects in invariant masses and other kinematic observables. Hence in this chapter, we generically investigate to what extent existing approaches to measure masses and spins are affected. We furthermore quantify any observable deviation through the introduction of phenomenological parameters and analyse these in a generic benchmark scenario.[1]

3.1 Motivation

The narrow-width approximation (NWA) is a very powerful tool for the calculation of complex processes since it constitutes a consistent framework for the factorisation of production and decay under the assumption of negligible non-resonant contributions. Following the idea of factorisation, the NWA seperates the production of (unstable) particles and their successive decay into two processes, connected through a Breit-Wigner propagator $\frac{N(q)}{q^2-m^2+im\Gamma}$, where q is the four momentum, m the mass and Γ the width of the associated intermediate particle. The exact form of $N(q)$ furthermore depends upon the quantum numbers of the intermediate state. In a nutshell,

---

[1] By the time of publishing, the results presented in this chapter are also available as preprint [62].

the factorisation of phase space and the full matrix elements (ME) squared allow for the division of the amplitude into production- and decay-part connected through a Breit-Wigner-propagator. The latter is integrated out under the condition of small widths Γ and a negligible dependence of the production and decay cross sections on the intermediate particle momentum q [63]:

$$\begin{aligned}
\sigma_{full} &= \int d\Phi \overline{\sum} |\mathcal{M}|^2 && (3.1)\\
&\simeq \Big(\int d\Phi_p \overline{\sum_d} |\mathcal{M}_p|^2\Big) \int \frac{dq^2}{2\pi} \frac{1}{(q^2-m^2)^2+m^2\Gamma^2} \Big(\int d\Phi_d \overline{\sum_d} |\mathcal{M}_d|^2\Big) && (3.2)\\
&\simeq \sigma_p \times \int \frac{dq^2}{2\pi} \frac{2m}{(q^2-m^2)^2+m^2\Gamma^2} \times \Gamma_d && (3.3)\\
&\simeq \sigma_p \times \frac{\Gamma_d}{\Gamma} \equiv \sigma_p \times \mathrm{BR} && (3.4)\\
&= \sigma_{NWA}. && (3.5)
\end{aligned}$$

As the intermediate particle is put on-shell, non-resonant off-shell contributions and interference effects are neglected and spin- and polarisation correlations have to be treated separately. Except for a handfull of resonant processes such as $e^+e^- \to W^+W^- \to 4f$ [64], the NWA has so far been very successful in reducing complexity for nearly all SM processes while retaining good accuracy. However, in general BSM scenarios this is not necessarily always the case [45, 65] and it was shown in [46] that a breakdown of the NWA is imminent, if any of the five criteria is violated:

1. $\Gamma \ll M$ (small total width compared to mass, e.g. ρ-resonance)
2. $m \ll M$ (daughters lighter than mother, e.g. near-degenerate scenarios such as UED)
3. $M \ll \sqrt{s}$ (cm energy larger than mass, e.g. threshold-effects)
4. no interference (e.g. overlapping decay modes of particles)
5. separable propagator from ME (e.g. non-trivial spectral density / unparticles)

For obvious reason, all of these points may not always be fulfilled simultaneously. Disregarding this fact, most existing studies and simulations of new physics still rely on the factorisation based on the NWA, not least since the level of complexity due to long decay cascades and the sheer number of final state particles is very high. The classical NWA was later supplemented by improved versions [66, 67], whose error is of $\mathcal{O}(\Gamma/M)$. Regardless of these enhancements, the more precise but at the same time also more complex way of simulating new physics is to use the full matrix element were possible.

In the following, we study to what extent the NWA is super-seeded by the full ME calculation and how emerging differences impact the measurement of relevant model parameters. As a foundation block, we choose to use the gluino as a prototype. It has several beneficial characteristics, which make it a valuable candidate for the analysis of off-shell contributions in decay cascades. First of all, if the gluino mass is not too high, it will be copiously produced at the LHC due to its coloured nature. Furthermore, it is an ideal parent particle as a starting point for rich decay patterns in long cascades. Moreover, in scenarios with light(er) squarks, a whole plethora of decay modes may naturally inflate the total width of the gluino to large ratios Γ/M of up to 10 percent or more [2]. This effect might be additionally enhanced by pure phase space kinematics, when the mass gap between the gluino and the squarks is of the size of several hundred GeV. In the SM the largest ratio Γ/M corresponds to the W boson with a value of 2.5 %, for which the NWA is known to be insufficient for a couple of processes [64].

In the applications to be studied, we will probe the amount of off-shell contributions in terms of the phenomenological width-to-mass ratio

$$\gamma \equiv \Gamma/M, \tag{3.6}$$

also later on denoted as the effective or relative width. In the next sections we will introduce our setup in detail and explain the steps we will undertake so as to quantify the size of the distortion for different values of γ before discussing the impacts on a selection of mass and spin determination methods.

3.2 Simulation Setup and Benchmark Model

For the analyses of off-shell effects on endpoint and shape measurements of invariant mass distributions, we rely on several assumptions briefly mentioned in Chapter 2. One major condition is the existence of a specific mass hierarchy. The so-called *golden*

---

[2] Although disfavoured by recent LHC results, the theoretical upper-limit of Γ/M for quasi-massless squarks is 32 %

chain for instance requires the following mass pattern in order for all two-body decays to be kinematically allowed:

$$m_{\tilde{q}_L} > m_{\tilde{\chi}_2} > m_{\tilde{l}_R} > m_{\tilde{\chi}_1}. \tag{3.7}$$

Early mSUGRA scenarios such as *SPS1a* [68] inspired the presence of this type of hierarchy. Consider for example a slight in- or decrease of the second-to-lightest neutralino mass m_{χ_2}. On one hand this would allow for an additional intermediate state in the cascade, e.g. the heavier of the two sleptons, which would consequently mean a superposition of two endpoints for the same exclusive final state. Alternatively this might result in a subsequent three-body decay with completely different kinematic behaviour. It is in that sense, that parameter determination for such assumptions is very sensitive with respect to slight changes of the hierarchy due to the position of the second-to-lightest neutralino mass in between the ones of the two scalar lepton states.

For the study of gluino width effects we choose to concentrate on the two main production processes

$$pp \to \tilde{g}_1\tilde{g}_2 + X \tag{3.8}$$

$$pp \to \tilde{g}_1\tilde{q}_{L/R} + X \tag{3.9}$$

where in the first case of gluino pair production (equation (3.8)) one of the two signal gluinos decays into two down quarks and the lightest neutralino while the other one decays into two bottom quarks and a second-to-lightest neutralino, which further decays via an intermediate (right handed) slepton to two corresponding leptons and a lightest neutralino:

$$\tilde{g}_1 \to b\tilde{b}_i \to b\bar{b}\tilde{\chi}_2^0 \to b\bar{b}l^\pm\tilde{l}_R^\mp \to b\bar{b}l^\pm l^\mp\tilde{\chi}_1^0 \tag{3.10}$$

$$\tilde{g}_2 \to d\tilde{d}_L \to d\bar{d}\tilde{\chi}_1^0 \tag{3.11}$$

Notice the index i at the bottom squark owing to the fact, that we include both decay modes of the gluino into $\tilde{b}_1$ and $\tilde{b}_2$. In the second case of squark-gluino associated production (equation (3.9)), we simulate the prompt squark decay into a quark and the lightest neutralino

$$\tilde{q}_{L/R} \to q\tilde{\chi}_1^0. \tag{3.12}$$

With the focus on this particular final state we omit additional complications from combinatorial ambiguities. It allows us to study the consequences of off-shell effects without having to suffer from SUSY or combinatorial backgrounds, both will be discussed and analysed later on in Chapter 4.

The last decay steps in the cascade of equation (3.10) are particularly well-known: they inherit from the *golden chain* with the replacement of a (first or second generation) squark by a sbottom: $\tilde{q}_L \to \tilde{b}_i$. This exclusive final state allows for a quite generic study of most of the methods introduced in Chapter 2 while in principle simultaneously reducing combinatorial mis-assignments due to the possibility of b-tagging. Furthermore, in the analysis of off-shell gluino width effects we are able to use methods based on the existence of sbottoms in the cascade introduced in the last chapter.

In the following we introduce a benchmark scenario that meets the existence criteria of our signal decay chain while capturing most of the relevant phenomenological features (Higgs mass of 125 GeV, heavy coloured scalars and rich decay patterns). To be as generic as possible, we decided to make use of the phenomenological MSSM (or pMSSM) with 19 free parameters introduced in chapter 1, for which all model parameters are given in Table 3.1. Moreover, the mass hierarchy of equation (3.7) is assured and the branching ratios of the four successive two body decay steps are of considerable size:

$\tilde{g}$	$\to b\tilde{b}_1$	10 %	$\tilde{b}_1$	$\to b\tilde{\chi}^0_2$	16 %	$\tilde{\chi}^0_2$	$\to e^\pm \tilde{e}^\mp_R$	42 %	$\tilde{e}^\pm_R$	$\to e^\pm \tilde{\chi}^0_1$	100 %
$\tilde{g}$	$\to b\tilde{b}_2$	07 %	$\tilde{b}_2$	$\to b\tilde{\chi}^0_2$	34 %	$\tilde{\chi}^0_2$	$\to \mu^\pm \tilde{\mu}^\mp_R$	42 %	$\tilde{\mu}^\pm_R$	$\to \mu^\pm \tilde{\chi}^0_1$	100 %

Summing up, the total branching fraction of our exclusive final state from signal gluinos decaying through the *benchmark* cascade is roughly 7 %. This number has to be interpreted with care for the following reason: the underlying concept of cross sections times branching ratio as within the NWA is a good approximation if off-shell contributions are suppressed due to small widths. However, in this study we investigate the effects arising from precisely these kind of contributions far away from the resonant pole of the propagator. A complete treatment should (at least) take into account fully differential four-particle final states or more. Since we use these figure merely as crude estimates for the appraisal of the actual number of events we expect from our exclusive decay cascade final state, we refrain from such a calculation. All masses of the spectrum were calculated using `SOFTSUSY` [69] while the particle decay widths were obtained with `SUSYHIT` [70]. An overview of all model parame-

M_1	M_2	M_3	A_t	A_b	A_τ	μ	M_A	$m_{\tilde{l}_L}$	$m_{\tilde{\tau}_L}$
150	250	1200	4000	4000	0	1500	1500	1000	1000

$m_{\tilde{l}_R}$	$m_{\tilde{\tau}_R}$	$m_{\tilde{q}_L}$	$m_{\tilde{q}^3_L}$	$m_{\tilde{q}^u_R}$	$m_{\tilde{q}^d_R}$	$m_{\tilde{t}_R}$	$m_{\tilde{b}_R}$	$\tan\beta$	
200	1000	1000	1000	1000	1000	4000	1000	10	

Table 3.1: Model parameters of the pMSSM under investigation. All figures (except $\tan\beta$) are in units of GeV.

ters is given in Appendix B. With the mass spectrum given, we use the obtained SLHA [71] file to calculate the relevant cross sections using `PROSPINO` [72], which are squark-gluino associated production (376.0 fb), gluino pair production (47.6 fb) and neutralino gluino associated production (3.7 fb). The sum we multiply by the total branching fraction of our exclusive final state (7 %) to arrive at an event number of roughly 9000 for an overall integrated luminosity of 300 fb^{-1}. Several diluting effects such as detector acceptance, b-tag efficiencies and event selection criteria may further reduce this figure, which is why we choose to analyse an event number of 5000. The following simulations are based on the most recent version of `WHIZARD` [73, 74]. All generated events were exported to HepMC [75] format and furthermore passed through a C++ analysis framework based on ROOT [76], which we specifically developed and tailored to the investigation of deviations from off-shell contributions in spin and mass determination methods.

In the following we concentrate on studies based on the parton level. The effects we are about to show are of very fundamental nature stemming from off-shell contributions of propagators in simple matrix elements. For this reason it is convenient to show deviations explicitly before other polluting aspects such as initial- and final state radiation, hadronisation and detector resolution distort the picture. The consequences of a broad gluino, whose width is of considerable size with respect to its mass, are investigated by simulating the production and decay of the first part using the full matrix element. More precisely the first part of equation (3.10) is completely calculated in one step

$$pp \to (b\bar{b}\tilde{\chi}^0_2) + (\tilde{g}/\tilde{q}) \tag{3.13}$$

including all contributions, whereas the successive decays of the second-to-lightest neutralino and the *spectator* gluino or squark are factorised with full spin correlations using the NWA. Furthermore, the phenomenological width-to-mass ratio $\gamma = \Gamma/M$ is scanned over using the values

$$\gamma \in \{0.5\%, 2.5\%, 5.0\%, 10.0\%, 15.0\%\}. \tag{3.14}$$

This set is chosen so as to resemble a broad range of possible width, which might be realised in nature. The particular reasoning behind the range will be discussed in the beginning of the next section. Using this relative width γ we study the impact of off-shell contributions on a choice of mass and spin determination methods inaugurated in Chapter 2.

3.3 Off-shell Effects in Mass Measurements

We begin our investigation with the study of several mass measurement variables. A sizable value of the width-to-mass ratio γ and hence a large width Γ in the gluino propagator affects the momenta of both the intermediate sbottom and the near (bottom) quark b_n. The far bottom quark b_f on the other hand is expected to receive only a minor contribution and thus should not distort invariant mass distributions. Figure 3.1 depicts the transverse momenta of both near and far bottom quark and their distortion with respect to different values of γ. The black (solid), red (short-dashed), green (dotted), blue (short-dashed-dotted), yellow (long-dashed-dotted), magenta (long-dashed-double-dotted) and cyan (long-dashed) line correspond to $\gamma = 0.5$ %, 2.5 %, 5.0 %, 10.0 %, 15.0 %, 20.0 % and 25.0 %, respectively. We observe that the near bottom quark exhibits a non-vanishing distortion visible by eye. While there is an obvious tendency for increasing distortion within the first five values of γ, the two largest effective widths exhibit only a slight increase. These values are anyhow to some extent academic, since in scenarios with realistic aspirations they are hard if not impossible to realise. However, we included them to illustrate the effect of moderate saturation. This motivates us to leave out the two highest values $\gamma = 20.0\%$, 25.0 % and from now on investigate the earlier introduced range of values up to 15 %. Turning to the far bottom quark, we notice that it is merely affected by the off-shell contributions. Hence, we choose to restrict our investigation of observables introduced in Chapter 2 to a subset containing the near quark b_n:

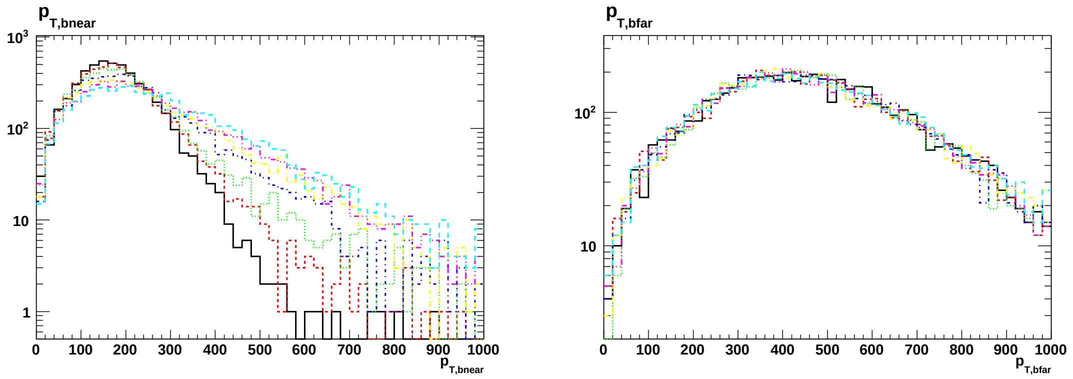

Figure 3.1: Transverse momenta of the two (near and far) bottom quarks in the signal cascasde. The different line types and colours correspond to different values of γ as discussed in the text.

$$\{m_{bb}, m_{b_nl,low}, m_{b_nl,high}, m_{bbl,low}, m_{bbl,high}, m_{b_nll}, m_{bbll}\}.$$

3.3.1 Exclusive Cascades

m_{bb} The first mass edge we study is the classical dijet endpoint of the first gluino decay step. Due to the scalar propagator of the intermediate bottom squark, we expect to see no effects of spin correlation in that the shape of the distribution resembles the well-known triangular nature of the di-lepton edge with a linear rise from 0 to $m_{bb}^{\max}$, where a sharp cutoff marks the endpoint. Figure 3.2 (a) shows the simulated distri-

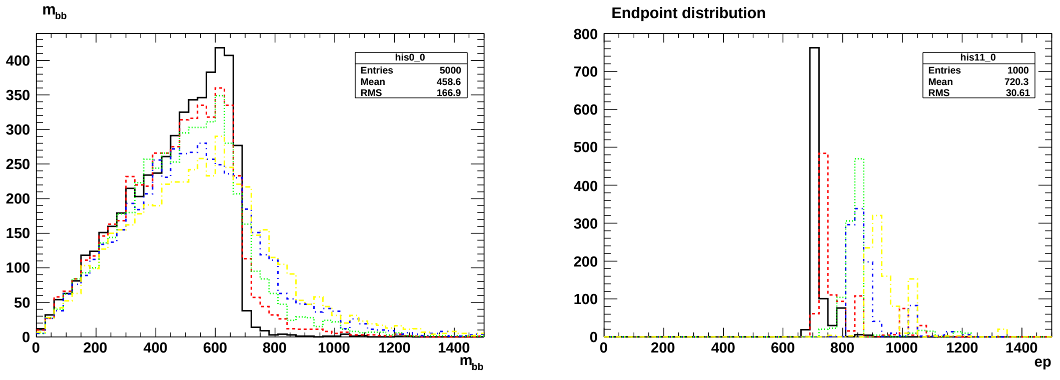

(a) (b)

Figure 3.2: (a) Invariant dijet mass of two bottom quarks from the gluino decay for different values of γ (see text for details). (b) Distribution of endpoints obtained as fit parameters of the Edge-to-Bump method.

butions for five different values of γ, where the line colour correspondence is the same as above. Notice the very small deviation of the solid black line from the idealised triangular shape, which is a direct consequence of the relative narrow width: $\gamma = 0.5$ %. The situation drastically changes when the width is incrementally increased: the distortion steadily grows and starts to wash out the clear cut edge structure with increasing γ. At high values of γ (≥ 5 %) the distribution acquires an irreducible tail, which mimics other distorting effects such as combinatorial mis-assignments or detector smearing already at this early parton level stage. However, we again want to stress the fact, that this kind of deviation from off-shell contributions is irreducible in the sense, that it cannot be tuned away e.g. by other methods designed to minimize combinatorial problems or a *perfect* detector resolution.

In the next step it is our goal to quantify these intrinsic contributions by estimating the distortion of the shape at the vicinity of the endpoint as a function of the effective width-to-mass ratio γ. The tool of our choice for this study is the Edge-to-Bump method [61] introduced in Chapter 2. It allows us to extract the edge information and to discriminate different endpoint behaviours in an unbiased way. In a nutshell, the approach fits a naive linear kink function (cf. equation 2.38) $\mathcal{O}$ (1000) times and returns bumps at the most likely positions of kinks (supposedly physical edges) in the original distribution.

As a first estimate of the impact of width effects on the measurement, we consider the shift of the actual endpoint position with respect to the value of γ. Table 3.2 discloses these values obtained with our own implementation of the method described in Chapter 2. The according distributions are depicted in Figure 3.2 (b). While for small effective width of 0.5% the obtained value (708 GeV) is close to the theoretical one (679.6 GeV), the endpoint positions for large values of γ are off by more than 200 GeV (920 GeV) using the same method and settings.

An alternative but related measure for the endpoint smearing is given by the size of the corresponding error estimates. Their increase with respect to γ reflects the observation that the spread of endpoint values in Figure 3.2 (b) is considerably enhanced for an increased effective width. While for $\gamma = 0.5\%$ the purely statistical error is small, the sheer growth of the standard deviation for $\gamma = 15.0\%$ by nearly two orders of magnitude serves as another good indication for a huge endpoint smear. This raises an important point: the overly high confidence expressed through the small errors of endpoints for low values of γ is a mere binning effect and does not represent a realistic error estimate for sophisticated endpoint measurements. Moreover these error estimates of the Edge-to-Bump method are purely statistical and reflect the transformation of a statistical uncertainty on an endpoint position onto the particular position of a mean value in a distribution of fit results. Since the binning of a histogram is furthermore bounded by experimental resolutions, a relatively large minimum bin size results in a systematic underestimation of the given errors.

The usage of the endpoint position as a measure for distortion is based on just one fit parameter (p_4) of the Edge-to-Bump method. Yet, a detailed observation of the fitting function from equation (2.38) suggests to make use of the parameters p_2 and p_3, which are the two linear slopes. Notwithstanding the fact, that the off-shell contributions tend to wash out the sharp edge and lead to smoother and longer tails, we propose to use the following variables as a measure to quantify the amount of distortion:

$$s_d = |p_3 - p_2| \tag{3.15}$$

$$s_r = |p_2/p_3| \tag{3.16}$$

These are the difference (s_d) and ratio (s_r) of the two slopes. For each fit, both values are calculated from the parameters returned by the Edge-to-Bump method. Ideally for a pure phase space distribution of triangular shape and no smearing beyond the sharp cutoff, the first slope is infinite and the second slope zero, ergo the slope difference maximal (infinite) and the slope ratio minimal (zero). In that sense, the difference in slopes measures the strength of a kink in the distribution whereas the ratio returns information about the size of the second slope relative to the first one. A ratio close to zero may thus be attributed to a tail-less distribution such as the triangular shaped one. Keep in mind, that due to the sanity checks of our method, $|p_2| < |p_3|$ and hence $s_r \in (0, 1)$. The full treatment of large width effects on the other hand introduces a tail and smears the endpoint behaviour, which gives rise to considerably smaller slope differences and higher slope ratios. If the returned fit value of such a slope difference is compatible with zero, the underlying distribution apparently lacks robust kinky features. Extraction of such shallow endpoints is therefore a very delicate task.

In Table 3.2 we collect results for the slope differences and ratios of the invariant di-bottom mass for all five values of γ. In Figure 3.3 we notice the impact of the different values of γ: while we observe slope differences well above one and small slope ratios compatible with zero for small γ, at an effective width of already 5 % the mean $\bar{s}_d$ is reduced to a value smaller than one. The slope ratio exhibits an equivalent behaviour: the mean value $\bar{s}_d$ is increased by a factor of 10.

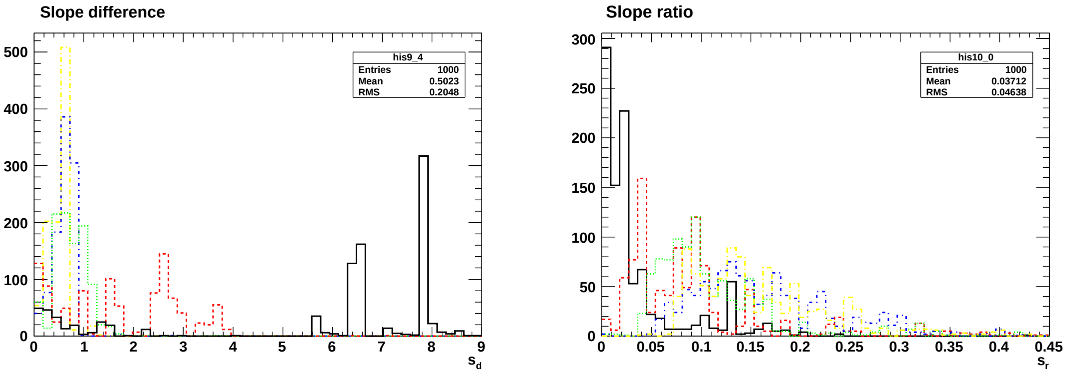

(a) (b)

Figure 3.3: Statistically distributed slope differences (a) and ratios (b) for m_{bb} obtained as fit parameters of the Edge-to-Bump method.

γ [%]	$\bar{m}_{bb}^{\max}$	$\bar{s}_d$	$\bar{s}_r$
0.5	708.5 ± 0.9	5.70 ± 2.90	0.014 ± 0.008
2.5	740.9 ± 2.5	1.71 ± 1.17	0.064 ± 0.028
5.0	835.7 ± 19.2	0.78 ± 0.24	0.084 ± 0.023
10.0	886.5 ± 13.0	0.67 ± 0.08	0.141 ± 0.045
15.0	921.3 ± 25.9	0.62 ± 0.04	0.131 ± 0.035

Table 3.2: Adapted mean values of endpoint positions (in GeV), slope differences (in 1/GeV) and slope ratios for invariant di-bottom mass m_{bb}.

$m_{b_n l}$ The next mass edges under investigation are the minimisation and maximisation over two possible lepton combinations with the near bottom quark. Recall the definitions

$$m_{b_n l,low} = \min\left[m_{b_n l^+}, m_{b_n l^-}\right] \tag{3.17}$$

$$m_{b_n l,high} = \max\left[m_{b_n l^+}, m_{b_n l^-}\right] \tag{3.18}$$

and their endpoints given in equations (2.16) and (2.17). By the very nature of the intermediate particles, there is a small correlation of the leptons and the bottom quark, that manifests itself in the shape of the distributions. Hence with no pure

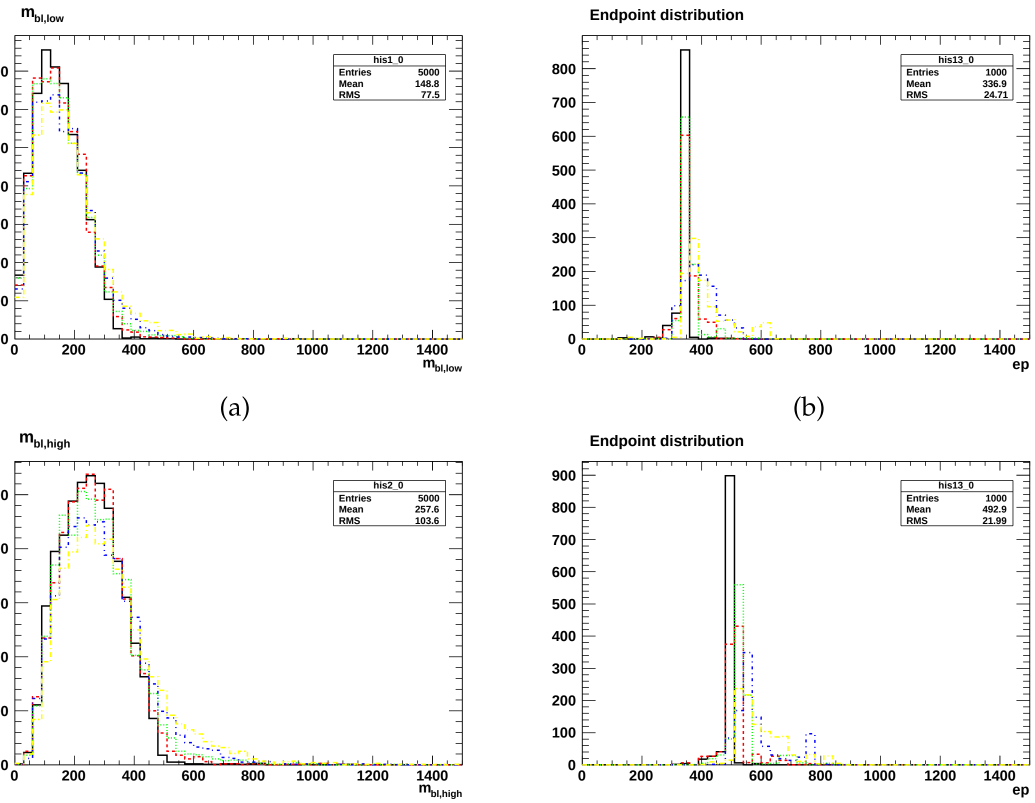

(a) (b)

(c) (d)

Figure 3.4: Left: Invariant mass of near bottom quark and leptons, varied as defined by $m_{bl,low}$ (a) and $m_{bl,high}$ (c) for different values of γ (see text for details). Right: Distribution of the corresponding endpoints obtained as fit parameters of the Edge-to-Bump method for $m_{bl,low}$ (b) and $m_{bl,high}$ (d).

phase space shape, we expect the distortion to be less pronounced in comparison to the invariant di-bottom mass. Especially $m_{b_n l,low}$ should not contain too much excess events in the upper parts, since these contributions will mostly be omitted due to the minimisation procedure. The variable $m_{b_n l,high}$ on the other hand will severely be affected for the very same reason. The distributions in Figures 3.4 (a) and (c) confirm these assumptions. The extracted endpoints depicted in Figures 3.4 (b) and (d) and Table 3.3 also support this statement: while for $m_{b_n l,low}$ the overall endpoint variation with respect to γ is about 40 GeV, $m_{b_n l,high}$ suffers from more than twice the endpoint shift with a value of about 80 GeV. Comparing this to the *theoretically* expected edge positions

$$m^{\max}_{b_n l,low} = 364.4 \text{ GeV} \tag{3.19}$$
$$m^{\max}_{b_n l,high} = 493.1 \text{ GeV} \tag{3.20}$$

calculated from equations (2.16) and (2.17), we find that the discrepancy for $m_{b_n l,low}$ is small and mostly in agreement with the expectation. For $m_{b_n l,high}$ however, the end-point deviance is as large as 15%. The adapted slope differences $\bar{s}_d$ show a similar picture: while the numbers of the minimised distributions exhibit only a mild overall decline, the maximised version illustrates an apparent tendency of $\bar{s}_d$ to decrease with rising γ. As for the slope ratios $\bar{s}_r$, the same holds but to an even greater extent, in that for $m_{bl,low}$ the three intermediate ratios are all in the same ballpark whereas for $m_{bl,high}$, $\bar{s}_r$ increases by nearly one order of magnitude.

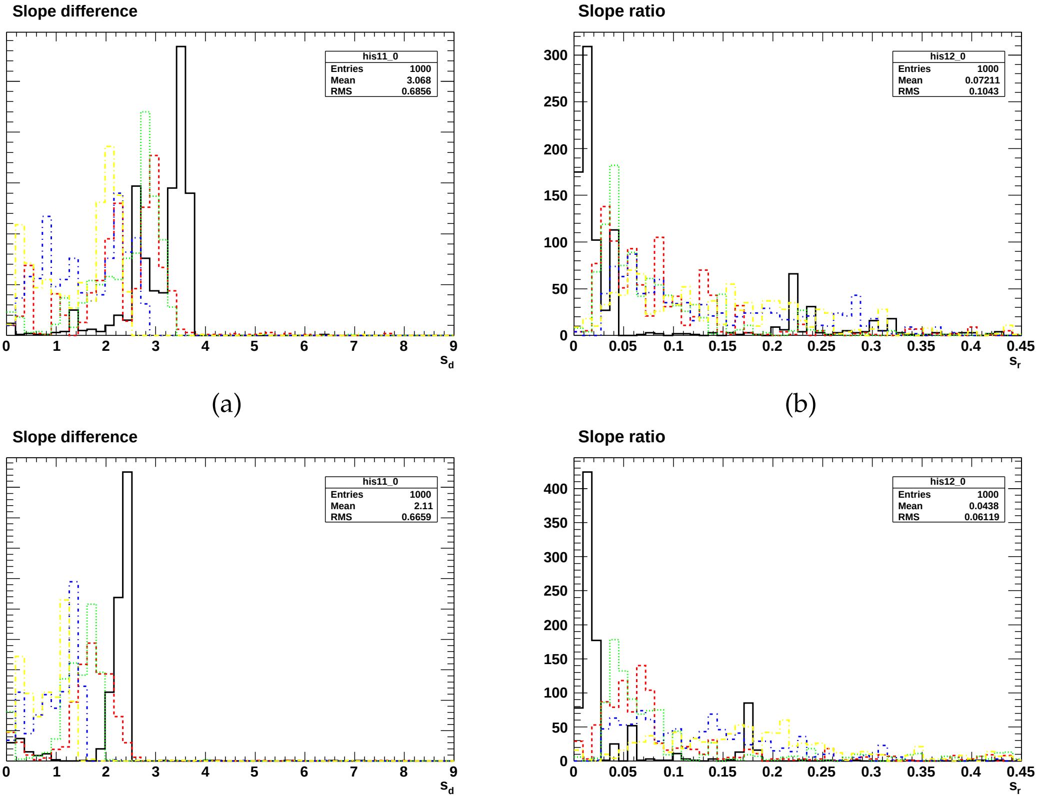

(a) (b)

(c) (d)

Figure 3.5: Statistically distributed slope differences (left) and ratios (right) for $m_{bl,low}$ (a)/(b) and $m_{bl,high}$ (c)/(d) obtained as fit parameters of the Edge-to-Bump method.

γ [%]	$\bar{m}^{\max}_{bl,low}$	$\bar{s}_d$	$\bar{s}_r$	$\bar{m}^{\max}_{bl,high}$	$\bar{s}_d$	$\bar{s}_r$
0.5	341.4 ± 6.7	3.25 ± 0.38	0.014 ± 0.007	499.8 ± 0.3	2.35 ± 0.03	0.017 ± 0.005
2.5	356.6 ± 2.7	2.58 ± 0.47	0.055 ± 0.025	511.2 ± 3.6	1.80 ± 0.26	0.055 ± 0.018
5.0	355.5 ± 1.8	2.82 ± 0.25	0.041 ± 0.011	527.0 ± 11.9	1.55 ± 0.25	0.054 ± 0.017
10.0	383.0 ± 39.6	1.59 ± 0.77	0.066 ± 0.024	556.3 ± 13.4	1.00 ± 0.44	0.103 ± 0.048
15.0	377.2 ± 22.3	1.47 ± 0.74	0.124 ± 0.069	579.0 ± 47.9	0.79 ± 0.40	0.158 ± 0.059

Table 3.3: Adapted mean values of endpoint positions (in GeV), slope differences (in 1/GeV) and slope ratios for $m_{bl,low}$ and $m_{bl,high}$.

m_{bbl} Extending the *low*- and *high*-type invariant masses from above with the additional (far) bottom quark, we arrive at a three-particle invariant mass, that has a similar feature as the ones just discussed: an intermediate neutralino propagator communicating spin correlations and allowing for a similarly altered shape compared to the triangular phase space. If we now start to gradually increase the effective width parameter γ, the off-shell contributions start to enter the game in a more severe way as for $m_{bl,low}$ and $m_{bl,high}$. This can be understood in terms of the inclusion of nearest neighbours: since the invariant di-bottom mass is heavily distorted by width effects and it is always included in both $m_{bbl,low}$ and $m_{bbl,high}$, we expect to observe large deviations. In that sense and in contrast to $m_{bl,low}$, the minimisation procedure over two possible lepton combinations is not able to suppress the appearance of these intrinsic contributions as given in Figure 3.6. Regarding the shift of edge positions, the situation is comparable to the case of m_{bb}: both $m_{bbl,low}$ and $m_{bbl,high}$ exhibit displacements of up to 150 and 180 GeV, respectively. For the highest value of $\gamma = 0.15$ in Table 3.4, we notice an exceptionally small error estimate for the endpoint position of $m_{bbl,low}$ in contrast to an unusually large one for $m_{bbl,high}$. The reasoning behind this is a trivial matter of statistics as is evident from Figure 3.6: while the lower of the two invariant masses has a sharp drop at the bin corresponding to the endpoint position, the higher distribution has two such *fake* kinks at around 1100 and 1250 GeV, respectively. These are purely statistical issues happening by chance and attributed to the low overall number of events of 5000. Hence the gross under- and overestimation of the error estimates for both edges. The mean value however still captures the important feature of endpoint translation: a shift of the returned mean value of the Edge-to-Bump method of up to 180 GeV. Comparing these with the theoretically expected values

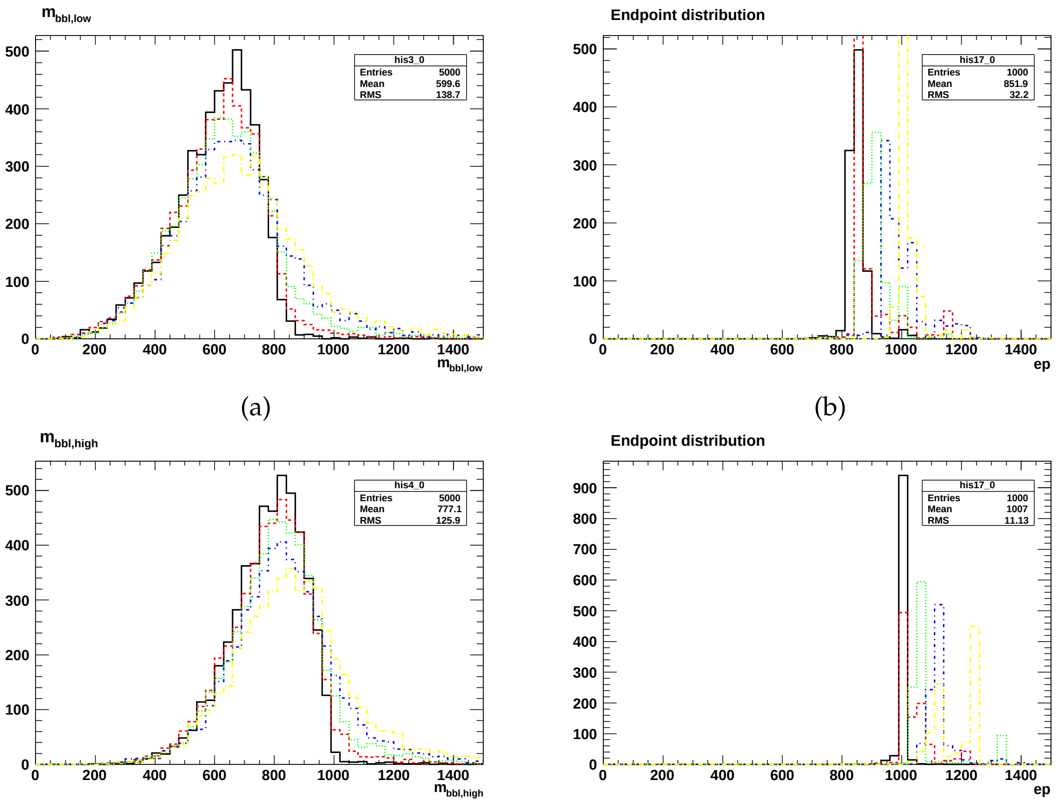

(a) (b)

(c) (d)

Figure 3.6: Left: Invariant mass of near bottom quark and leptons, varied as defined by $m_{bbl,low}$ (a) and $m_{bbl,high}$ (c) for different values of γ (see text for details). Right: Distribution of the corresponding endpoints obtained as fit parameters of the Edge-to-Bump method for $m_{bbl,low}$ (b) and $m_{bbl,high}$ (d).

γ [%]	$\bar{m}^{\max}_{bbl,low}$	$\bar{s}_d$	$\bar{s}_r$	$\bar{m}^{\max}_{bbl,high}$	$\bar{s}_d$	$\bar{s}_r$
0.5	845.2 ± 11.6	2.87 ± 0.50	0.025 ± 0.011	1009.7 ± 00.4	3.47 ± 0.10	0.009 ± 0.005
2.5	864.4 ± 02.2	1.79 ± 0.91	0.046 ± 0.020	1017.0 ± 01.7	2.11 ± 0.77	0.041 ± 0.012
5.0	900.8 ± 23.5	1.45 ± 0.22	0.067 ± 0.022	1060.0 ± 10.6	1.72 ± 0.32	0.050 ± 0.012
10.0	979.4 ± 34.8	0.62 ± 0.29	0.156 ± 0.051	1120.8 ± 11.3	0.94 ± 0.22	0.126 ± 0.031
15.0	1002.3 ± 4.9	0.71 ± 0.07	0.163 ± 0.041	1184.3 ± 62.9	0.63 ± 0.30	0.175 ± 0.052

Table 3.4: Adapted mean values of endpoint positions (in GeV), slope differences (in 1/GeV) and slope ratios for $m_{bbl,low}$ and $m_{bbl,high}$.

$$m^{\max}_{bbl,low} = 868.6 \tag{3.21}$$

$$m^{\max}_{bbl,high} = 996.6 \tag{3.22}$$

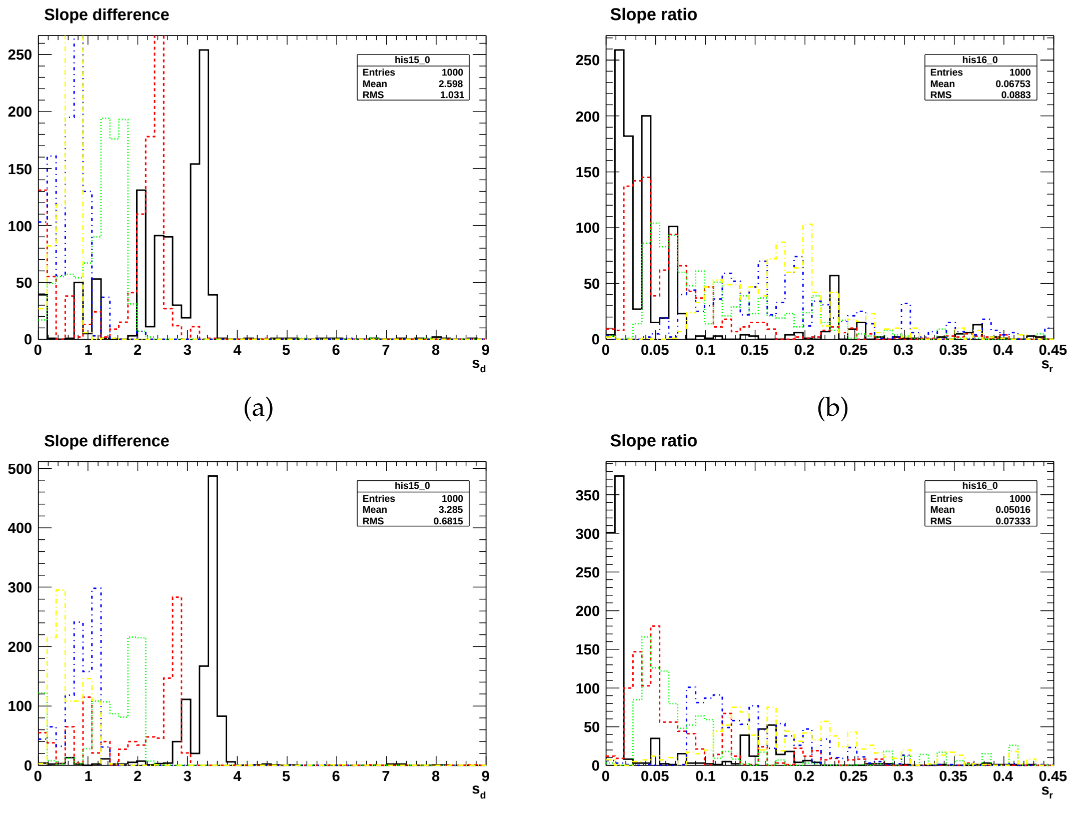

(a) (b)

(c) (d)

Figure 3.7: Statistically distributed slope differences (left) and ratios (right) for $m_{bbl,low}$ (a)/(b) and $m_{bbl,high}$ (c)/(d) obtained as fit parameters of the Edge-to-Bump method.

we again find agreement for small widths and large deviations for high values of γ. In Figure 3.7 and Table 3.4 the slope differences $\bar{s}_d$ (ratios $\bar{s}_r$) of the two variables both display a clear decreasing (increasing) trend for growing (falling) effective width factors γ and thus confirm our choice as a parameter quantifying the distortion strength.

$m_{b_n ll}$ The last three-particle invariant mass we investigate is the combination of the near bottom quark and the lepton pair. Without the particular need for distinction between the two leptons, we expect to observe a moderate distortion for large widths, which might be weakened by the fact that the first linear slope of the undistorted distribution is not maximally steep since $m_{b_n ll}$ is not built out of direct next neighbours. An example of a maximally steep endpoint behaviour is the undistorted invariant di-bottom mass, whose first slope parameter would ideally be infinite due to the triangular shape. Figure 3.8 (a) and (b) depict $m_{b_n ll}$ and the corresponding endpoint distributions, numerical values of which are given on the left-hand side of Table 3.5. Despite a fairly accurate endpoint estimate for up to $\gamma = 2.5\%$ in comparison with the theoretical value of 578.8 GeV, the maximal deviation of 100 GeV for huge widths is still of substantial size. The two slope parameters both behave similarly to what we have already seen with other invariant mass variables (cf. Figure 3.9): an average slope difference $\bar{s}_d$ of well above two is reduced to a value below one, that is compatible with zero within two standard deviations. For small widths, the slope ratio $\bar{s}_r$ is also close to zero but increasing γ results in a steady growth of $\bar{s}_r$ of more than one order of magnitude in size to values of up to 16 %.

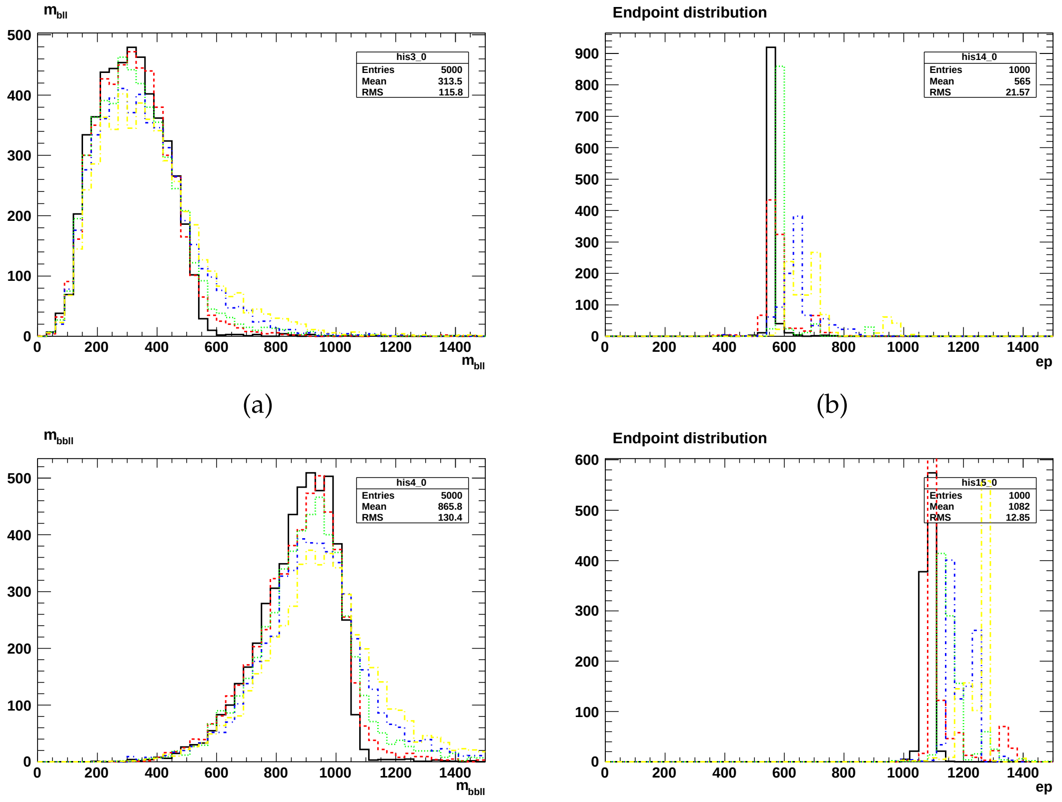

(a) (b)

(c) (d)

Figure 3.8: Left: Invariant mass of bottom quark(s) and leptons: $m_{b_n ll}$ (a) and m_{bbll} (c) for different values of γ (see text for details). Right: Distribution of the corresponding endpoints obtained as fit parameters of the Edge-to-Bump method for $m_{b_n ll}$ (b) and m_{bbll} (d).

γ [%]	$\bar{m}_{bll}^{\max}$	$\bar{s}_d$	$\bar{s}_r$	$\bar{m}_{bbll}^{\max}$	$\bar{s}_d$	$\bar{s}_r$
0.5	565.4 ± 1.7	2.37 ± 0.15	0.010 ± 0.002	1079.3 ± 2.4	4.64 ± 0.51	0.011 ± 0.009
2.5	568.5 ± 3.4	1.92 ± 0.08	0.080 ± 0.037	1105.1 ± 1.3	2.22 ± 1.22	0.035 ± 0.013
5.0	594.5 ± 2.0	1.56 ± 0.04	0.050 ± 0.012	1150.2 ± 19.9	1.34 ± 0.70	0.078 ± 0.020
10.0	640.0 ± 12.0	0.94 ± 0.25	0.142 ± 0.064	1193.7 ± 37.4	1.00 ± 0.44	0.163 ± 0.041
15.0	668.6 ± 40.5	0.65 ± 0.33	0.157 ± 0.050	1251.2 ± 30.9	0.78 ± 0.17	0.182 ± 0.036

Table 3.5: Adapted mean values of endpoint positions (in GeV), slope differences (in 1/GeV) and slope ratios for m_{bll} and m_{bbll}.

m_{bbll} Combining all objects from one cascade we obtain the variable m_{bbll}, which has a very clear cut endpoint and a steep edge structure, since it is constructed out of next neighbours. The sharper the drop of the distribution at the vicinity of the edge, the larger we expect the impact of off-shell contributions to be, even so if just one out of the four propagators, in our case the signal gluino, is affected. From Figure 3.8 (c) and (d), the amount of distortion may already be estimated by eye. A more quantitative statement is given in terms of numerical values on the right-hand side of Table 3.5. While the estimated endpoints for small values of γ are in gross agreement with the theoretically expected value of 1092.7 GeV, the largest deviation of $m_{bbll}^{\max}$ for $\gamma = 15\%$ is 172 GeV. A similar picture as for $m_{b_n ll}$ is found for the slope parameters (also cf. Figure 3.9): ranging from just below five down to well below one, the slope difference exhibits an even larger spread of values. The slope ratios on one hand are compatible with zero for the smallest width $\gamma = 0.5\%$ but on the other hand increase by a factor of 15 for the largest off-shell contribution.

3.3.2 Inclusive Approaches

M_{T2} Up to now, we only studied exclusive invariant mass variables, i.e. combinations of objects arising from one cascade side from a decay of just one single mother. In our case, this was taken to be the gluino, which has a large variety of possible decay patterns and consequently a plethora of interesting invariant mass combinations. Restricting the analysis to just one particular decay cascade entails several problems, the largest is presumably combinatorics. Consider for example the symmetric case of two identical decay chains of the type we have analysed so far, where not one, but two gluinos decay into two bottom quarks, two leptons and the lightest neutralino. All variables we have just discussed assume, that somehow a differentiation between

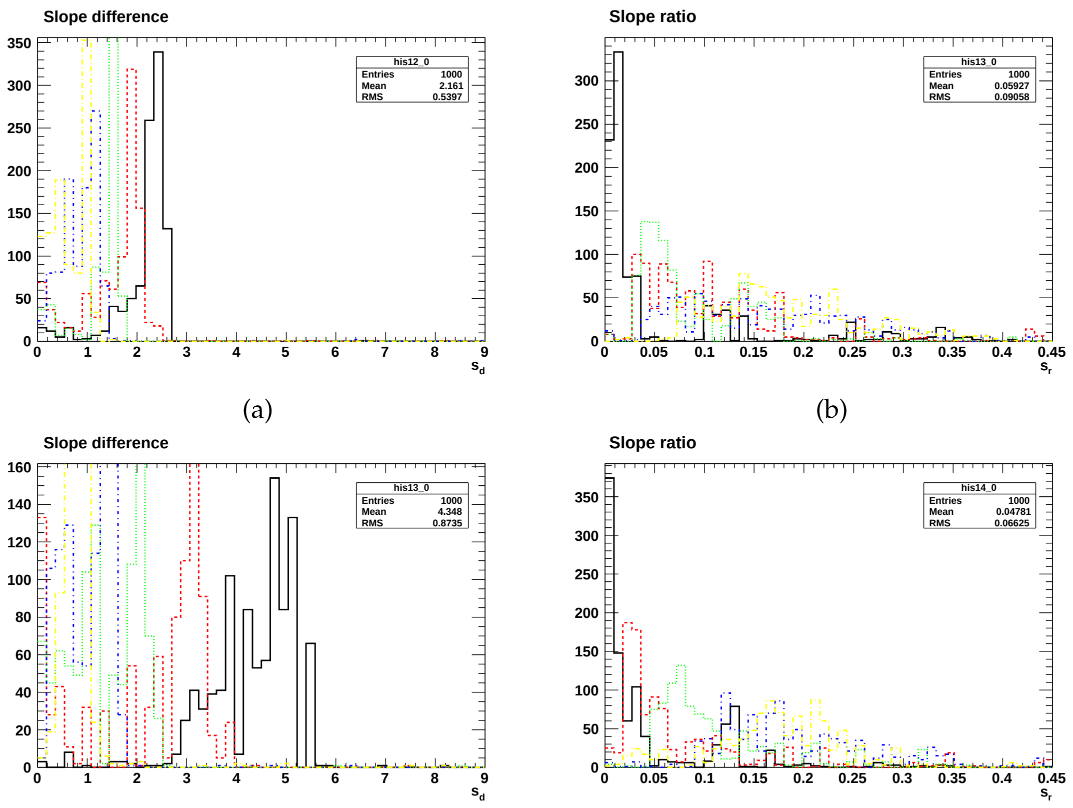

(a) (b)

(c) (d)

Figure 3.9: Statistically distributed slope differences (left) and ratios (right) for m_{bll} (a)/(b) and m_{bbbl} (c)/(d) obtained as fit parameters of the Edge-to-Bump method.

the two cascades is somehow given (e.g. the partitioning of four leptons into 2 × 2 leptons). However a priori there is no general recipe that always allows for such a correct assignment. This severely affects the usability of these exclusive variables and is known as the combinatorial problem.

An alternative, less exclusive approach is M_{T2} as introduced in the Chapter 2. Although M_{T2} is similarly affected by the combinatorial problem, since here the visible momentum has to be split into two separate sides as well, there exist methods, which address this issue[3] (cf. Chapter 2). In the remainder of this chapter we circumvent these kind of combinatorics through two non-identical decay chains, which allow us to concentrate on the effects of off-shell contributions. Hence, the partition of visible momenta into two sides for the application of $M_{T2}(p_{vis}^{(1)}, p_{vis}^{(2)}, \not{p}_T, m_\chi)$ is naively given

---

[3] e.g. $M_{T\mathrm{Gen}}$ [77], which is the minimum of M_{T2} for all possible momentum assignments into two partitions

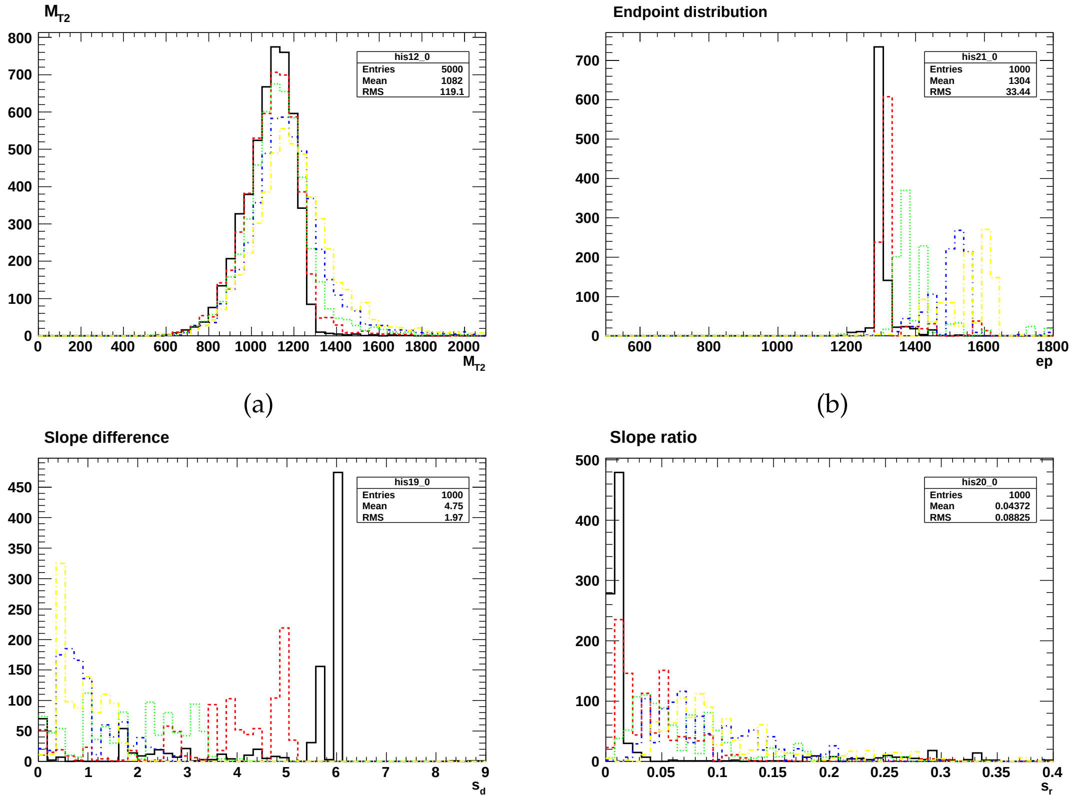

(a) (b)

(c) (d)

Figure 3.10: M_{T2} distribution (a) and its statistically distributed endpoints (b), slope differences (c) and ratios (d) obtained as fit parameters of the Edge-to-Bump method for five different values of γ.

by

$$p_{vis}^{(1)} = \{b, \bar{b}, l^{\pm}, l^{\mp}\} \tag{3.23}$$

$$p_{vis}^{(2)} = \{q, \bar{q}\} \tag{3.24}$$

where the light flavoured partonic jets are assigned to one side and the remaining objects to the other. The input test mass of the invisible sparticle was set to $m_{\chi} = 150$ GeV close to the true value of the benchmark scenario. Figure 3.10 (a) illustrates the impact of the effective width parameter γ on the distribution of M_{T2}: similar to the exclusive invariant mass variables discussed above, relative widths larger than 2.5 % result in substantial smearing and a long tail, which is absent at lower values. Owing to the general minimisation procedure of M_{T2}, the effect is somewhat smaller than for variables such as m_{bb} or m_{bbll}, which is supported by numerical values given in Table 3.6. The endpoint $M_{T2}^{\max}$ is given by the parenting sparticle mass, thus we expect to observe a clear edge structure at the gluino mass of 1277 GeV. Up to a slight overshoot, this is in gross agreement with the values given for $\gamma < 5\%$. However, effective widths of up to 15 % lead to an edge shift of nearly 300 GeV. This is the largest translation of an endpoint we have obtained so far and can be understood in terms of the underlying topology: in this inclusive scenario both partitions are affected by off-shell contributions through non-resonant parts of the gluino propagators and hence they have their share in the distribution by means of the definition of M_{T2}. To this extent it was necessary to create a special event sub-sample, which slightly differs from the one introduced in the beginning. In equation (3.13) the factorisation of the spectator gluino was exchanged with a full matrix-element calculation according to

γ [%]	$\bar{M}_{T2}^{\max}$	$\bar{s}_d$	$\bar{s}_r$
0.5	1293.7 ± 0.8	5.92 ± 0.21	0.009 ± 0.003
2.5	1315.0 ± 10.8	4.42 ± 0.54	0.029 ± 0.017
5.0	1381.0 ± 27.4	1.82 ± 1.03	0.054 ± 0.027
10.0	1526.0 ± 18.6	0.70 ± 0.20	0.072 ± 0.029
15.0	1589.5 ± 31.4	0.87 ± 0.40	0.079 ± 0.022

Table 3.6: Adapted mean values of endpoint positions (in GeV), slope differences (in 1/GeV) and slope ratios for M_{T2}.

$$pp \rightarrow (b\bar{b}\tilde{\chi}_2^0) + (q\bar{q}\tilde{\chi}_1^0) \tag{3.25}$$

since the light quarks are now promoted and also play a role in the construction of M_{T2}. The six-particle final state (with subsequent factorised decay of the second-to-lightest neutralino $\tilde{\chi}_2^0$) is necessary to be able to fully analyse all off-shell effects in this inclusive scenario. The slope parameters in Table 3.6 confirm the strength of the deviation: while the differences s_d exhibit a significant drop for rising values of γ, the ratios s_r show a minor but steady increase.

3.4 Off-shell Effects in Spin Determinations

After a possible discovery of any new physics beyond the SM, the next steps in determining underlying model characteristics are the measurements of masses and spins of novel particles. While many mass determinations rely on endpoint positions of invariant mass distributions, the nature of the underlying spin is encoded in the shape of those distributions and as such more delicate to differentiate. Hence after discussing the effects of off-shell contributions on mass determination variables, in this section we turn to spin measurements and carefully analyse the effects of a fat gluino onto several methods designed to distinguish a hypothetical SUSY signal from an equivalent one of UED. In general, spin studies compare shapes of distributions by choosing one particular type of mass spectrum which is either of UED or supersymmetric nature. Since typical UED spectra are far more compressed resulting in softer decay products and thus require for more comprehensive analyses (cf. Chapter 1 and [40, 41]), we choose to stick to hierarchical SUSY like spectra. Moreover, as we want to emphasise the difference of spin in intermediate propagators and their impact on invariant mass distributions before comparing it to contributions arising from off-shell effects, we construct a particular UED model, which inherits all masses and width parameters from our SUSY benchmark model and hence allows us to use the particularly interesting decay chain already known from the mass measurement section with the replacements $(\tilde{g}, \tilde{b}_i, \tilde{\chi}_2, \tilde{l}_R, \tilde{\chi}_2) \rightarrow (g^{(1)}, b^{(1)}, Z^{(1)}, l^{(1)}, \gamma^{(1)})$. Thus in this cascade, edges of invariant masses stay the same but shapes thereof are expected to drastically change. In contrast to the gluino, the KK-gluon will retain a small effective width of $\gamma = 0.5$ % throughout this analysis. As for the technical side, we use an adapted version of the minimal UED model [31], implemented into `WHIZARD` using a recently developed `FEYNRULES` interface [78, 79]. In the following parts, we start to analyse shape asymmetries based on exclusive invariant quark-lepton masses before turning to hadronic correlations inside a single cascade and finally investigating the impact of non-resonant contributions on inclusive angular distributions.

3.4.1 Shape Asymmetries

Many studies of spin measurements rely on the specific decay topology of the *golden chain* and make inherent use of invariant mass shapes therein as discussed in Chapter 2. Since we are interested in effects emerging from a gluino, we concentrate on the extended version introduced in equation (2.12). On the basis of the methods introduced thereafter, we analyze to what extent the spin determination methods proposed in [41] are affected by the off-shell contributions from a broad gluino. The approaches studied within this work were designed to differentiate signatures of a supersymmetric gluino from the ones emerging from a Kaluza-Klein gluon excitation in models of UED.

$A^{\pm}(m_{bl})$ At first, we investigate the *first* bottom-lepton asymmetry, recall its definition (cf. equation (2.46)):

$$A^{\pm}(m_{bl}) = \frac{d\sigma/dm_{bl^+} - d\sigma/dm_{bl^-}}{d\sigma/dm_{bl^+} + d\sigma/dm_{bl^-}} \tag{3.26}$$

where we assume, that the bottom (instead of anti-bottom) quarks are to be uniquely identified through a lepton charge tag of the b-tagging algorithm. Due to the Majorana nature of the gluino, all bottom quarks are near bottom quarks in 50 % of all decays, i.e. they are produced in the first two-body decay step. Hence, visible effects from off-shell contributions of a fat gluino propagator are expected to influence half of the invariant mass shapes. Figure 3.11 depicts both the invariant mass distributions of m_{bl^+} and m_{bl^-} as well as the bottom lepton asymmetries for each 5k and 25k events. To keep the plots digestible and at the same time condense all relevant information, we refrain from using all widths but rather restrict ourselves to the most extreme values of $\gamma = 0.5$ and 15%, given by the black (solid) and blue (dotted) lines as well as the UED sample, depicted by the red (dashed) line.

The decision to artificially increase the event number by a factor of 5 up to 25k was made to clarify wether the deviating trend of the large-width sample is merely a statistical artifact. As it turns out in Figure 3.11 (d) there is indeed a subtle effect observable in the large width SUSY sample, which is well beyond the size of fluctuations, although both of the two invariant mass distributions show no strong discrepancies with respect to the two different values of γ. Nonetheless, the minimum plateau from 300 to 400 GeV as well as the subsequent rise from 500 to 800 GeV are both reduced by up to one third in magnitude. As is evident through direct comparison with the superimposed UED sample however, it is obvious that large off-shell contributions are not endangering a possible discrimination of the fundamentally different spin scenarios.

$A_s^{\pm}(m_{bl})$ Next, we investigate the impact on the *second* bottom-lepton asymmetry. The difference to the *first* asymmetry is given by the spectrum dependent property, that the softer b-quark may coincide with the nearer b-quark. We recall its definition

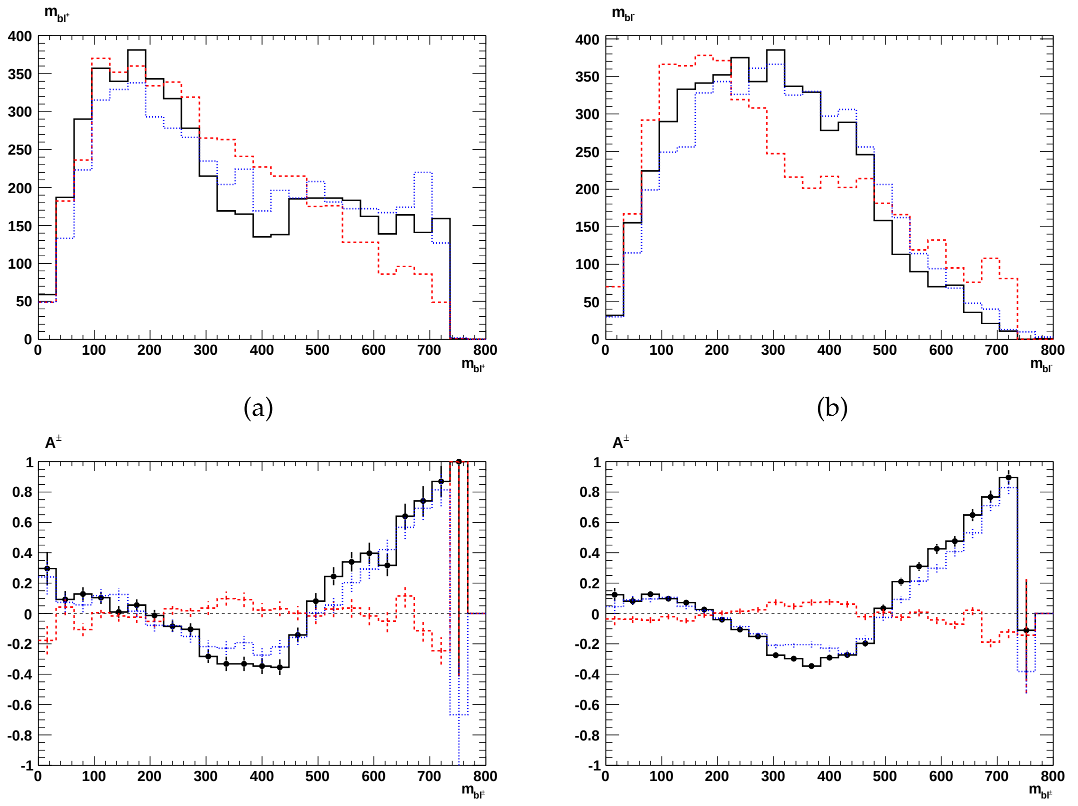

(a) (b)

(c) (d)

Figure 3.11: Invariant masses m_{bl^+} (a) and m_{bl^-} (b) with a bottom quark and their asymmetry $A^{\pm}$ for 5k (c) and 25k (d) events. See text for details of colouring.

from equation (2.47):

$$A_s^{\pm}(m_{b_s l}) = \frac{d\sigma/dm_{b_s l^+} - d\sigma/dm_{b_s l^-}}{d\sigma/dm_{b_s l^+} + d\sigma/dm_{b_s l^-}}. \tag{3.27}$$

In fact, in our scenario this is true most of the time: for small width $\gamma = 0.5\%$ in $4557/5000 \sim 90\%$ of all events the near bottom is also the softer one. Apparently, this changes when the width is increased, as is illustrated in Figure 3.1. However, even for the largest width of $\gamma = 15\%$, in $4109/5000 \sim 80\%$ of all events this assumption is correct. Obviously this characteristic will drastically change when the mass gap between the gluino and the sbottom is increased. The nearer quark will become harder due to a larger phase space in the gluino decay and the value of $A_s^{\pm}$ will consequently be reduced. In Figure 3.12 (a) and (b) we depict both invariant masses $m_{b_s l^+}$ and $m_{b_s l^-}$, which exhibit the typical smearing behaviour for large widths encountered

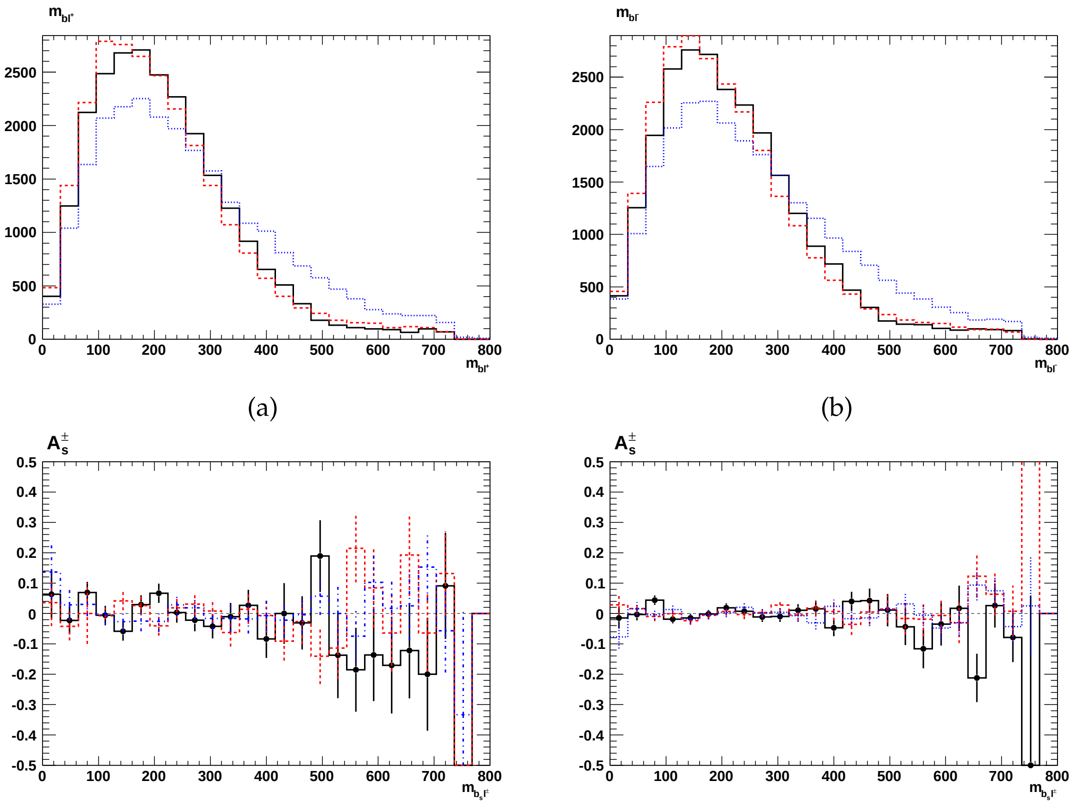

(a) (b)

(c) (d)

Figure 3.12: Invariant masses $m_{b_s l^+}$ (a) and $m_{b_s l^-}$ (b) with the softer of the two bottom quarks and their asymmetry $A_s^{\pm}$ for 5k (c) and 25k (d) events. The colouring corresponds to the one in Figure 3.11

more often in the mass measurement section above. Already by eye the asymmetries in Figure 3.12 (c) and (d) exhibit a comparable pattern: both invariant mass distributions have similar shapes and the corresponding asymmetries are thus rather small. Regardless of the size of the effective width γ, the distortion of $m_{b_s l^+}$ mimics the one of $m_{b_s l^-}$ and the same holds for the asymmetries. Consequently, the small event sample of 5k is fully compatible with a vanishing asymmetry throughout the complete range of the histogram, not only for the two SUSY samples, but also for UED. Moreover, the larger samples of 25k events also have only minor deviations from $A_s^{\pm} = 0$, which might be attributed to statistical disturbances. Altogether we find the size of this *second* bottom lepton asymmetry to be of negligible size compared to the already small deviations found in [41]. Hence, it is not surprising that a steady distortion for both $m_{b_s l^+}$ and $m_{b_s l^-}$ results in negligible change of an already very small asymmetry. We conclude that this last asymmetry is neither preferable in terms of discriminative power between SUSY and UED nor for observing differences due to off-shell effects. After all this should be attributed to the specific kind of underlying mass spectrum.

3.4.2 Hadronic Angular Correlations

Additionally it was further proposed to analyse purely hadronic correlations such as the average pseudo-rapidity $\bar{\eta}_{bb}$ or the difference of azimuthal angles $\Delta\phi_{bb}$ of the two bottom quarks [41] (cf. Chapter 2). The first of these exhibits no visible distortion with respect to the maximal width γ in the supersymmetric sample, although a small difference to the UED case is perceptible. We confirm the results of [41], where a slightly more central behaviour of the two b-quarks was found for SUSY signals. For the azimuthal distance we find a non-negligible deviation (cf. Figure 3.13) of the large width SUSY sample from the standard SUSY sample and the former turns out

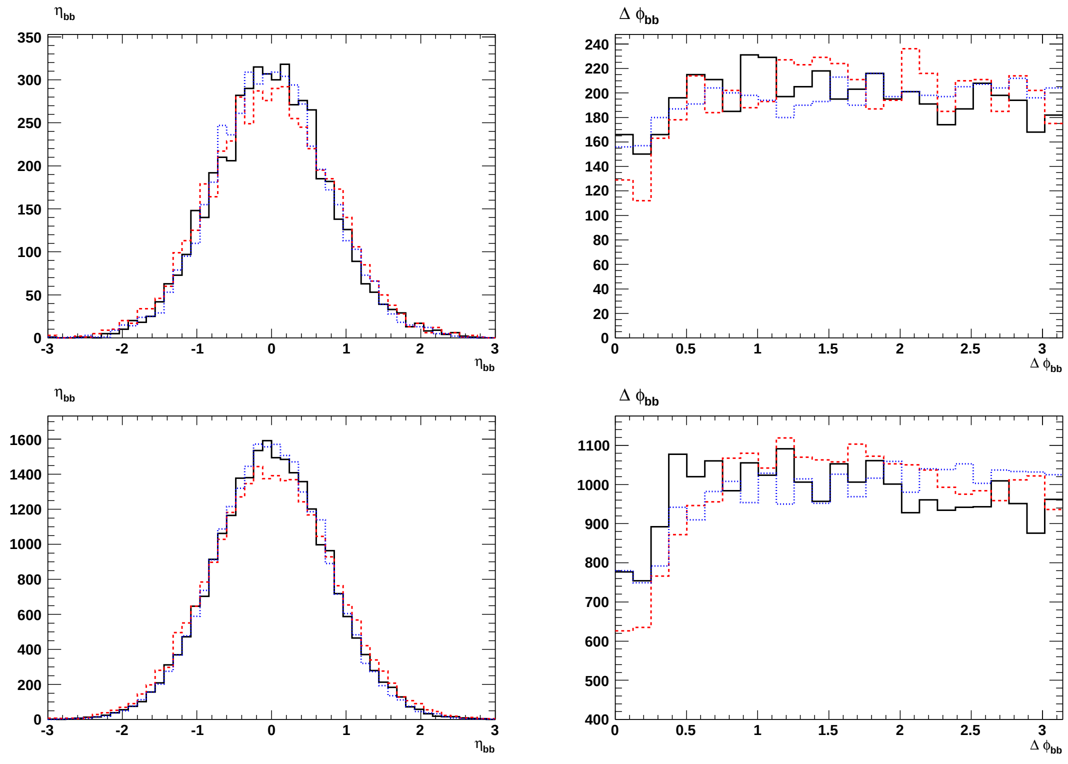

(a) (b)

Figure 3.13: Average pseudo-rapidity (a) and azimuthal distance (b) of both bottom quarks for 5k (top) and 25k (bottom) events. The colouring corresponds to the one in Figure 3.11.

to resemble the shape of UED events. As a next step, for each of the two variables the following asymmetries are defined [41]

$$A_\eta^\pm = \frac{N(|\bar{\eta}_{bb}| < 1) - N(|\bar{\eta}_{bb}| > 1)}{N(|\bar{\eta}_{bb}| < 1) + N(|\bar{\eta}_{bb}| > 1)} \tag{3.28}$$

$$A_\phi^\pm = \frac{N(\Delta\phi_{bb} < \pi/2) - N(\Delta\phi_{bb} > \pi/2)}{N(\Delta\phi_{bb} < \pi/2) + N(\Delta\phi_{bb} > \pi/2)}, \tag{3.29}$$

which were proposed to obtain an additional measure that allows for a differentiation between a standard SUSY and UED signal. We apply these variables to our three scenarios, namely the standard and off-shell SUSY as well as the UED samples. Numerical values for all of these are given in Table 3.7 for 5k and 25k events, respectively.

The value of the asymmetry $A_\eta^\pm$ of the average pseudo-rapidity $\bar{\eta}_{bb}$ only exhibits a marginal increase for the off-shell SUSY sample compared to the undistorted standard one. Both coincide within at most two sigma of the purely statistical error. The UED case on the other hand has less central values than the off-shell SUSY parts. This difference to both the standard SUSY sample as well as to the UED sample should be attributed to the fact that the off-shell contributions tend to harden (at least the first) decay product(s)[4] and hence allow for even more central values of η. The situation

sample	5k	25k
$A_\eta^\pm$ (std)	0.627 ± 0.017	0.628 ± 0.008
$A_\eta^\pm$ (ofs)	0.645 ± 0.017	0.645 ± 0.008
$A_\eta^\pm$ (ued)	0.567 ± 0.016	0.557 ± 0.007
$A_\phi^\pm$ (std)	0.014 ± 0.014	0.005 ± 0.006
$A_\phi^\pm$ (ofs)	-0.047 ± 0.014	-0.052 ± 0.006
$A_\phi^\pm$ (ued)	-0.042 ± 0.014	-0.039 ± 0.006
$A_{ct}^\pm$ (std)	0.194 ± 0.015	0.180 ± 0.007
$A_{ct}^\pm$ (ofs)	0.125 ± 0.014	0.129 ± 0.006
$A_{ct}^\pm$ (ued)	0.003 ± 0.014	0.008 ± 0.006

Table 3.7: Numerical figures for the Asymmetries $A_\phi^\pm$, $A_\eta^\pm$ and $A_{ct}^\pm$ defined in equations (3.29), (3.28) and (3.32) for different scenarios: std, ofs and ued correspond to the standard ($\gamma = 0.5\%$) and off-shell ($\gamma = 15\%$) SUSY as well as UED event samples. Errors are purely statistical.

---

[4] recall the p_T distributions of the near and far bottom quarks in Figure 3.1

looks a lot less promising for the azimuthal distance $\Delta\phi_{bb}$ of the two bottom quarks. Here we find that off-shell contributions in the large width SUSY sample drive the asymmetry $A_{\phi}^{\pm}$ such, that mistaking these effects with signals of UED is imminent. Although the shapes of the distributions differ by a moderate amount visible by eye in all three scenarios (cf. Figure 3.13 (b)), the off-shell SUSY sample is washed out in such a way so as to drive the quantitative numerical estimate of the asymmetry negative by the same amount as in the case of UED (cf. Table 3.7).

3.4.3 Inclusive Angular Distributions

Finally, we investigate angular correlations of the initially produced particles, which in our case corresponds to gluinos or KK-gluons. Although we are not able to reconstruct the complete mother particle momenta due to missing energy, the first emitted partons of each decay cascade should still possess an observable angular correlation among each other. This was first used in the variable

$$\cos\theta_{ll}^{*} = \tanh\left(\frac{\Delta\eta_{ll}}{2}\right) \tag{3.30}$$

in a study of slepton production [42] and later adapted to general coloured SUSY production [43], both introduced in the Chapter 2. The adapted method was applied to fully hadronised inclusive signal event samples with gluino and squark contributions or the corresponding equivalent for UED, where the largest discriminative power is attributed to the squark and KK-quark signatures. Our study on the other hand is based on the parton level and we restrict ourselves to subsamples with gluinos, since we aim to assess the impact of their off-shell contributions on the method. More precisely, we apply the variable to the *exclusive* gluino benchmark process in our scenario introduced in the beginning of this chapter in the following way:

$$\cos\theta_{qq}^{*} = \tanh\left(\frac{\Delta\eta_{q_l q_r}}{2}\right) \tag{3.31}$$

where $q_l = \min(b_1, b_2)$ and $q_r = \min(q_1, q_2)$ are the softer of the two quarks from each cascade side. While in [43] the largest contributions arise from prompt squark decays to quarks and lightest neutralinos and thus $\cos\theta_{qq}^{*}$ is chosen to be applied to the two hardest objects, we make particular use of the (unfortunately spectrum-dependent) approach of selecting the softer quarks to be attributed to the first (near) gluino or

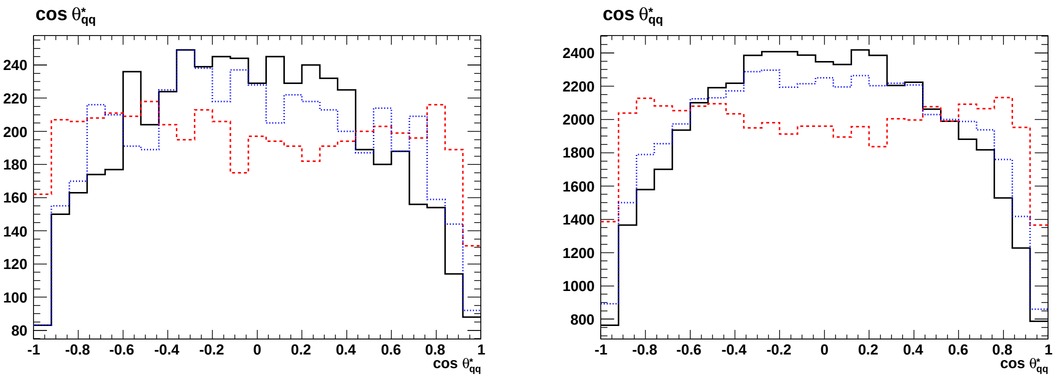

(a) (b)

Figure 3.14: $\cos\theta^*_{qq}$ for 5k (a) and 50k (b) events. The colouring corresponds to the one in Figure 3.11.

KK-gluon decay products. These are furthermore assumed to inherit features of the initially produced mother particles. Figure 3.14 illustrates the behaviour of $\cos\theta^*_{qq}$ for the two SUSY scenarios with different width (black and blue) and the UED scenario (red) for 5k and 50k events. We included the high statistics sample to show the asymptotic behaviour of the fundamentally different models. The distortion due to off-shell contributions is apparent, and although they tend to wash out the distribution to less central values, the differentiation with respect to UED is not endangered in the exclusive gluino subsample. A quantification of this statement can be obtained through the definition of the asymmetry [43]:

$$A^{\pm}_{ct} = \frac{N(|\cos\theta^*_{qq}| < 0.5) - N(|\cos\theta^*_{qq}| > 0.5)}{N(|\cos\theta^*_{qq}| < 0.5) + N(|\cos\theta^*_{qq}| > 0.5)} \tag{3.32}$$

whose values for the three cases are given in Table 3.7. The initial observations from Figure 3.14 are confirmed: while the value of $A^{\pm}_{ct}$ is indeed reduced by one third in the *standard* SUSY sample with respect to the off-shell SUSY sample, the UED case is compatible with a value of zero. Hence we conclude, that although an apparent discrepancy of $\cos\theta^*_{qq}$ is confirmed, it is not threatening the discrimination of SUSY and UED models.

Summary

In this chapter the impact of off-shell effects from a broad gluino on a representative selection of observables for mass and spin determination is analysed with a discrete set of effective width-to-mass ratios $\gamma = \Gamma/M \in \{0.5\%, 2.5\%, 5.0\%, 10.0\%, 15.0\%\}$. The basis for this analysis are SUSY signals from gluinos where production *and* the first decay step are simulated with a full matrix-element calculation to account for non-resonant contributions in the gluino propagator distorting kinematic observables. All subsequent decays are then factorised using the NWA including spin correlations. An adapted Edge-to-Bump method is employed to quantify deformations in kinematic distributions, which arise in scenarios with large effective width-to-mass ratios γ. In this approach, several parameters from a naive linear kink function fitted to the corresponding variables are extracted and utilised to highlight the blurring character of these off-shell contributions. In general, mass measurement observables are more obviously affected in that the endpoint smear dominates the distributions of otherwise sharp edge structures already at $\gamma = 5\%$ and steadily increases throughout higher values of γ. As a result, the endpoint positions obtained with the Edge-to-Bump method are drastically shifted at a very fundamental level. The difference and the ratio of the two slope parameters are additional measures of distortion which similarly indicate a washed-out endpoint behaviour. Methods of spin determination are on the other hand less affected by propagator contributions far off the mass-shell. Shape asymmetries as well as angular correlations exhibit only small deviations of event samples with broad gluinos from the ones with a *regular* narrow resonance. In the special case of azimuthal distance, the difference of these two event samples however is of considerable size, and although the shapes of the broad SUSY as well as the UED sample still differ, the numerical values of the associated asymmetry $A_{\phi}^{\pm}$ coincide within their purely statistical errors. Our findings suggest that scenarios with broad resonances as in our exemplary case a fat gluino lead to severe distortions of kinematic distributions which are the basis for many mass and spin determination methods. These deviations from non-resonant contributions arise at the fundamental parton level in simulations where production and decay are simulated with the full matrix element. Many existing studies on the other hand utilise the NWA, whose predictions vigorously differ from the full calculation. Hence a correct treatment of such effects is of crucial importance for both mass and spin measurements so as to not misinterpret the potential signals of much sought-after new physics.

Chapter 4

Combinatorial Effects in Gluino Dijet Endpoint Measurements

In this chapter we attempt to measure the dijet mass edges from two different gluino decay modes in a realistic LHC environment for three different benchmark scenarios based on [80]. We study the emerging combinatorial and SUSY backgrounds and assess their impact on the measurements through several new and existent variables. Finally we quantify the different endpoint positions with an adapted edge-to-bump method introduced in Section 2.1.3.

4.1 Introduction

Measuring masses of supersymmetric particles is a highly non-trivial task that requires a good understanding of the detector as well as the underlying physics performance, not least since in R-parity conserving models we expect to observe huge amounts of missing energy. The recent discovery of a new particle, supposedly the Higgs boson, with a mass of around 125 GeV favours supersymmetric scenarios with heavy scalars [6, 7, 81]. In these models, the lightest coloured particle is often the gluino. If its mass is within reach of a 14 TeV LHC, i.e. at most a couple of TeV, we are likely to measure a signal with many jets originating from subsequent three-body decays of the colour octet fermion. Other than the edge positions of a gluino two-body decay discussed and described in Chapters 2 and 3, these endpoints of three-body decays are simply given by the mass difference of the involved particles. The prompt gluino decay into two jets and the LSP may hence constitute an additional indirect approach to measure the mass of a hypothetical dark matter candidate.

Many existing methods of mass measurements introduced in Chapter 2 rely on the particular knowledge of the mass hierarchy, the precise decay chain or the complete underlying SUSY model in question. Naturally this information is neither a priori available nor is it likely to have just one particular dominant decay pattern.

Another issue is the generally inclusive nature of the production of supersymmetric particles: if squarks are kinematically accessible at the LHC, the associated production of gluinos and squarks is known to dominate the production rates over a wide range of parameter space. Hence it is difficult to separate pure gluino from pure squark signatures. These irreducible contributions are traditionally referred to as *SUSY backgrounds*.

Moreover, SUSY processes with additional jet radiation are of the same size as the leading order processes themselves (depending on the phase space region, see e.g. [82]) and the presence of those initial state radiation (ISR) jets in the event considerably influences the results of mass reconstruction [60, 83].

What is more, some of the variables need particular assignments to a specific decay cascade (e.g. the single-sided versions) or simply a partition into two different sides (e.g. grouping of visible momenta for application of M_{T2}). However, partitioning of the visible momenta is also spectrum dependent and far from straightforward. False assignments of momenta to decay sides pose another severe threat to mass measurment methods and should be handled with care. They are known as *combinatorial backgrounds*. Note, that in principle a high-p_T ISR jet as well as jets from irreducible *SUSY backgrounds* (e.g. a squark decay) both contribute to the *combinatorial backgrounds*. As an example consider the process $\tilde{g}\tilde{g} \to 4j + 2\tilde{\chi}_1^0$, where the probability of the correct jet pairing is 1/3. However, a process such as $\tilde{q}\tilde{g} + j_{\text{ISR}} \to 4j + \tilde{\chi}_1^0\tilde{\chi}_i \to 6j + 2\tilde{\chi}_1^0$ with two jets not meeting the selection criteria resulting in the same 4j + $\not{E}_T$ final state has a correct jet pairing probability of either 1/6 (gluino jet kept) or 0 (gluino jet dismissed).

In principle, there is no solution to the first obstacle. The other drawbacks have in parts been addressed in the literature. *SUSY backgrounds* for example are assumed to be under approximate control through crude selection criteria. The sheer number of jets, although affected by the presence of ISR and the like, may be taken as a rough guideline for the underlying physical process: at least two, three or four hard objects in principle correspond to squark pair-, gluino-squark associated- and gluino pair-production, respectively. However, this represents only an approximate estimate and in the following we will discuss the influence of such a selection in more detail. Several ideas have been proposed [84, 53, 54, 55] to address the issues of *combinatorial backgrounds*, some of which make inherent use of the kinematical dijet edge position of the gluino in event topologies of the type: $\tilde{g}\tilde{g} \to 4j + \not{E}_T$. These methods assume that this gluino endpoint is known and further make use of it in discriminating wrong particle assignments by imposing an upper invariant mass threshold for two possible jet combinations at precisely *this* edge. Despite the fact that these approaches give good results in discarding false assignments with reasonable efficencies and high purity, they all neglect the fundamentally important circumstance that both the identifaction as well as the position of the exact gluino dijet endpoint itself suffers from *SUSY and combinarotial backgrounds*.

The road of this chapter is to assess the feasibility of such a gluino dijet endpoint measurement in a realistic LHC environment including both *SUSY* and *combinatorial backgrounds* as well as disturbing effects of ISR and detector smearing. However, in an inclusive SUSY sample it is most likely to have not only one but several of these gluino dijet endpoints which is why we consider two potential options: a gluino decay into two jets accompanied by either a bino or wino, the corresponding edges of which we denote by 'bino edge' and 'wino edge', respectively. Gluinos and left-handed squarks in general decay more often into wino states, whereas these further decay into final states with jets or leptons and a bino. These wino jets are an additional source of jet background and lead to further complications of combinatorics. Both the wino edge as well as the bino edge are three-body decay endpoints and as such are given by the mere mass difference of mother and daughter particles. If we now safely assume the involved quarks to be massless, the edge positions are given by the difference of gluino and bino or wino mass. Since the latter is usually heavier than the former, the wino edge is located below the bino edge. Contrasting this with the supremacy of wino decay modes in terms of quantity, we establish an inconvenient truth: on one hand the sheer amount of events contributing to the wino edge drastically weakens the structure of the bino edge in an inclusive SUSY sample. The latter in turn overshoots the former, which has the undesired ramification of mimicking impeding effects of hadronisation and detector resolution, even so if combinatorial issues are artificially set aside by means of MC truth information. So in the following we attempt to disentangle those two edges using a method of semi-inclusive jet multiplicity selection: we propose two event selection criteria covering particular ranges of jet multiplicities and leptons.

In the next sections we introduce three benchmark scenarios within a semi-simplified model, differing with respect to their relative mass hierarchies, along with our simulation setup before discussing all possible event topologies culminating in the definition of two particular selection criteria responsible for the edge discrimination. We then illustrate a set of existing and new variables which we further use in the next sections together with the criteria to disentangle and estimate the particular endpoint positions in detail.

4.2 Benchmark Scenarios and Simulation Setup

To keep this analysis as generic as possible and at the same time cover a wide range of parameter space we make use of a semi-simplified model with a lot less parameters than the MSSM. This still covers the gross features of interest from general SUSY scenarios within models of gravity or gauge mediation. Two characteristics of our model are decoupled sleptons and third generation squarks. Our study concentrates on the impact of multi-jet combinatorics and additional leptons from slepton decays or b-tagged jets from third generations squarks may in any case help unravel the underlying SUSY cascade and scenario. All higgsinos are decoupled as well, hence we obtain a lightest neutralino which is purely bino and a second-to-lightest neutralino (or lighter chargino) that is purely wino. We furthermore impose an approximate GUT relation 6:2:1 on the gaugino masses and fix them to the values $(m_{\tilde{g}}, m_{\tilde{W}}, m_{\tilde{B}})$ = (1200,400,200) GeV. Moreover, we concentrate on scenarios where the gluino is lighter than all squarks. The motivation for this has in parts been outlined above and is in short given by a moderately heavy Higgs mass of 125 GeV, which itself is possibly driven by heavy third generation squarks. Nonetheless, a rough estimate of the gluino and squark mass splitting is likely to be obtained by distributions of the hemisphere mass or the inclusive M_{T2} version in high p_T dijet events [83]. Hence in our model the gluino features three body decays to dijet final states with bino and wino states:

$$\tilde{g} \to jj\tilde{W} \qquad \text{or} \qquad \tilde{g} \to jj\tilde{B}. \tag{4.1}$$

spectrum	$m_{\tilde{Q}}$	$m_{\tilde{G}}$	$m_{\tilde{W}}$	$m_{\tilde{B}}$	$m_{jj}^{max}(\tilde{W})$	$m_{jj}^{max}(\tilde{B})$
A	1300	1200	400	200	800	1000
B	1900	1200	400	200	800	1000
C	10000	1200	400	200	800	1000

Table 4.1: Sparticle masses and endpoints of the three benchmark scenarios A, B and C (in GeV). The other scalar and higgsinos masses are set to 10 TeV.

Thus the bino edge and wino edge positions are also fixed to

$$m_{jj}^{\max}(\tilde{W}) = m_{\tilde{g}} - m_{\tilde{W}} = 800\ \text{GeV} \tag{4.2}$$

$$m_{jj}^{\max}(\tilde{B}) = m_{\tilde{g}} - m_{\tilde{B}} = 1000\ \text{GeV}. \tag{4.3}$$

Further assuming the first two squark generations to be degenerate we introduce the following scenarios based on three different values for these (also cf. Table 4.1):

Scenario A ($m_{\tilde{q}}$ = 1300 GeV)

In the first scenario, relatively light squarks (compared to the other spectra) result in a dominance of the associated $\tilde{q}\tilde{g}$ production process. The mass difference $\Delta m \equiv m_{\tilde{q}} - m_{\tilde{g}} = 100$ GeV is rather small and the branching fraction $\tilde{q} \rightarrow j\tilde{g}$ is kinematically suppressed. Squarks predominantly decay into light gauginos which in turn leads to a hard jet and only one signal gluino for the overall dominant production and decay process.

Scenario B ($m_{\tilde{q}}$ = 1900 GeV)

The second scenario is motivated by moderately heavy squarks and a reduced but still sizable associated $\tilde{q}\tilde{g}$ production. As a consequence of the larger mass difference $\Delta m \equiv m_{\tilde{q}} - m_{\tilde{g}} = 700$ GeV, the squark decays to a gluino and hence we expect a moderately hard jet together with two signal gluinos in the dominant combined production and decay process.

Scenario C ($m_{\tilde{q}}$ = 10000 GeV)

In the third scenario, the squark mass is set out of LHC reach. Gluino pair production is the only SUSY QCD process. Hence in some sense this spectrum represents a best case scenario for a pure gluino study.

In the analysis below all event samples were obtained with `Herwig++` [85] and `WHIZARD` [74]. Moreover these samples are inclusive in that they embrace the full simulation chain from parton level, showering, hadronisation and decay to detector response. The latter was simulated with `DELPHES` [86] set to CMS detector settings with the anti-k_T algorithm and a jet resolution parameter R = 0.5. Further jet criteria are a minimum transverse momentum of $p_T^{\text{min}} = 50$ GeV and a restriction to the more central areas in the detector with $|\eta| < 2.5$. Those are designed to suppress soft activities from inital and final state radiation as well as the underyling event. Additionally we adopted the SUSY baseline selection from [87] designed to reduce SM backgrounds:

- $H_T > 800\,\text{GeV}$
- $E_T^{\text{miss}} > 200\,\text{GeV}$
- $\Delta\phi(j_{1/2}, E_T^{\text{miss}}) > 0.5$

Here H_T is defined as the scalar sum of (just) the first four hardest jets j_i ($i \in \{1, 2, 3, 4\}$). Specifically the cut on the angle between the missing energy $\not{E}_T$ and the first two hardest jets is designed to reject events, where the missing energy results from jet energy mismeasurements.

4.3 Derivation of Selection Criteria

We now develop two basic selection criteria which allow for a discrimination between different edges that originate from two main gluino decay modes. In many studies an exclusive gluino decay into two jets and LSP ($\tilde{g} \to jj\tilde{B}$) is a crucial and mostly generic assumption. The gross number of SUSY spectra suggested by most SUSY breaking scenarios however exhibit richer gluino decay patterns with at least two comparable decay modes into bino ($\tilde{g} \to jj\tilde{B}$) *and* wino ($\tilde{g} \to jj\tilde{W}$). Recall from equations (4.2) and (4.3), that each of the two modes has a different endpoint position. A larger gauge coupling of the wino furthermore leads to a domination of the wino edge, although its position is located below the bino edge. The latter in turn weakens the structure of the former, despite the smaller amount of events. Taking into account the successive decay of the weak gaugino (wino), the situation becomes even more involved with respect to combinatorics. In our benchmark scenarios, the (relevant) decays of both the neutral and charged components (i.e. the second-to-lightest neutralino and the lighter chargino) are given by

$$\tilde{W}^0 \to h + \tilde{B} \to bb\tilde{B} \tag{4.4}$$

$$\tilde{W}^\pm \to W^\pm + \tilde{B} \to jj/l\nu + \tilde{B}. \tag{4.5}$$

Since we refrain from additional information from b-tagging and furthermore treat all b-jets as non-tagged generic ones, the overall number of jets drastically increases for all variants of the included wino decay modes of the gluino. An increased number of jets results in an even larger number of possible jet pairings and hence a radically reduced probability of picking the correct combination. Even though the introduction of an additional decay mode constitutes a further complication of combinatorial nature, we will shortly see how to make use of this for the discrimination of those two endpoints.

In order to distinguish between the bino and the wino edge we propose to divide the inclusive event sample consisting of all production and decay modes into two subsamples. Each of these is designed to maximise the number of events with one particular decay mode (e.g. bino) and minimise the contamination of events with the respective other decay mode (e.g. wino). One indication for a possibly dividing measure is the number of decay products or final state jets, respectively. In Figure 4.1 the classification of event topology patterns for the dominant gluino production mechanisms as well as the successive decays is depicted. The values in the left column represent the numbers of decay products of *both* SUSY decay cascades. As can be seen from the first row of Figure 4.1, topologies with four or less SUSY decay products correspond to events with exclusive bino decay modes. Topologies with eight or more SUSY decay products on the other hand are unambiguously originating from events with exclusive wino decay modes.

In a crowded hadron collider environment, the number of decay products is naturally not available. Polluting aspects of initial and final state radiation, hadronisation, further decays as well as the underlying event all considerably contribute as possible sources of jets and smearing. Detector responses and clustering effects of the jet algorithm furthermore distort the correspondence between the number of SUSY decay products and the inclusive number of jets in the event. Although the aforementioned issues are of substantial size and influence, this correlation persists to a great extent

# decay particles	topology
3/4	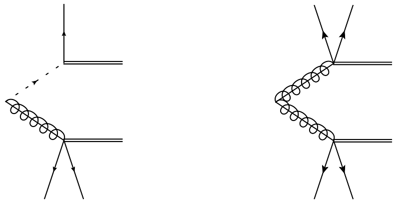
5	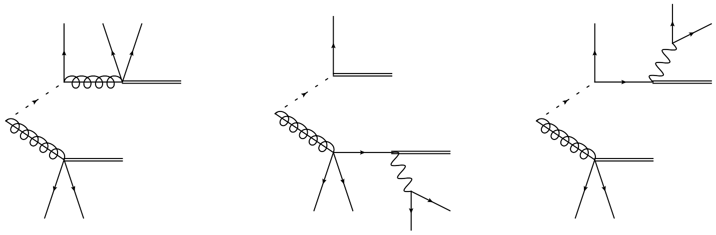
6	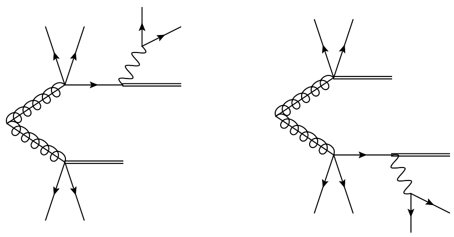
7	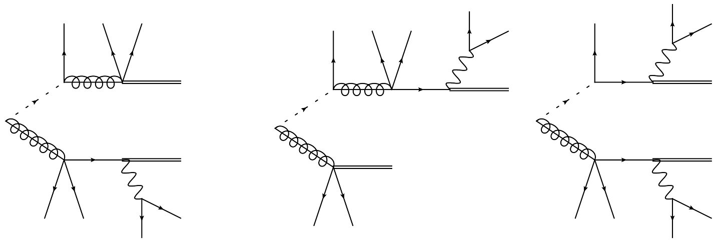
8/9	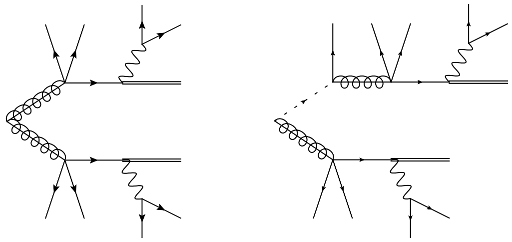

Figure 4.1: Classifcation of event topology patterns for the dominant gluino production mechanisms with successive decays according to the number of decay products. Double lines visualise the stable but invisible bino which is the LSP.

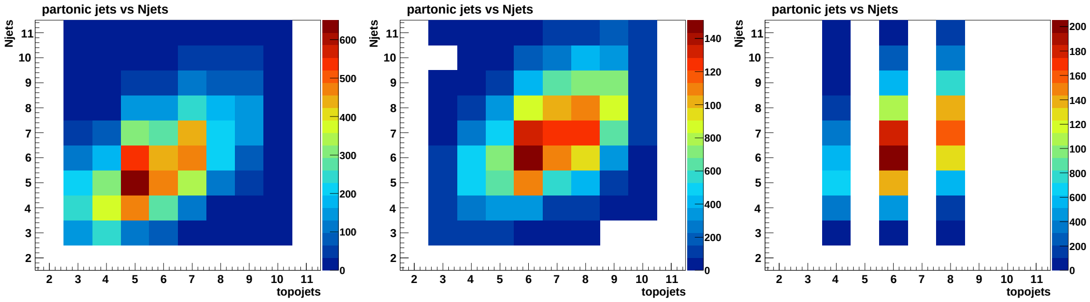

Figure 4.2: Inclusive number of detector level jets vs expected number of (coloured) SUSY decay products from topological considerations. Scenarios A, B and C are shown in the left, center and right plots, respectively.

throughout all three scenarios as is visible from Figure 4.2. Even the strict minimum baseline cuts of $p_T > 50$ GeV and $|\eta| < 2.5$ do not alter this result by much. To distinguish the different decay modes, we propose the following selection criteria for the division of the event sample into two subsamples with maximised relative bino or wino content:

- **bino edge:** 4-5 jets & lepton veto,
- **wino edge:** ≥ 6 jets & 1 lepton.

Those two criteria *define* our semi-inclusive jet multiplicity selection method. For the first (bino) selection we decide to stick to 4 or 5 jets and a lepton veto which discards events with a leptonically decaying wino. By lepton we either denote an electron or a muon with $p_T^{\text{min}} > 20$ GeV and $|\eta| < 2.5$. The enlargement of the subsample by one supplemental jet (with respect to the four expected decay products) has several reasons. First of all, we expect to have large contributions from hard initial state radiation that accounts for one additional jet. What is more, the statistical significance of an exclusive four jet sample can be very low. An increase of up to five jets is rewarded with a gain in (signal) statistics at the price of a slightly larger contamination of winos in the sample. On the other hand this contamination is to some extent acceptable, since the wino endpoint is located below the bino endpoint. Finally, the SM background is known to be very large in low multiplicity jet bins. Although a detailed systematic analysis of the SM backgrounds is beyond the scope of this study, the benefits of an additional jet requirement with respect to background suppression can be shown to be huge [88].

Turning to the wino selection criteria, we as well modify the expected initial criterion of eight or more SUSY decay products: instead of selecting ≥ 8 jets, we require ≥ 6 jets and at least one additional lepton. A leptonically decaying wino allows for a reduction of the number of jets down to six which drastically reduces the possible number of (wrong) jet pairings. Already very few events with bino decay modes may spoil the clear endpoint structure of the wino edge due to the higher edge position and hence, the lepton requirement further improves the ratio of wino to bino events at the price of decreased statistics. The dominance of wino events is reflected in the relative ratios of decay modes for the two selection criteria: while for the bino selection the ratio $N(\tilde{B})/N(\tilde{W})$ is in the ballpark of 0.3 - 0.7, dependent upon which of the three spectra is analysed, the wino selection allows for a much better ratio of $N(\tilde{W})/N(\tilde{B}) \sim \mathcal{O}(10)$.

With the two selection criteria defined above we are now able to discuss the relevant SM background contributions in addition to the signal. As for the bino selection, two processes dominate as possible backgrounds: overwhelmingly large QCD multijet background, where the missing energy $\not{E}_T$ originates from neutrinos of heavy flavour quark decays or jet energy mismeasurements from instrumental effects, and furthermore Z + jets, where the heavy gauge boson decays into two neutrinos. Other common backgrounds such as leptonically decaying $t\bar{t}$-pairs or W + jets are expected to be suppressed by the lepton veto. A further reduction of backgrounds may be achieved by cutting on more advanced variables such as $Y_{\text{MET}} = \not{E}_T/\sqrt{H_T}$ which is used for SUSY searches at ATLAS and CMS [89, 90].

The wino selection on the other hand is anticipated to have very little to no backgrounds at all, since the endpoint selection criteria themselves are sufficiently suppressing all SM contributions to the extent that no additional cuts are needed to extract the desired endpoint information. Neither QCD - due to the lepton requirement - nor W/Z + jets - due to the high jet multiplicity - are expected to have an influence on the measurement [88].

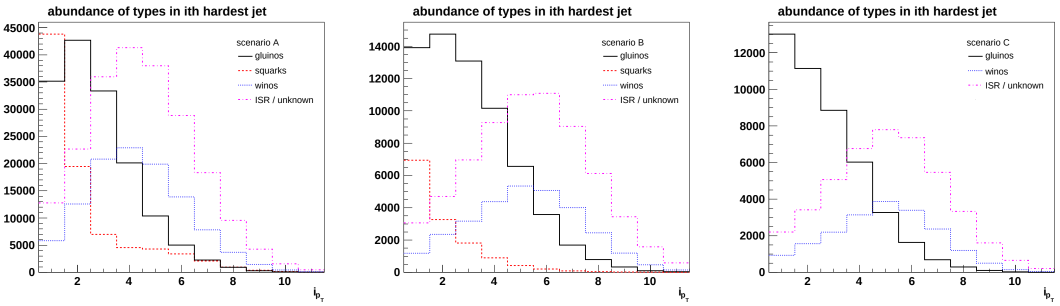

Figure 4.3: Gluino (black full line), squark (red dashed line), wino (blue full line) and ISR/unknown (blue dotted line) jet abundances in the inclusive sample for bin of jet hardness *i* in spectra of type A, B and C in the left, center and right plot, respectively.

4.4 Kinematic Variables with reduced Combinatorial Impact

In the next steps we address the combinatorial issues mentioned earlier throughout this chapter. More precisely, we will discuss a set of existent variables and propose new ones which allow for an extraction of relevant endpoints in the two subsamples defined by the selection criteria introduced in the previous section. In our semi-inclusive jet samples there are at least four to six jets, two of which have to be combined to an invariant mass. Furthermore, there are at most two signal gluinos whose decays result in up to four *true* gluino jets. On the other hand, there exist several other origins for jets, such as ISR and W decays. In scenarios with light squarks (such as scenario A and to some extent scenario B), additional jets may also arise from prompt squark decays. Albeit the transverse momenta of three-body decay jets from gluinos is known not to be too large, a difference to ISR and wino decay jets is expected to be observable. A distinction to the squark decay jet may or may not be feasible and is heavily dependent upon the spectrum. This conjecture is reinforced by the distributions in Figure 4.3, where the abundance of jets from different origins is plotted against their hardness. These jets are identified using MC truth information in that detector level objects are matched to partonic decay particles. If such an assignment to the corresponding SUSY mother particle is not successful, it is either due to clustering effects of the jet algorithm or initial state radiation before the hard process. One point to take away from Figure 4.3 is the relatively high abundance of jets with gluino origin in the first three highest p_T objects. The influence of the squark in the first two scenarios A and B however is not negligible: a significant contribution in the highest p_T bin from the decay $\tilde{q} \rightarrow j\tilde{B}(\tilde{W})$ enhances the probability of wrong jet pairings. Due to the nature of the highest p_T object, a pairing of such a jet supposedly originating from a squark decay and a *correct* gluino jet is likely to exceed the true endpoint and thus spoil the anticipated edge behaviour. Hence we propose a minimization procedure inherent in the definition of two novel variables

$$min_{3j} = \min_{k=1,2}\{m_{3k}\} \tag{4.6}$$

$$min_{123} = \min_{i,j=1,2,3}\{m_{ij}\}, \qquad i \neq j \tag{4.7}$$

which reduces the impact of excess events beyond the true endpoint from falsely combined highest p_T objects. Here m_{ij} denotes the invariant mass of jets i and j. While min_{3j} fixed the third hardest jet and minimizes over the two highest, min_{123} is even smaller since the minimization procedure includes one additional combination: m_{12}. The endpoint of min_{123} is smaller or equal to the true gluino endpoint as long as two gluino jets from the *same* decay chain are among the three highest p_T jets. Thus in scenarios with predominantly one signal gluino such as type A we anticipate good results from both min_{j3} and min_{123} albeit the moderately low relative gluino jet abundance (cf. Figure 4.3).

For scenarios of type B we find the highest relativ gluino jet abundance in the jet bins with hardness $i = 2, 3, 4$, motivating the introduction of the following variable

$$min_{234} = \min_{i,j=2,3,4}\{m_{ij}\}, \qquad i \neq j \tag{4.8}$$

where by construction we explicitly exclude the highest p_T jet before taking the minimum out of all other invariant dijet mass combinations among the four hardest jets. Again we anticipate the endpoint of min_{234} to stay below the true endpoint as long as two gluino jets from the same cascade are among the set over which we minimize.

The combinatorial problem of gluino dijet edge extraction has been partially discussed in the literature. One such approach is indirectly given by a naive application of the hemisphere method [59] introduced in Chapter 2. Recall the basics of the algorithm: after the division of an event into two hemispheres defined by two seeds (the object with the highest p_T and the one maximizing $\Delta R \cdot p$), each element is assigned to one of the two spatial areas using the Lund distance measure defined in equation (2.32). When this clustering is finished, the seeds are updated and the procedure is iteratively applied until the assignment converges. After two well defined hemispheres with separated objects are found, the next step is the naive combination of the two highest p_T jets from each hemisphere to form an invariant mass. This defines the following two variables:

$$m_{12}^{(1)} = m_{12} \ \text{(from hemisphere 1)}, \quad m_{12}^{(2)} = m_{12} \ \text{(from hemisphere 2)}, \tag{4.9}$$

with hemisphere 1 being associated to the first seed, i.e. the one with the highest p_T jet.

Another method to obtain gluino dijet endpoints is merely given as a by-product of a set of variables introduced to investigate event topologies of exclusive 4j + $\not{E}_T$ final states [91]. Two out of the four variables are dijet mass variables which we will use for our purpose. The first, F_3, was specially designed to investigate, whether 3 out of 4 jets originate from a *single* decay chain, ergo the underlying topology is of the type $3 \oplus 1$. It is defined as the invariant dijet mass *opposite* to the maximum of all possible combinations:

$$F_3(p_1, p_2, p_3, p_4) = m_{kl}, \qquad \text{for} \quad \epsilon_{ijkl} \neq 0 \quad \text{and} \quad m_{ij} = \max_{r,s=1,\ldots,4} \{m_{rs}\}. \tag{4.10}$$

By construction for an asymmetric $3 \oplus 1$ topology the endpoint of F_3 coincides with the largest one of the 3 particle cascade. The other dijet variable, F_4, is designed to bring forth the symmetric $2 \oplus 2$ topology where two jets are produced on both sides. Its definition is given as the minimum of the larger invariant dijet mass out of three possible pairings:

$$F_4(p_1, p_2, p_3, p_4) = \min_{i,j=1,\ldots,4} \{\max\left(m_{ij}, m_{kl}\right)\}, \qquad \epsilon_{ijkl} \neq 0. \tag{4.11}$$

The endpoint of F_4 is smaller or equal to the true gluino endpoint if the symmetric topology under investigation is e.g. a pure gluino pair production signal with subsequent bino decay modes. Disturbing effects of ISR, hadronisation and detector acceptance are however known to decrease the performance of those variables to a great extent [91]. In the upcoming analysis we use both of these variables not only for 4 jets + $\not{E}_T$ events but also apply them to our two selection samples for bino and wino in that we make use of just the four hardest jets and compare them to our variables defined above.

4.5 Discriminating distinct Gluino Endpoints

In the following we apply the variables we just introduced to the two event samples that correspond to the two selection criteria for bino and wino edges. The simulations are based on a 14 TeV LHC with an assumed integrated overall luminosity of 300 fb^{-1}. In scenarios A, B and C this amounts to 108.000, 27.600 and 16.200 signal events, respectively. Furthermore the generated events are fully inclusive in that the whole simulation chain of parton showering, hadronisation, decays and detector response is in place. These figures were obtained by the most recent version of `Herwig++` and cross-checked with `WHIZARD`. These numbers are conservative since they correspond to leading order cross-sections and NLO QCD corrections typically only enlarge them by K-factors of up to two [72].

4.5.1 Scenario A

The first of the three scenarios is determined by the small squark gluino mass difference of just 100 GeV. An immediate consequence is the dominance of squark gluino association production which leads to only one signal gluino when combined with a preferred squark decay into light gauginos. Moreover, the jet with the highest p_T in the event is more likely to originate from a squark than from a gluino decay (cf. Figure 4.3) and should thus be excluded from explicit usage.

In Figure 4.4 the distributions of all variables for scenario A are depicted, applied to both bino (left column) and wino (right column) event selections. The first row shows the two hemisphere variables $m_{12}^{(1)}$ and $m_{12}^{(2)}$ defined in equation (4.9) in which the black solid line denotes the first hemisphere ($m_{12}^{(1)}$) and the red dashed line corresponds to the second hemisphere group ($m_{12}^{(2)}$). In the second row we display the two topological variables F_4 with a black solid line and F_3 with a red dashed one. The bottom row exhibits our new variables where the black solid, red dashed and blue dotted lines correspond to min_{123}, min_{3j} and min_{234}, respectively.

As for the bino selection we perceive that both F_3 and F_4 fail to show a clear endpoint structure around the true value of 1000 GeV. Turning to min_{123} and min_{3j} we note an endpoint structure close to the true value which however has a slight tendency to overshoot the correct endpoint. The best results are found for the two hemisphere variables, especially $m_{12}^{(2)}$ looks promising. Recalling the asymmetric nature

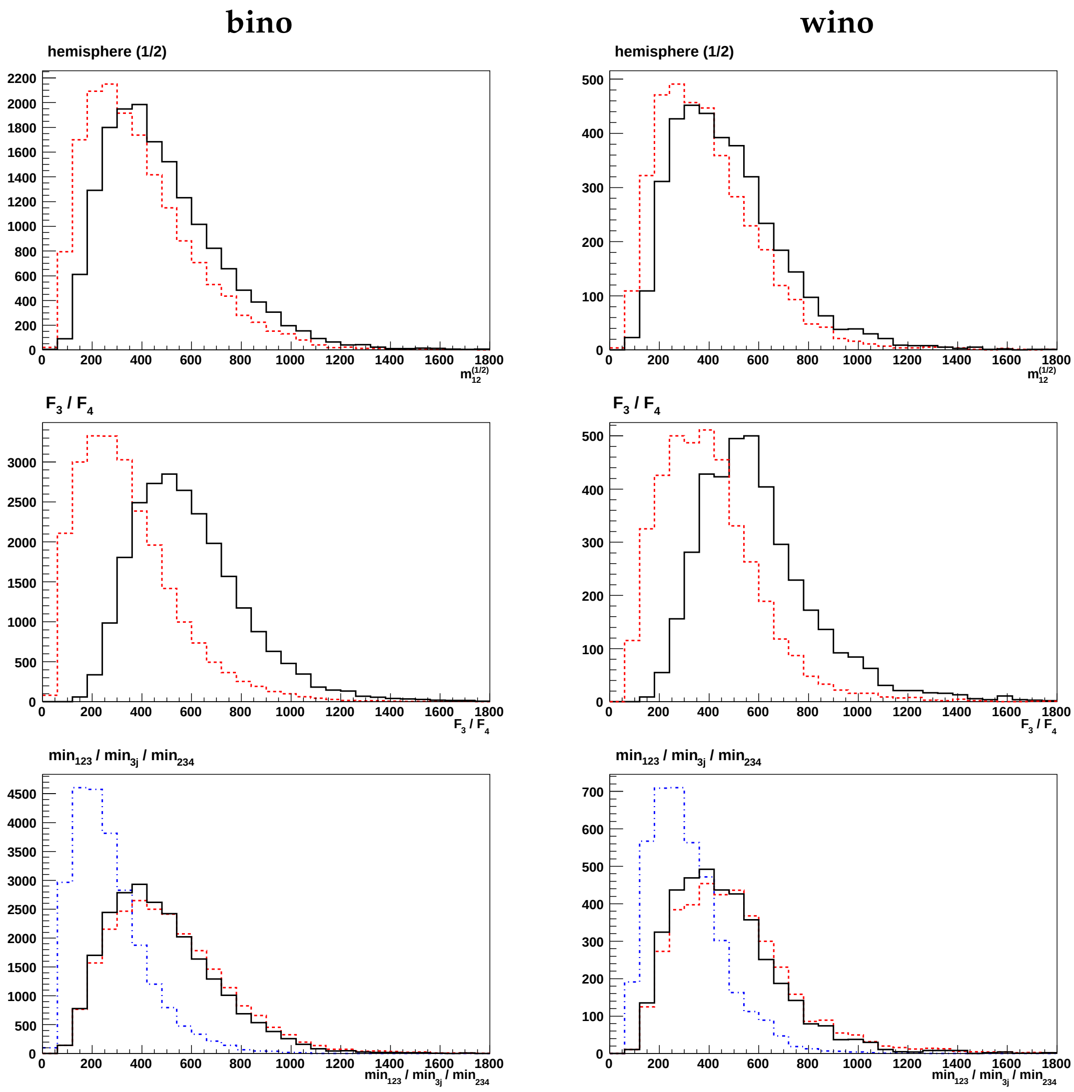

Figure 4.4: Scenario A: In the first row, the hemisphere variables for the harder $m_{12}^{(1)}$ (solid, black) and softer $m_{12}^{(2)}$ (dashed,red) hemispheres are shown. The second row features $F4$ (solid, black) and $F3$ (dashed,red). In the bottom row the new variables min_{123} (solid, black), min_{3j} (dashed,red) and min_{234} (dot-dashed, blue) are given. Bino and wino selections are depicted in the left and right column, respectively.

of scenario A we deduce that the softer of the two hemisphere variables is indeed the one we expect to work best: the harder hemisphere is very likely to be assigned to the squark decay jet, which has the highest probability of being the hardest object in the event. The opposite hemisphere grouping may hence be seen as the one corresponding to the gluino decay products.

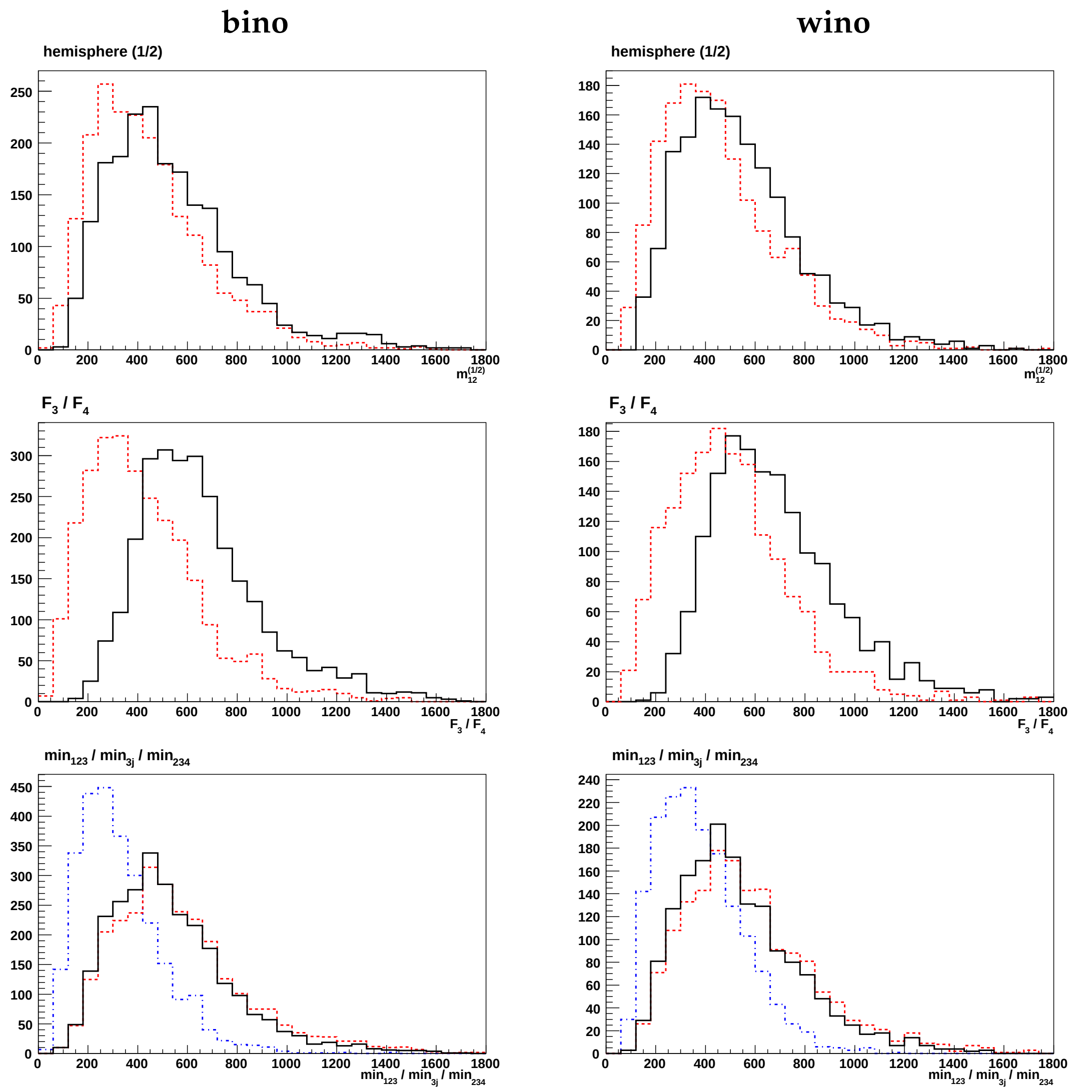

Figure 4.5: Scenario B: distributions of all variables under investigation. The histogram labeling is the same as in Figure 4.4.

Most variables in the wino selections exhibit tails beyond the true endpoint value of 800 GeV. For the minimized variables min_{123} and min_{3j} as well as for F_4, these tails are rather long. F_3 and the softer hemisphere version $m_{12}^{(2)}$ on the other hand expose a nice kink structure at the vicinity of the true edge despite the existence of a non-negligible tail. This success may again be attributed to the underlying asymmetric nature of the signals in this scenario.

4.5.2 Scenario B

In scenario B the squarks are moderately heavier than the gluino. While the squark-gluino associated production is not as dominant as in spectra of type A, it has still a sizable share in the overall production mechanisms. Another big difference to scenario A is given by the squark decay, provided that it has been produced. Due to the larger mass difference, it now predominantly decays into a jet and a gluino, increasing the overall number of gluino (signal) as well as unwanted jets. Hence the still high probability of having a (wrong) squark jet in the hardest jet (cf. Figure 4.3).

In Figure 4.5 the distributions of all variables in scenario B are plotted. The first overall impression is that many variables are shifted to higher mass regions and clear endpoint structures are mostly missing. In the bino selection we observe a shallow but existent kink structure for min_{123} and min_{3j}. F_3 also has an endpoint behaviour around 1000 GeV but the distribution itself is rather smeared. F_4 on the other hand seems to possess a kinky feature which however is washed out to great extent. The harder of the two hemisphere variables shows a more pronounced kink structure at the vicinity of the true endpoint.

The situation looks worse for the wino endpoint selection: nearly all variables consistently overshoot the true endpoint of 800 GeV and exhibit a behaviour comparable to the one of the bino selection. This would amount in gross overestimation of the endpoints if it were not for three exceptions: F_3, $m_{12}^{(2)}$ and min_{234} all make a stand against the general tendency of overshooting and feature pronounced kink structures around the true endpoint. Especially min_{234} justifies its earlier introduction with its outstanding performance at this point.

4.5.3 Scenario C

In some sense the last spectrum resembles a best case scenario. Completely decoupled squarks with masses of 10 TeV are set ouf LHC reach and do therefore not contribute to the combinatorial background. Moreover the gluino pair production is the only (relevant) SUSY QCD production process. Since many studies of combinatorial issues rely on this particular spectrum (with the caveat that only one particular gluino decay mode is investigated), we expect a generally good overall behaviour of all proposed variables. Figure 4.6 confirms this assumption. In the bino selection we

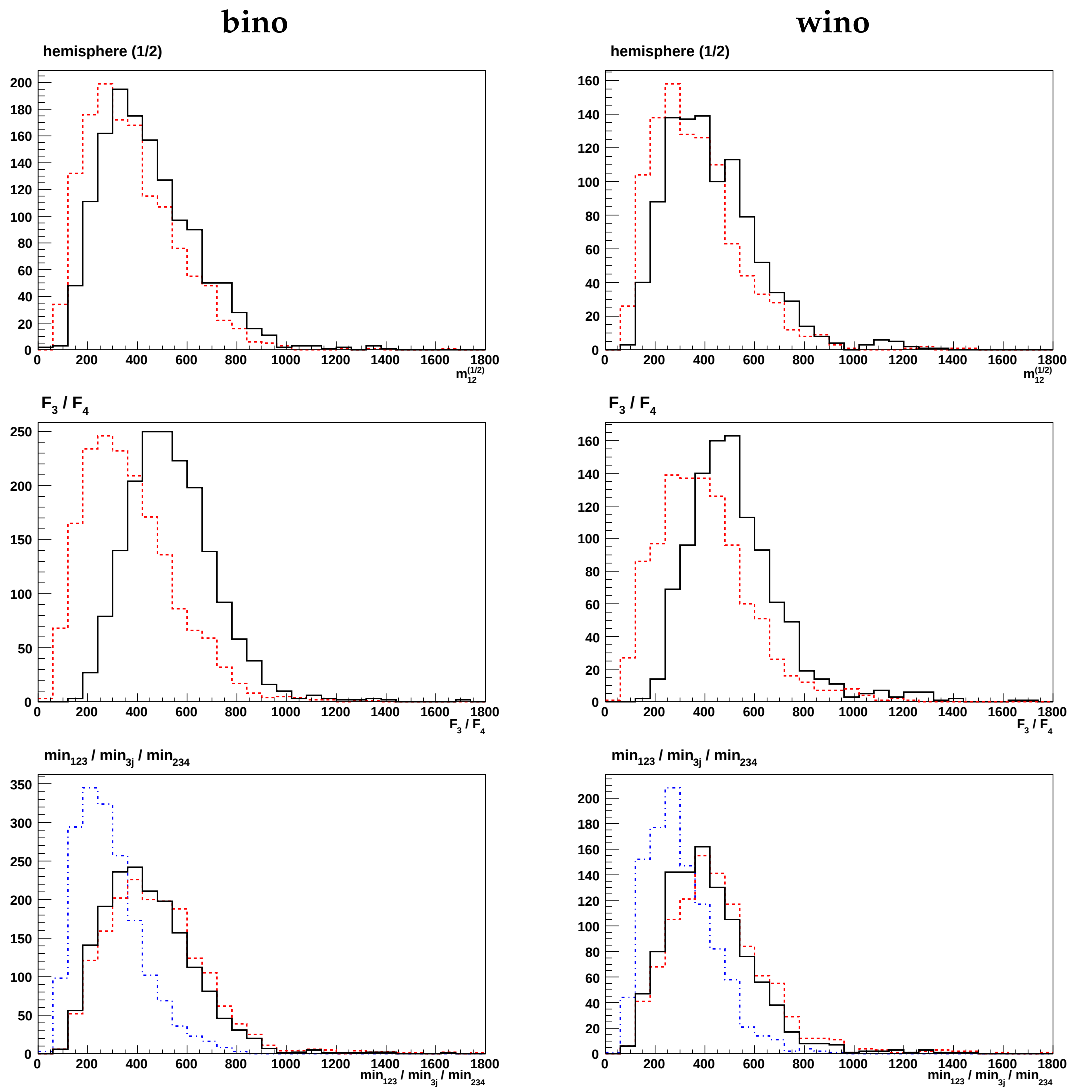

Figure 4.6: Scenario C: distributions of all variables under investigation. The histogram labeling is the same as in Figure 4.4.

find all variables give good results in that a (mostly) linear drop of the distribution down to the clear edge structure is evident. At most for min_{123} and min_{3j} the endpoint is slightly lower than expected. This can be ascribed to low statistics, to which endpoints measurements are in general very vulnerable by their very nature. Since scenario C has the least events of all scenarios, a slight tendency of underestimation is also expected.

Due to the lower edge position, the wino selection is not affected by the issue of statistical underestimation. A small fraction of remaining bino events overshoots the true endpoint and yields very pronounced kinks in basically all distributions that

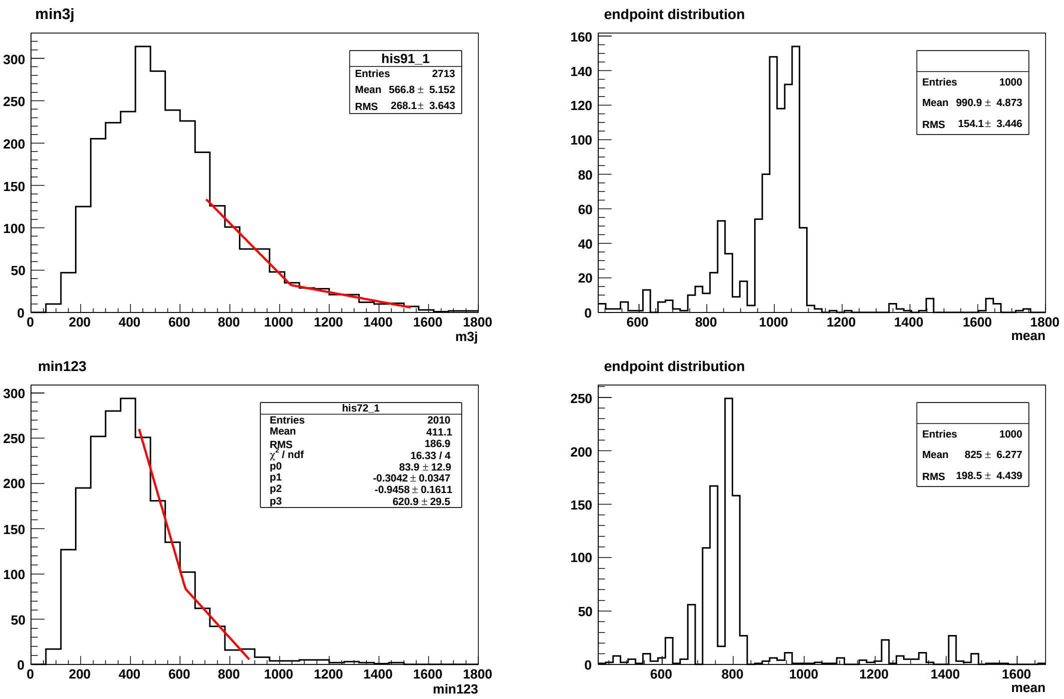

Figure 4.7: Two examples of endpoint fit distributions: in the first row min_{3j} (top, left) and the corresponding endpoint distribution (top, right) are depicted in scenario B. The second row features min_{123} (bottom, left) and the respective endpoint distributions (bottom, right) in scenario C.

allow for a separate extraction of the wino edge.

4.6 Endpoint Determination

Finally it is our aim to quantify the actual endpoint positions of the discussed variables in all three scenarios. The tool of choice for this job is again the edge-to-bump method [61] in the specially adapted version introduced in Chapter 2. In a nutshell, the approach fits a naive linear kink function 1000 times over randomly generated sub-domains of the complete invariant mass spectrum, before the relevant fit parameters are extracted to create a statistical distribution of fit results. In Chapter 3 we made use of three fit parameters, namely the two slopes and the actual kink position whereas at this point we only need the kink parameter i.e. the supposed endpoint position. Two examples of the application of the edge-to-bump method and the resulting endpoint fit distributions are given in Figure 4.7. For min_{3j} in scenario B we

endpt.	min_{123}	min_{234}	min_{3j}	$m_{12}^{(1)}$	$m_{12}^{(2)}$	F_3	$F4$
scenario A							
bino	1106 ± 52	570 ± 14	1125 ± 106	822 ± 21	**1012 ± 104**	686 ± 33	1191 ± 132
wino	908 ± 83	665 ± 34	948 ± 99	932 ± 31	**780 ± 26**	**794 ± 33**	1031 ± 53
scenario B							
bino	**986 ± 36**	773 ± 147	**1028 ± 34**	**1010 ± 6**	794 ± 49	766 ± 25	1046 ± 66
wino	895 ± 23	**748 ± 68**	892 ± 18	958 ± 10	**819 ± 47**	911 ± 51	928 ± 37
scenario C							
bino	812 ± 24	545 ± 8	**921 ± 37**	816 ± 29	721 ± 90	708 ± 22	**894 ± 57**
wino	778 ± 23	577 ± 19	**804 ± 6**	769 ± 47	764 ± 14	708 ± 38	**793 ± 7**

Table 4.2: Results of the adapted edge-to-bump method for all variables and scenarios. Values highlighted in bold face are the ones closest to the true endpoint.

observe a shallow endpoint structure with a longer tail in the invariant mass spectrum which translates to a broad width of the main peak in the statistical endpoint fit distribution. min_{123} in scenario C on the other hand has a very pronounced edge close to the true value of 800 GeV which is reflected in a relative narrow peak width in the resulting endpoint fit distribution. More importantly, for both variables the peak in the statistical endpoint distribution is tightly correlated with the theoretical value. Using the exact same iterative procedure as described in Chapter 2 we reduce the impact of background noise and contributions far off the main peak in the fit results of all variables in all scenarios, the results of which are the values featured in Table 4.2. In there bold figures represent the most accurate ones, i.e. closest to the theoretically expected endpoints. The first impression of these values confirms the observations from section 4.5: there is not a single variable which works perfect for all scenarios but one rather has to carefully choose which variable to use for the corresponding endpoints. Our results furthermore suggest that it might be necessary to use more than one variable and that a preceding clarification of the particular type of underlying mass spectrum is mandatory. An indication for the type of mass scenario may be obtained by a careful study of inclusive jet multiplicities (cf. Figure 4.2) or signal cross-sections.

In scenario A, the best results are obtained by the variables $m_{12}^{(2)}$ for the bino selection and $m_{12}^{(2)}$ as well as F_3 for the wino selection. The success of these variables may be explained by the asymmetric nature of this spectrum. Both min_{3j} and min_{123} slightly overshoot the true endpoint by 100 GeV but agree within two sigma statistical significance and correctly identify the mass difference of 200 GeV between bino and wino edge. As for scenario B, an additional high-p_T jet in combination with two signal gluinos severely influences the proposed endpoint measurements due to the largest combinatorial backgrounds of all three scenarios. Nevertheless min_{123}, min_{3j} and $m_{12}^{(1)}$ all give good results for the bino selection criteria while in the wino case both $m_{12}^{(2)}$ and min_{234} are able to accurately extract an endpoint compatible with the theoretical value. The mass differences between the bino and wino edges are however underestimated for all variables confirming the earlier mentioned assumption that distributions for bino and wino selections resemble each other in this scenario. Hence we emphasize the importance of appropriate variable choice for the different selection criteria of bino and wino. In the *ideal* scenario C the situation is two fold. On one hand, all variables in the bino selection systematically underestimate the endpoints with respect to the true value, although combinatorial and SUSY backgrounds are the smallest of all three spectra. This bias towards lower edge positions can be understood as a mere effect of poor statistics. The signal cross-section for SUSY processes is the smallest in this scenario and the invariant mass distributions contain only $\mathcal{O}(1000)$ events after baseline and selection cuts. Moreover, the linear kink fit method underestimates endpoints in the limit of low event counts. Hence through an artificial increase of events we confirm that the underestimation trend is resolved. The wino selection on the other hand exhibits good results for nearly all variables with correspondingly small errors.

Finally a caveat is in place: the quoted errors above are obtained with the iterative procedure introduced in Chapter 2 and describe the impact of statistical fluctuations from the fit parameters of the edge-to-bump method only. Furthermore there exist other important sources of errors which did not make their way into this analysis: the statistical error of each bin, the dependence of the fit result on the bin width as well as errors with greater physical relevance such as the existence of multiple kinks in the underlying distributions, systematic errors in the definitions of the variables or SM background influences. All these effects are expected to contribute to the errors with the same size as the quoted ones. A dedicated study of those is beyond the scope of this work but nonetheless an important topic for the endpoint determination of gluino dijet signatures.

Summary

Summing up, in this chapter we analysed the gluino dijet mass edge measurement in a fully inclusive hadron collider environment, that is event samples of all possible SUSY signatures and their respective decay modes including distorting effects of initial state radiation, hadronisation and detector smearing. Moreover we proposed two distinct selection criteria that allow for a separation of otherwise intrinsically overlaid gluino dijet mass edges, that originate from decay modes into different light gauginos. Using a semi-simplified model with three different squark masses, we studied to what extent SUSY and combinatorial backgrounds affect the gluino dijet endpoint measurements with the help of newly introduced and existent variables. Their distributions are fitted with the edge-to-bump method to obtain a quantitative estimate of the actual endpoint position. We find that in all three scenarios which are representative for a large part of parameter space favoured by the recent LHC discovery of the presumptive Higgs boson these edges can be disentangled with good accuracy and hence proof the validity of our method.

Chapter 5

Fake Combinatorics from Particles with non-standard quantum numbers

In the last chapter we studied the impact of combinatorics and proposed several variables to reduce the impact of long tails in invariant mass distributions from the combination of uncorrelated objects. However, such distortions of kinematic observables do not necessarily need to originate from combinatorial backgrounds but they may also emerge due to the presence of exotic BSM particles with non-standard quantum number assignments, if they are in reach of the LHC. These so-called 'fake combinatorics' arise in the same way as ordinary combinatorial ambiguities from wrong assignments of particles to different cascades or different positions within a single cascade. The intricate thing is that if particles with non-standard quantum numbers are in the game, they may shift the SM particles' positions to unanticipated places within decay cascades with the result of distorted behaviours of standard variables. As a prime example for such particles we study fermions carrying both lepton and baryon number, which are endowed with a discrete parity leading to the general features of pair production and cascade decays. In what follows, we will briefly sketch how those exotics emerge from extended SUSY models and discuss their characteristics and potential signatures. Finally, we embed these particles into generic SUSY benchmark scenarios and investigate their effects on ordinary decay cascades through a scan of different masses with respect to the underlying spectrum.

5.1 Characteristics and Signatures of exotic chiral Fermions

Many supersymmetric extensions beyond the MSSM feature various new particles which are for instance new gauge bosons or additional matter fermions. In grand unified theories the existence of novel particles is predicted by additional degrees of freedom in the fundamental representations of the associated gauge group. In case of the exceptional Lie group E_6 the fundamental representation is **27**-dimensional and contains new colour triplets among others. The special feature of these triplets are their eponymous couplings to both leptons and quarks, naming the scalar versions *leptoquarks* and the fermionic variants *leptoquarkinos*. In the following, we take the fermions as our candidates for non-standard exotics. Due to an odd R-parity assignment, they entail interesting phenomenological consequences: a cascade-like decay structure through typically long cascades similar to that of ordinary SM superpartners. The phenomenological details of these models can be found in [92, 93], while the model-building aspects are discussed in [94, 95, 96, 97, 98].

We take these models as a motivation for the existence of such particles, but adopt a completely phenomenological view and simply embed the leptoquarkinos into two gravity-mediated SUSY spectra, *SPS1a* and *SPS3*, as well as a gauge-mediated SUSY spectrum, *SPS7* [68, 99]. These scenarios differ with respect to their masses and signatures and they are chosen to reflect generic aspects of SUSY models.

Leptoquarkinos are either produced in pairs or singly in association with a slepton. While the former is a pure QCD process and as such only determined by the mass of the exotic fermion, the latter depends on the size of the unknown Yukawa coupling y. Generically, due to their colour charge leptoquarkinos are expected to be copiously produced at the LHC. Their decay patterns are much more model-dependent and dominated by two properties: the Yukawa coupling y and the underlying mass spectrum. In what follows, we take the scalar leptoquarks to be considerably heavier than their fermionic counterparts, based on the fact that the leptoquarkino mass parameter m_D itself is part of the scalar leptoquark mass [100, 101]. Furthermore, we are agnostic about model assumptions and simply choose to set the size of the Yukawa coupling equal to the electromagnetic coupling $y = 0.312$ and hence allow for non-vanishing single production and more importantly observable decays of the exotic fermions at the LHC. In Figure 5.1 (a) we depict the leading order[1] cross section for

---

[1] Next-to-leading order cross sections for these exotics are currently unavailable. In that sense, these figures are conservative, since the cross-sections of coloured particles are in general known to increase

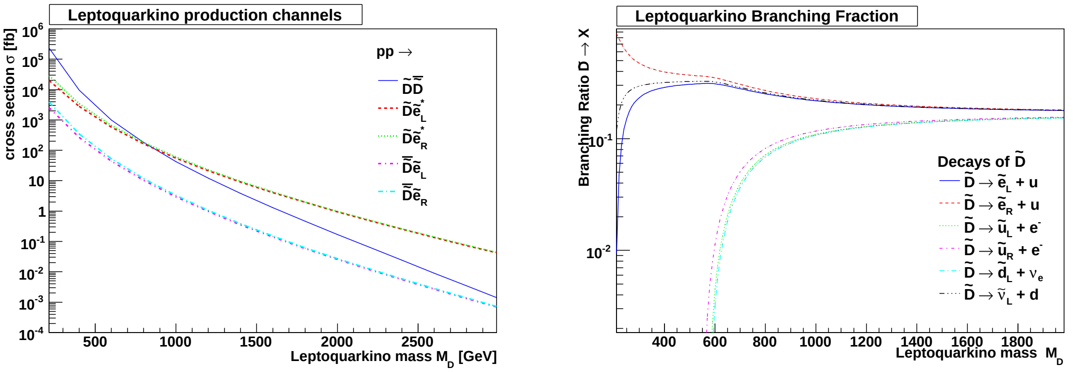

(a) (b)

Figure 5.1: Leading order cross section at 14 TeV (a) and branching ratios for an underlying SPS1a-like spectrum (b), both for varying leptoquarkino masses and a fixed Yukawa coupling $y = 0.312$.

a 14 TeV LHC. For small leptoquarkino masses m_D, the exotics are predominantly produced in pairs. Increasing the mass parameter however yields a larger rate for singly produced leptoquarkinos, which starts to dominate the production in the high mass regime. This discrepancy of single and pair production is a phase space effect since the production of two heavy fermions is merely suppressed.

According to the branching ratios in Figure 5.1 (b), the decay of the leptoquarkino is given by the slepton modes in vast regions of the mass range, since the squark modes are either kinematically forbidden or heavily phase space suppressed. Thus, we safely assume the slepton modes to be the dominant decay pattern, which results in the following quite generic decay cascades:

$$\tilde{D} \longrightarrow q\tilde{l}^{\pm}_{L/R} \longrightarrow q l^{\pm}\tilde{\chi}^0_1 \tag{5.1}$$

where q is either a quark or an antiquark. Hence, a signal of pair produced leptoquarkinos yields the exclusive final state of (at least) two hard partonic jets, two opposite sign same flavour (OSSF) leptons and large amounts of missing transverse energy. Signatures of squarks, on the other hand, may show precisely the same final states, e.g. for an asymmetric prompt squark decay into quark and neutralino on one side and a *golden chain*-like decay on the other side (cf. Figure 5.2).

Following the general assumption of minimal flavour violation in SUSY scenarios

---

in precision calculations.

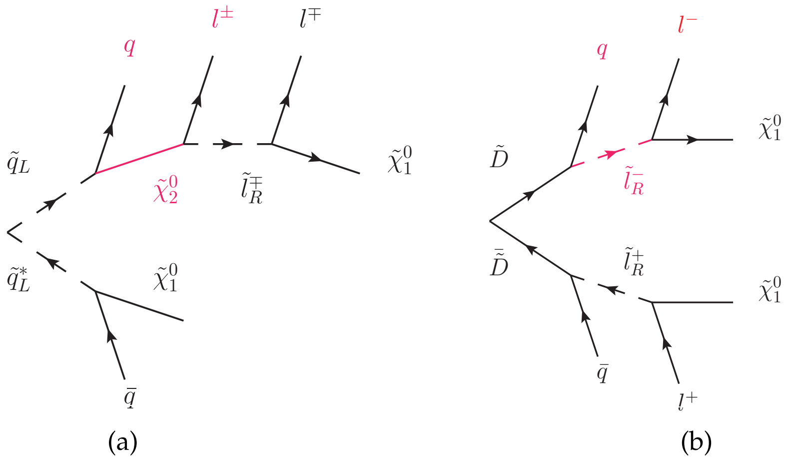

Figure 5.2: Typical squark (a) and leptoquarkino (b) decay cascades with the same exclusive final states of 2 jets, 2 leptons and $\not{E}_T$. The difference of intermediate propagators affecting jet-lepton observables is highlighted in red.

motivated by past and present measurements, flavour is a conserved quantity (up to CKM). Hence, OSSF leptons from squark decays are equally likely than opposite sign different flavour (OSDF) leptons (up to a combinatorial factor) for standard MSSM paradigms, where branching fractions for the first two generations are generally of the same size. In a pure leptoquarkino signal these OSDF contributions are absent since the flavour of the lepton is the same as the flavour of the exotic mother particle for the naive assumption of diagonal Yukawa couplings and standard constraints from flavour changing neutral currents. This bears the opportunity to discriminate the contributions from exotic and ordinary superpartners as we will see later on.

5.2 Mass Edges with chiral Exotics

The physiognomy of mass edges with chiral exotics is depicted in Figure 5.2, which constitute the main processes for a SUSY background (a) and a leptoquarkino signal (b). There are two major differences of vital importance. First of all, both leptons originate from one particular decay chain for squark *backgrounds*, whereas only one lepton per cascade is emitted in case of leptoquarkino *signatures*. A long tail in the invariant mass distributions results from the combination of such a lepton with a completely uncorrelated quark from the opposite and thus wrong cascade. Secondly, the intermediate particle between quark and lepton is of fundamentally different nature. The squark backgrounds possess an intermediate second-to-lightest neutralino, a Majorana fermion, which allows for spin information to be communicated between the two partons. As we have seen in Chapters 2 and 3, these correlations affect the shape of the invariant mass distribution and hence allow for a discrimination between fundamentally different models of spin. The leptoquarkino cascade on the other hand has an intermediate scalar particle, namely a slepton, between quark and lepton, the invariant mass distribution of which is given by the pure phase space distribution of prominent triangular shape.

The theoretical endpoint value is determined by the masses of the involved particles (cf. Chapter 2 and Appendix A). Therefore, if the exotic mass is located in the ballpark of the squark mass, and sizable production and decay are assured by a non-negligible Yukawa coupling, construction of these invariant masses from the same exclusive final state yields a superposition of both edges from squarks and leptoquarkinos. On one hand, a relatively light exotic dominates the production and also the decay patterns. Heavy leptoquarkinos on the other hand exhibit the opposite behaviour: squark contributions will dominate the distributions and occasionally show a small distortion from the expected shape. In summary, the endpoints of jet lepton distributions are distorted in two ways with respect to their shapes in standard MSSM cascades: an overall endpoint shift due to different masses of the particles in the two subsequent two-body decays as well as a long tail from the inevitable inclusion of a lepton from a different cascade.

Other BSM models allow for similar signatures due to differing intermediate propagators, e.g. non minimal versions of UED. Nevertheless, in the following we concentrate on the specific case introduced above and take this setup as an application prototype to investigate how deviations from an intermediate scalar may distort mass edges in the context of a typical SUSY decay cascade.

Since our exotics possess both lepton and baryon number, in the subsequent analysis we concentrate on variables which include these. More precisely, we restrict ourselves to the following four observables: $m_{ql,low}, m_{ql,high}, m_{qll}, m^*_{ql}$. While the first three have already been discussed in Chapter 2, the last variable was proposed in [100]. It is defined as

$$m^*_{ql} = m(\min_{p_T}\{j_1, j_2\}, \max_{p_T}\{l^+, l^-\}), \tag{5.2}$$

m	*SPS1a*	*SPS3*	*SPS7*
$\tilde{u}_L$	567	865	903
$\tilde{u}_R$	547	835	872
$\tilde{l}_L$	204	288	262
$\tilde{l}_R$	145	181	131
$\tilde{\chi}_2^0$	181	304	272
$\tilde{\chi}_1^0$	97	162	163

Table 5.1: SUSY masses in units of GeV for three different underlying SPS spectra used in the numerical analysis. All masses were generated with `SPheno` [102] according to [68].

which is the invariant mass of the hardest lepton and the softest jet from an exclusive two-jet, two-lepton and $\not{E}_T$ final state. The difference between the last and the former three observables is a combinatorial one. The first three exclusive variables require an a priori decay cascade assignment. m^*_{ql} on the other hand is an inclusive variable and by definition free of combinatorial ambiguities for the application to the exclusive final state of two jets and two leptons.

To compare exotic and *standard* SUSY signatures, we scan the leptoquarkino masses from 400 to 1200 GeV with steps of 200 GeV, centred around the squark mass of the respective underlying SPS spectrum. As an overview, we give all relevant masses of these spectra in Table 5.1. At the time this study was published [93], squark exclusion bounds from the LHC were less strict than to date [103, 104, 105, 89]. However, for the other, heavier spectra we will see that the feature we are about discuss are rather generic and the size of the effect merely depends on the relative mass difference of exotic fermions and standard squarks. The exclusions bounds for scalar leptoquarks top out around 600 GeV [106, 107, 108] whereas for the fermionic leptoquarkinos the closest applicable exclusion is presumably a heavy bottom quark at 400 GeV, which, however, has different decay patterns [109].

The numerical setup is as follows: for each model, we simulated 10K unweighted events with the event generator `WHIZARD` [73, 74] using a hard-coded implementation of an E_6-inspired SUSY model sketched above, that gives rise to exotic states. The parts responsible for production and decay have been extensively tested and validated, partially using the `WHIZARD` interface to `FeynRules` [79]. The selection criteria for the partonic jets are a minimum transverse momentum of $p_T^{\min} = 50$ GeV. When

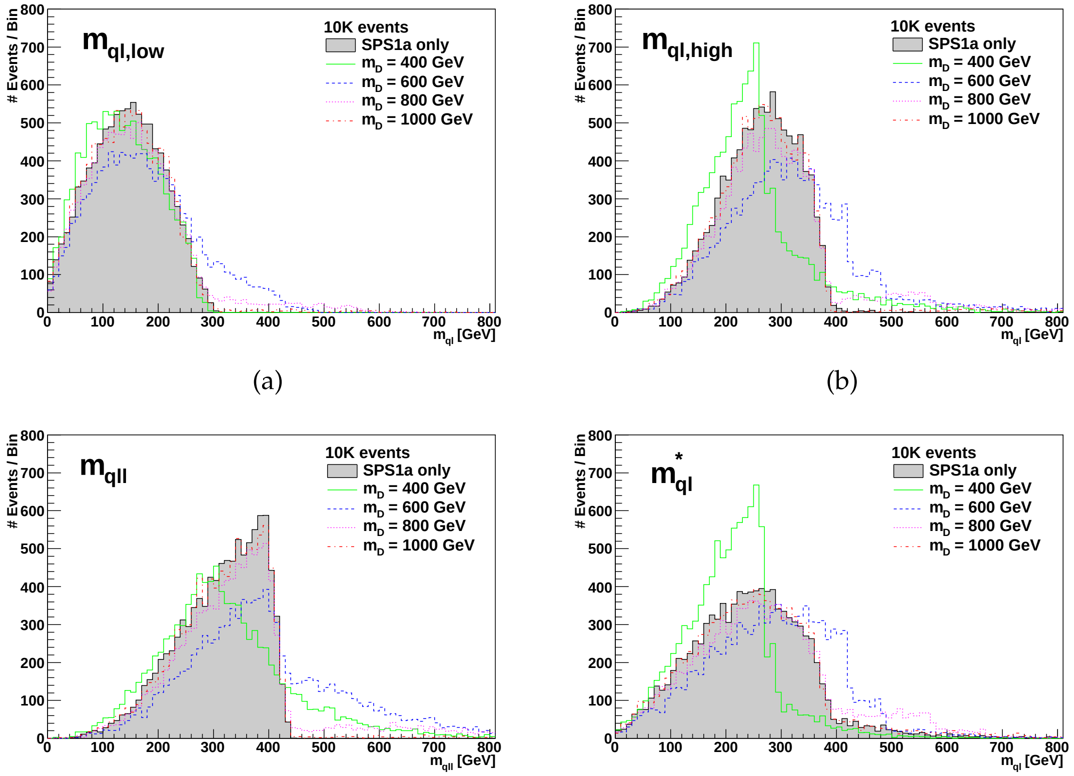

(a) (b)

(c) (d)

Figure 5.3: Four different mass edges for varying leptoquarkino masses embedded into an SPS1a spectrum: $m_{ql,low}$ (a), $m_{ql,high}$ (b), m_{qll} (c) and m^*_{ql} (d). Continuous, dashed, dotted and dash-dotted lines correspond to leptoquarkino masses of 400, 600, 800 and 1000 GeV, respectively.

we extend the exclusive two-jet sample, this cut reduces backgrounds from additional ISR contaminations. For jet multiplicities of four, more care is needed to avert the inclusion of an additional background: gluino pair production. In this case, the third hardest jet has to be smaller than 50 GeV. The contamination of gluino-squark associated production is also known to be accompanied by hard ISR jets [82] and may hence constitute an additional SUSY background[2]. Despite all this, we assume the jet background to be under control. A complete background analysis is beyond the intent of this work and neglected here, since after all we are confident that the basic criteria given above are sufficient to reduce SUSY backgrounds to a minimum so as to allow for a distinction between a plain MSSM cascade structure and novel signatures of exotic fermions therein.

---

[2] cf. the discussion of SUSY backgrounds in Chapter 4.

5.3 True and Fake combinatorics in Cascades

In this section we discuss the kinematic distributions containing chiral exotics in detail, depicted in Figures 5.3, 5.4 and 5.5. In the *SPS1a* scenario (cf. Figure 5.3), we note the modulated strength of exotic signatures for varied masses. The scan yields a dominant exotic signal for large negative mass differences of exotics and squarks, i.e. lighter leptoquarkinos, which starts to balance the pure squark signatures in the regime of equal masses (up to ± 50 GeV). Further increasing the mass difference to values of +200 GeV results in rather small deviations which completely vanish for exotic masses which are heavier by more than 400 GeV. This shows that leptoquarkino masses well above 200 GeV heavier than the corresponding squark mass of the underlying spectrum contribute only to little extent to dedicated analysis methods. Or more specifically, very heavy exotics (with respect to typical SUSY masses) will most certainly not influence *standard* analysis procedures.

For exotic fermion masses close to or below the squark values, we find tremendous discrepancies. Consider the two quark-lepton observables $m_{ql,low}$ and $m_{ql,high}$ which both have a minimisation or maximisation procedure over two leptons in their definition. As mentioned earlier, while in standard MSSM paradigms the two OSSF leptons are originating from one particular side, the leptoquarkino signature allows for OSSF leptons from two different cascades. Consequently, in Figure 5.3 (a) and (b) we observe long tails in the distributions arising from the combination of uncorrelated leptons. However, due to the minimisation procedure of $m_{ql,low}$, the effects there are less pronounced compared to the distortion of $m_{ql,high}$.

The three-particle invariant mass m_{qll} also lacks a clear endpoint structure for small values of the exotic mass. Nonetheless, as Figure 5.3 (c) depicts in terms of the blue dashed line corresponding to $m_D = 600$ GeV, a visible kink starts to appear at the true squark endpoint. This is something we would expect to see in an inclusive event sample after taking into account polluting effects of ISR, hadronisation and detector response (cf. discussion in Chapter 4), but not already at this early partonic stage. At this point we want to make a remark. The shallow endpoint behaviour of the distributions in Figure 5.3 (a), (b) and (c) may not unequivocally point to exotic signatures. More importantly, if a mass edge is distorted by few events outside the actually kinematically accessible region (i.e. beyond the endpoint), it might also indicate, that a *standard* squark analysis with a preceding decay cascade differentiation went berserk and momentum assignments to different sides of cascades utterly

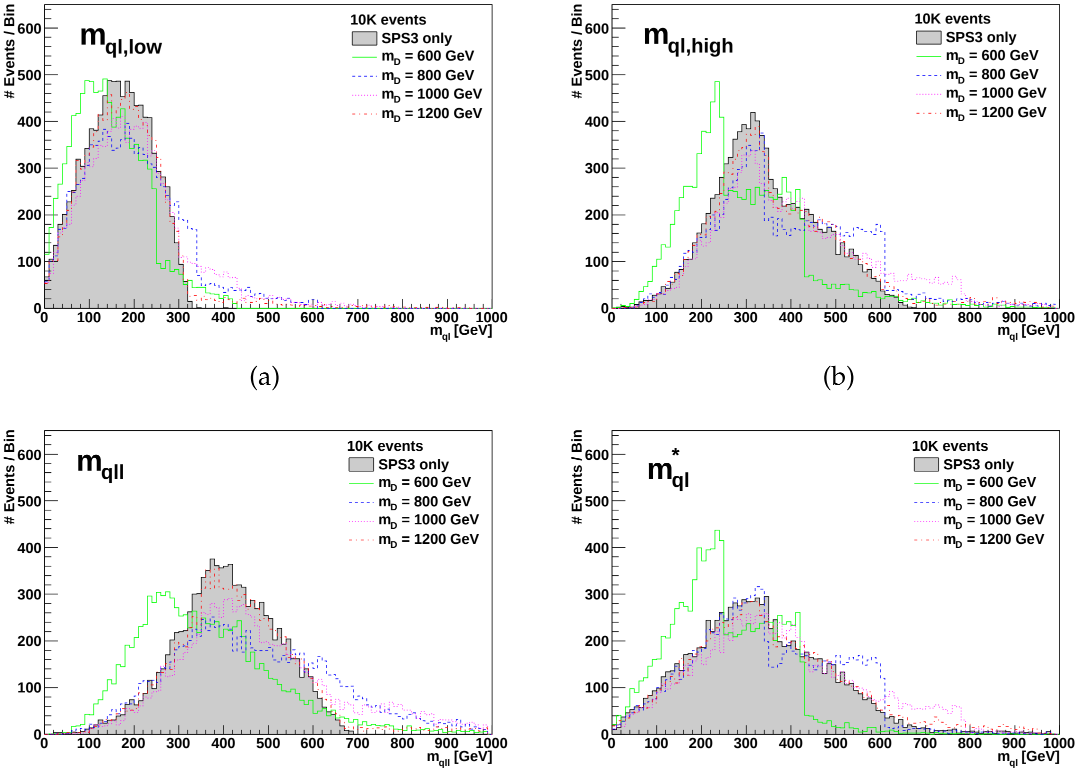

(a) (b)

(c) (d)

Figure 5.4: Same as Figure 5.3, but instead dressed with an underlying SPS3 spectrum. Also note the overall shift of 200 GeV in leptoquarkino mass values due to the higher squark masses.

failed (cf. combinatorial backgrounds discussed in Chapter 4). Therefore we want to stress the importance of a careful analysis not only of the data, but also of the underlying model assumptions. A slight variation thereof might also account for distorting effects otherwise ascribed to false combinatorial assignments.

Concerning the new variable m^*_{ql}, the distributions in Figure 5.3 (d) clearly justify its introduction. For the case of $m_D = 400$ GeV, existing variables such as $m_{ql,high}$ exhibit a structure at the vicinity of the true leptoquarkino endpoints of 277 and 302 GeV (for two possible intermediate sleptons), but the kink of m^*_{ql} at this edge is much more pronounced. Similar statements hold for the heavier exotics, as long as they are not overwhelmed by the underlying squark production.
Turning to the scenario *SPS3*, we find a similar picture for all four variables. Since it is reasonable to centre the scan of leptoquarkino masses around the actual squark masses, we increased the starting point of m_D by 200 GeV up to 600 GeV. The two-

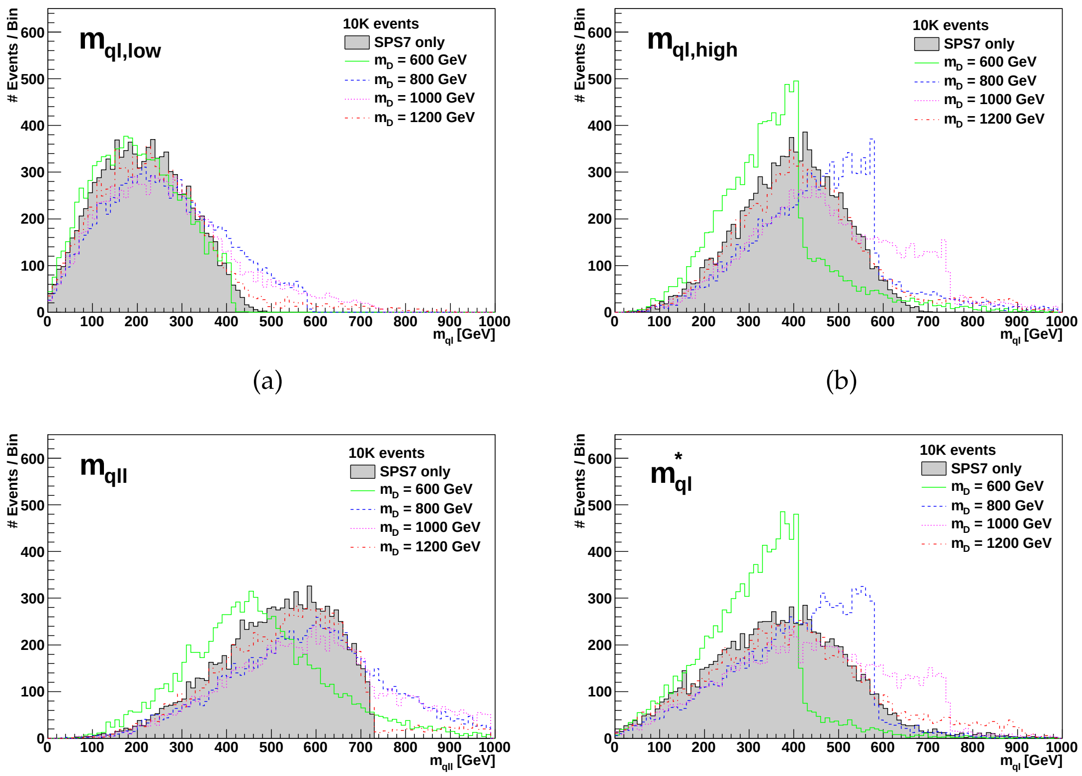

(a) (b)

(c) (d)

Figure 5.5: Same as Figure 5.4, but instead dressed with an underlying SPS7 spectrum.

fold kink behaviour visible in 5.4 (b) and (d) may be attributed to the spectrum: the masses of *SPS3* are such that an almost equal amount of exotic decays takes place through either left- or right-chiral sleptons. Apart from that, the discrepancies with respect to the underlying scenario tend to be even larger for low exotic masses and less washed out for higher masses. In the GMSB scenario *SPS7*, squark masses of $\sim$ 900 GeV allow for even heavier leptoquarkinos to stay visible. The exotic benchmark masses of 800 and 1000 GeV still show huge deviations in Figure 5.5 and it is only at a difference of leptoquarkino to squark mass of 300 GeV that the distortions get washed out and start to dissappear in the underlying spectrum.

To further quantify the ability to distinguish leptoquarkino from squark signatures, we exploit the (non-) existent correlation of the two OSSF leptons. In the case of squark signatures, the di-lepton invariant mass has the same property as the quark-lepton invariant mass for the exotics: an intermediate scalar propagator and

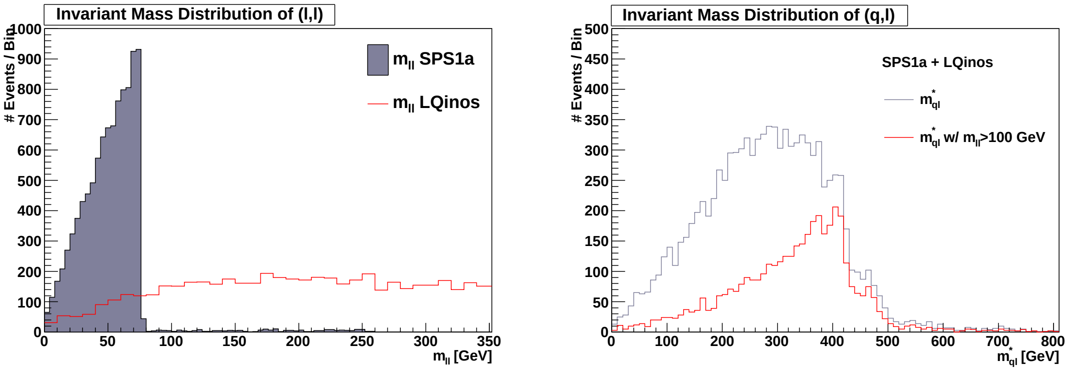

(a) (b)

Figure 5.6: The di-lepton spectrum of both leptoquarkino and squark signatures (a) as well as m^*_{ql} before and after the application of a cut ($m_{ll} > 100$ GeV), designed to suppress SUSY backgrounds (b), for m_D = 600 GeV.

a corresponding triangular phase space distribution. The di-lepton spectrum of leptoquarkino signatures on the other hand is rather flat, as can be seen in Figure 5.6.

Hence, an observation of a kink in the dilepton spectrum may indicate the kinematic endpoint of a vanilla MSSM signal augmented by new exotics. Requiring the invariant mass of the leptons to be above this particular kink position would thus yield events that could ideally be attributed to leptoquarkino signatures. In this way, we are able to quantify the separability of both processes for the benchmark scenario *SPS1a* with the cut $m_{ll} > 100$ GeV and furthermore give an estimate in terms of signal (after cut) to signal + background (before cut) ratios assuming a 7 TeV LHC[3] and

m_D	N_{inc}	N_{sig}	S / $\sqrt{\text{S+B}}$
400	8763	5061	54
600	1355	540	15
800	684	102	4
1000	594	24	1

Table 5.2: Inclusive number of events before ($N_{inc} \equiv S + B$) and after cut ($N_{sig} \equiv S$) and the corresponding signficance estimate for 100 fb^{-1} at 7 TeV.

---

[3] The generic features persist for other centre-of-mass energies such as the current 8 TeV or the planned 14 TeV, since the effects are manifest in *invariant* masses and based only on the relative mass difference of exotic and standard particle content.

100 fb^{-1}. The numerical values in Table 5.2 confirm the qualitative observations from Figure 5.3: while the apparent discrepancies for small exotic masses are supported by overwhelmingly high significance estimates, the washed out edge behaviour for heavier masses corresponds to rather low signal to background ratios.

Summing up, we analysed the issue of so-called fake combinatorics, i.e. the problem of false assignments of particles to correct decay cascades due to additional chiral fermions with non-standard quantum numbers, which are motivated in context of a GUT-inspired SUSY model. The presence of the exotic states in decay cascades drastically alters the shape of invariant mass distributions. These distorting effects in several mass determination variables arise from intermediate propagators with different spin assignments. However, these do not stem from fundamentally different underlying model assumptions (e.g. a non-minimal version of UED) but rather due to a slight extension of a standard MSSM paradigm. Hence, in these scenarios a confusion in terms of model discrimination is imminent. The contribution of leptoquarkinos in *usual* squark analysis method ranges from strong dominance to small deviation in terms of uncorrelated tails. These effects are likely to be misidentified as potentially false decay cascade assignments and thus they threaten not only the correct determination of model parameters but also a possible discovery of novel, perhaps exotic physic signatures.

Chapter 6

Summary and Outlook

Signatures of new physics are eagerly anticipated to be observed in the near future at the LHC, since various shortcomings of the Standard Model of elementary particle physics motivate the presence of new physics at the TeV scale. The very recent discovery of the supposed Higgs boson further supports the search for new phenomena. After a potential discovery of new particles, it is of utmost importance to determine their intrinsic properties: the measurement of masses and spins form two major corner stones. In recent years a plethora of methods have been developed to measure the masses of novel particles and discriminate different models through spin-sensitive observables. However, several obstacles arise in determining these fundamental model parameters. Hence, we investigate two prominent and often neglected complications in three different parts of this thesis: the impact of combinatorial and off-shell effects in new physics cascades on mass and spin measurements.

For one, many new physics signatures are simulated using the Narrow-Width Approximation due to the inherent complexity of the models and the sheer amount of final state particles in the event, in spite of the compliance with its basic requirements. This motivates our study of a naive violation of one of these conditions: the impact of a 'broad' resonance with considerable non-resonant contributions on mass and spin determination methods. Our investigation is based on SUSY signals from gluinos whose total width Γ is varied according to a discrete set of effective width-to-mass ratios $\gamma = \Gamma/M$ ranging from 0.5 % up to 15.0 %. We simulate these signals with a complete matrix-element calculation for the production *and* the first decay step to fully address the effects of off-shell propagator contributions whereas all subsequent decays are factorised in the usual way using the NWA with spin correlations. It turns out that the transverse momentum of the first decay product is substantially increased by these non-resonant effects, and the resulting invariant mass distributions of several mass measurement variables are severely distorted for already moderate values of $\gamma = 5.0\%$. What is more, the endpoint positions of those observables exhibit a considerable dilution, and initially steep edge structures are turned into shallow endpoints. Concerning spin measurements, the impact of a broad gluino is less striking. The investigated shape asymmetries and angular correlations display only a minor dependence on the effective width-to-mass ratio γ and the visible effects are reasonably small. There is, however, one exception: the azimuthal correlation of two quarks within a single decay cascade suffers from strong discrepancies between the narrow ($\gamma = 0.5\%$) and broad ($\gamma = 15.0\%$) gluino samples. The deviation of the latter is strong and the associated asymmetry yields a value which is compatible with the one of the UED sample. Hence, for this exclusive observable, a model discrimination between SUSY and UED is at stake and we conclude that it is mandatory to use several observables to reveal the nature of the spin quantum numbers of the underlying particles. Summing up, our studies show that predictions from a full matrix-element calculation vigorously differ from a naive factorisation procedure based on the NWA for the case of broad resonances. Even though this is an expected behaviour, the huge deviations of invariant mass distributions, especially for mass measurement observables, beautifully illustrate the necessity of accurate predictions. The correct treatment of these off-shell contributions is essential for a precise mass determination of new resonances with already moderate widths. Moreover, as the first decay product of a broad gluino inherits the majority of non-resonant contributions, observables including that particular particle display large deviations. However, at the LHC the situation is such that we even expect to see an influence on variables that do *not* employ the initial decay products, since irreducible combinatorial backgrounds yield a non-vanishing probability to include them into other observables. Consequently, the effects of broad particles are expected to have a substantial impact on *all* variables and the extent to which these are affected is of deep relevance. Therefore, we propose a generic investigation of these indirect influences in a dedicated future study.

Combinatorial ambiguities, on the other hand, are another subject of major importance to LHC physics. Environments at hadron colliders give rise to events with a plethora of jets, not all of which are necessarily originating from underlying physics processes of interest. The combination of completely uncorrelated objects from different decay cascades to invariant masses yields long tails in distributions and poses a severe irreducible background to most endpoint measurements. To overcome these issues, various methods have been proposed to reduce the impact of these combinatorics. Some of these procedures rely on the precise knowledge of the gluino dijet edge, which is assumed to be easily measurable. However, this measurement itself suffers from combinatorial and SUSY backgrounds, which motivated us to study this particular endpoint in three phenomenologically distinct but fully inclusive scenarios, i.e. event samples with all possible SUSY production and decay patterns including additional effects from initial and final state radiation, hadronisation as well as detector response. At first, we disentangled the contributions of two distinct gluino edges originating from two decay modes into light gauginos by means of crude selection criteria. Next, we proposed new variables and compared them to existing ones in order to address the intrinsic contributions of combinatorial backgrounds. Finally, we employed an adjusted version of the Edge-to-Bump method to quantify the actual endpoint positions and to compare the results of all variables. Our results show that, in principle, we are able to extract all of these endpoints separately. However, no single variable works perfectly for both of the two endpoints in all scenarios. Instead, one has to carefully choose the appropriate observable for endpoint determination depending on the spectrum and selection criteria. The obtained endpoints are in good agreement with the theoretical expectations, although there are moderate discrepancies between the three scenarios. In large parts this may be attributed to the error estimates of the Edge-to-Bump method, which are purely statistical. Yet, there exist other important sources of errors such as systematics from the variable definitions, SM backgrounds and the existence of multiple kinks among others. A comprehensive study of those is of crucial importance for gluino dijet endpoint measurements and remains to be investigated in future work.

However, the effects of combinatorial backgrounds, i.e. long tails in invariant mass distributions and distorted endpoint behaviours, do not necessarily need to originate from false assignments of decay products from standard superpartners, but instead they may arise from additional particles with non-standard quantum numbers. The presence of such chiral exotics yields an exchange of the observable decay products positions to unanticipated places within the same or a different cascade and results in a severe distortion of standard kinematic mass determination variables. As a candidate for these non-standard states we studied fermions with lepton and baryon number, that emerge in general theories of grand unification, with an odd R-parity assignment accounting for pair production and cascade decays. In a completely phenomenological approach we embedded these particles into three SUSY benchmark scenarios and scanned their masses relative to the underlying spectrum.

Depending on the mass hierarchy, we find two results. First, small exotic masses in relation to the other superpartners yield huge discrepancies to ordinary squark signals in various jet-lepton observables. Secondly, only small deviations of shallow nature appear in invariant mass distributions, if these states are heavier than squarks by 200 GeV or more. In fact, for this second type of spectra, signals from those exotics are likely to be misinterpreted as distortions from combinatorial backgrounds. In that sense, this kind of setup serves as a prime example to illustrate the necessity of future analyses to disentangle the kinematic properties of newly discovered particles in order not to misidentify the underlying model specifics.

In summary, immediately ensuing the discovery of new physics is the determination of masses and spins of novel particles. Their measurements are crucial to the knowledge of the particular type of underlying new physics model. Prominent scenarios of BSM physics such as UED or SUSY with conserved KK- or R-parity are characterised by demanding event topologies, where large parts of information are effectively lost due to invisibly escaping lightest parity-odd particles. In recent years an active development in this field led to many successful methods of mass and spin determination that are able to deal with the characteristics of events with large portions of missing transverse energy. However, these procedures are often based on ideal case scenarios and they rely on fundamental assumptions, which are not necessarily met. In this thesis we addressed three examples of likely obstacles that may arise in various BSM scenarios, discussed their impact on the measurements and, if possible, illustrated discriminating measures and potential workarounds. After all, there are very interesting times ahead and signatures of new physics are eagerly anticipated to be observed at the LHC.

Appendix A

Compilation of Endpoints

Endpoint	Theoretical Position
$(m_{ll}^{max})^2$	$\frac{(m_{\tilde{\chi}_2}^2-m_{\tilde{l}}^2)(m_{\tilde{l}}^2-m_{\tilde{\chi}_1}^2)}{m_{\tilde{l}}^2}$
$(m_{ql_n}^{max})^2$	$\frac{(m_{\tilde{q}}^2-m_{\tilde{\chi}_2}^2)(m_{\tilde{\chi}_2}^2-m_{\tilde{l}}^2)}{m_{\tilde{\chi}_2}^2}$
$(m_{ql_f}^{max})^2$	$\frac{(m_{\tilde{q}}^2-m_{\tilde{\chi}_2}^2)(m_{\tilde{l}}^2-m_{\tilde{\chi}_1}^2)}{m_{\tilde{l}}^2}$
$(m_{ql_{eq}}^{max})^2$	$\frac{(m_{\tilde{q}}^2-m_{\tilde{\chi}_2}^2)(m_{\tilde{l}}^2-m_{\tilde{\chi}_1}^2)}{(2m_{\tilde{l}}^2-m_{\tilde{\chi}_1}^2)}$
$(m_{ql_{low}}^{max})^2$	$\min\left[(m_{ql_n}^{max})^2, (m_{ql_{eq}}^{max})^2\right]$
$(m_{ql_{high}}^{max})^2$	$\max\left[(m_{ql_n}^{max})^2, (m_{ql_f}^{max})^2\right]$
$(m_{qll}^{max})^2$	$\frac{\left(m_{\tilde{q}}^2-m_{\tilde{\chi}_2}^2\right)\left(m_{\tilde{\chi}_2}^2-m_{\tilde{\chi}_1}^2\right)}{m_{\tilde{\chi}_2}^2}$ for $\frac{m_{\tilde{q}}}{m_{\tilde{\chi}_2}} > \frac{m_{\tilde{\chi}_2}}{m_{\tilde{l}}}\frac{m_{\tilde{l}}}{m_{\tilde{\chi}_1}}$
	$\frac{\left(m_{\tilde{q}}^2 m_{\tilde{l}}^2-m_{\tilde{\chi}_1}^2 m_{\tilde{\chi}_2}^2\right)\left(m_{\tilde{\chi}_2}^2-m_{\tilde{l}}^2\right)}{m_{\tilde{l}}^2 m_{\tilde{\chi}_2}^2}$ for $\frac{m_{\tilde{\chi}_2}}{m_{\tilde{l}}} > \frac{m_{\tilde{l}}}{m_{\tilde{\chi}_1}}\frac{m_{\tilde{q}}}{m_{\tilde{\chi}_2}}$
	$\frac{\left(m_{\tilde{q}}^2-m_{\tilde{l}}^2\right)\left(m_{\tilde{l}}^2-m_{\tilde{\chi}_1}^2\right)}{m_{\tilde{l}}^2}$ for $\frac{m_{\tilde{l}}}{m_{\tilde{\chi}_1}} > \frac{m_{\tilde{q}}}{m_{\tilde{\chi}_2}}\frac{m_{\tilde{\chi}_2}}{m_{\tilde{l}}}$
	$\left(m_{\tilde{q}} - m_{\tilde{\chi}_1}\right)^2$ otherwise
$(m_{qll}^{min})^2$	$\Big[2m_{\tilde{l}}^2(m_{\tilde{q}}^2 - m_{\tilde{\chi}_2}^2)(m_{\tilde{\chi}_2}^2 - m_{\tilde{\chi}_1}^2) + (m_{\tilde{q}}^2 + m_{\tilde{\chi}_2}^2)(m_{\tilde{\chi}_2}^2 - m_{\tilde{l}}^2)(m_{\tilde{l}}^2 - m_{\tilde{\chi}_1}^2)$ $-(m_{\tilde{q}}^2 - m_{\tilde{\chi}_2}^2)\sqrt{(m_{\tilde{\chi}_2}^2 + m_{\tilde{l}}^2)^2(m_{\tilde{l}}^2 + m_{\tilde{\chi}_1}^2)^2 - 16m_{\tilde{\chi}_2}^2 m_{\tilde{l}}^4 m_{\tilde{\chi}_1}^2}\Big] / (4m_{\tilde{l}}^2 m_{\tilde{\chi}_2}^2)$

Endpoint	Theoretical Position	
$(m^{max}_{qq})^2$	$\frac{(m^2_{\tilde{g}}-m^2_{\tilde{q}})(m^2_{\tilde{q}}-m^2_{\tilde{\chi}_2})}{m^2_{\tilde{q}}}$	
$(m^{max}_{q_n l_n})^2$	$\frac{(m^2_{\tilde{g}}-m^2_{\tilde{q}})(m^2_{\tilde{\chi}_2}-m^2_{\tilde{l}})}{m^2_{\tilde{\chi}_2}}$	
$(m^{max}_{q_n l_f})^2$	$\frac{(m^2_{\tilde{g}}-m^2_{\tilde{q}})(m^2_{\tilde{l}}-m^2_{\tilde{\chi}_1})}{m^2_{\tilde{l}}}$	
$(m^{max}_{q_n l_{eq}})^2$	$\frac{(m^2_{\tilde{g}}-m^2_{\tilde{q}})(m^2_{\tilde{l}}-m^2_{\tilde{\chi}_1})}{(2m^2_{\tilde{l}}-m^2_{\tilde{\chi}_1})}$	
$(m^{max}_{q_n l_{low}})^2$	$\min\left[(m^{max}_{q_n l_n})^2, (m^{max}_{q_n l_{eq}})^2\right]$	
$(m^{max}_{q_n l_{high}})^2$	$\max\left[(m^{max}_{q_n l_n})^2, (m^{max}_{q_n l_f})^2\right]$	
$(m^{max}_{qql_n})^2$	$(m^{max}_{qll})^2 \quad \text{with} \quad \left(m_{\tilde{q}}, m_{\tilde{\chi}_2}, m_{\tilde{l}}, m_{\tilde{\chi}_1}\right) \longrightarrow \left(m_{\tilde{g}}, m_{\tilde{q}}, m_{\tilde{\chi}_2}, m_{\tilde{l}}\right)$	
$(m^{max}_{qql_f})^2$	$(m^{max}_{qll})^2 \quad \text{with} \quad \left(m_{\tilde{q}}, m_{\tilde{\chi}_2}, m_{\tilde{l}}, m_{\tilde{\chi}_1}\right) \longrightarrow \left(m_{\tilde{g}}, m_{\tilde{q}}, m_{\tilde{\chi}_2}, m_{\tilde{\chi}_1} m_{\tilde{\chi}_2} / m_{\tilde{l}}\right)$	
$(m^{max}_{qql_{high}})^2$	$\max\left[(m^{max}_{qql_n})^2, (m^{max}_{qql_f})^2\right]$	
$(m^{max}_{qql_{low}})^2$	$(m^{max}_{qql_n})^2$	for $m^2_{\tilde{\chi}_1} + m^2_{\tilde{\chi}_2} < 2m^2_{\tilde{l}}$
	$(m^{max}_{qql_f})^2$	for (condition (1))
	$(m^{max}_{qql_{eq}})^2$	otherwise
$(m^{max}_{q_n ll})^2$	$(m^{max}_{qll})^2 \quad \text{with} \quad m_{\tilde{q}} \longrightarrow m_{Y'} = \sqrt{m^2_{\tilde{g}} - m^2_{\tilde{q}} + m^2_{\tilde{\chi}_2}}$	
$(m^{max}_{qqll})^2$	$\frac{\left(m^2_{\tilde{g}}-m^2_{\tilde{q}}\right)\left(m^2_{\tilde{q}}-m^2_{\tilde{\chi}_1}\right)}{m^2_{\tilde{q}}}$	for $\frac{m_{\tilde{g}}}{m_{\tilde{q}}} > \frac{m_{\tilde{q}}}{m_{\tilde{\chi}_2}} \frac{m_{\tilde{\chi}_2}}{m_{\tilde{l}}} \frac{m_{\tilde{l}}}{m_{\tilde{\chi}_1}}$
	$\frac{\left(m^2_{\tilde{g}}m^2_{\tilde{\chi}_2}-m^2_{\tilde{q}}m^2_{\tilde{\chi}_1}\right)\left(m^2_{\tilde{q}}-m^2_{\tilde{\chi}_2}\right)}{m^2_{\tilde{q}}m^2_{\tilde{\chi}_2}}$	for $\frac{m_{\tilde{q}}}{m_{\tilde{\chi}_2}} > \frac{m_{\tilde{\chi}_2}}{m_{\tilde{l}}} \frac{m_{\tilde{l}}}{m_{\tilde{\chi}_1}} \frac{m_{\tilde{g}}}{m_{\tilde{q}}}$
	$\frac{\left(m^2_{\tilde{g}}m^2_{\tilde{l}}-m^2_{\tilde{\chi}_2}m^2_{\tilde{\chi}_1}\right)\left(m^2_{\tilde{\chi}_2}-m^2_{\tilde{l}}\right)}{m^2_{\tilde{l}}m^2_{\tilde{\chi}_2}}$	for $\frac{m_{\tilde{\chi}_2}}{m_{\tilde{l}}} > \frac{m_{\tilde{l}}}{m_{\tilde{\chi}_1}} \frac{m_{\tilde{g}}}{m_{\tilde{q}}} \frac{m_{\tilde{q}}}{m_{\tilde{\chi}_2}}$
	$\frac{\left(m^2_{\tilde{g}}-m^2_{\tilde{l}}\right)\left(m^2_{\tilde{l}}-m^2_{\tilde{\chi}_1}\right)}{m^2_{\tilde{l}}}$	for $\frac{m_{\tilde{l}}}{m_{\tilde{\chi}_1}} > \frac{m_{\tilde{g}}}{m_{\tilde{q}}} \frac{m_{\tilde{q}}}{m_{\tilde{\chi}_2}} \frac{m_{\tilde{\chi}_2}}{m_{\tilde{l}}}$
	$\left(m_{\tilde{g}} - m_{\tilde{\chi}_1}\right)^2$	otherwise

Both (condition (1)) and $(m^{max}_{qql_{eq}})^2$ are given in [52].

Appendix B

Spectrum of pMSSM Scenario

value	input parameter
1.000E+01	$tanb$
1.500E+02	$M_1(MX)$
2.500E+02	$M_2(MX)$
1.200E+03	$M_3(MX)$
4.000E+03	$At(MX)$
4.000E+03	$Ab(MX)$
0.000E+00	$Atau(MX)$
1.500E+03	$mu(MX)$
1.500E+03	$mA(pole)$
1.000E+03	$meL(MX)$
1.000E+03	$mmuL(MX)$
1.000E+03	$mtauL(MX)$
2.000E+02	$meR(MX)$
2.000E+02	$mmuR(MX)$
1.000E+03	$mtauR(MX)$
1.000E+03	$mqL1(MX)$
1.000E+03	$mqL2(MX)$
1.000E+03	$mqL3(MX)$
1.000E+03	$muR(MX)$
1.000E+03	$mcR(MX)$
4.000E+03	$mtR(MX)$
1.000E+03	$mdR(MX)$
1.000E+03	$msR(MX)$
1.000E+03	$mbR(MX)$

mass	particle
8.040E+01	$W+$
1.255E+02	h
1.500E+03	H
1.499E+03	A
1.501E+03	$H+$
4.878E+00	m_b
1.076E+03	d_L
1.073E+03	d_R
1.073E+03	u_L
1.076E+03	u_R
1.076E+03	s_L
1.073E+03	s_R
1.073E+03	c_L
1.076E+03	c_R
1.067E+03	b_1
1.119E+03	b_2
1.116E+03	t_1
4.007E+03	t_2
1.005E+03	e_L
1.846E+02	e_R
1.001E+03	nu_eL
1.005E+03	mu_L
1.846E+02	mu_R
1.001E+03	nu_muL

mass	particle
9.875E+02	tau_1
1.014E+03	tau_2
1.001E+03	nu_tauL
1.277E+03	g
1.464E+02	chi_10
2.598E+02	chi_20
-1.503E+03	chi_30
1.505E+03	chi_40
2.600E+02	chi_1+
1.506E+03	chi_2+

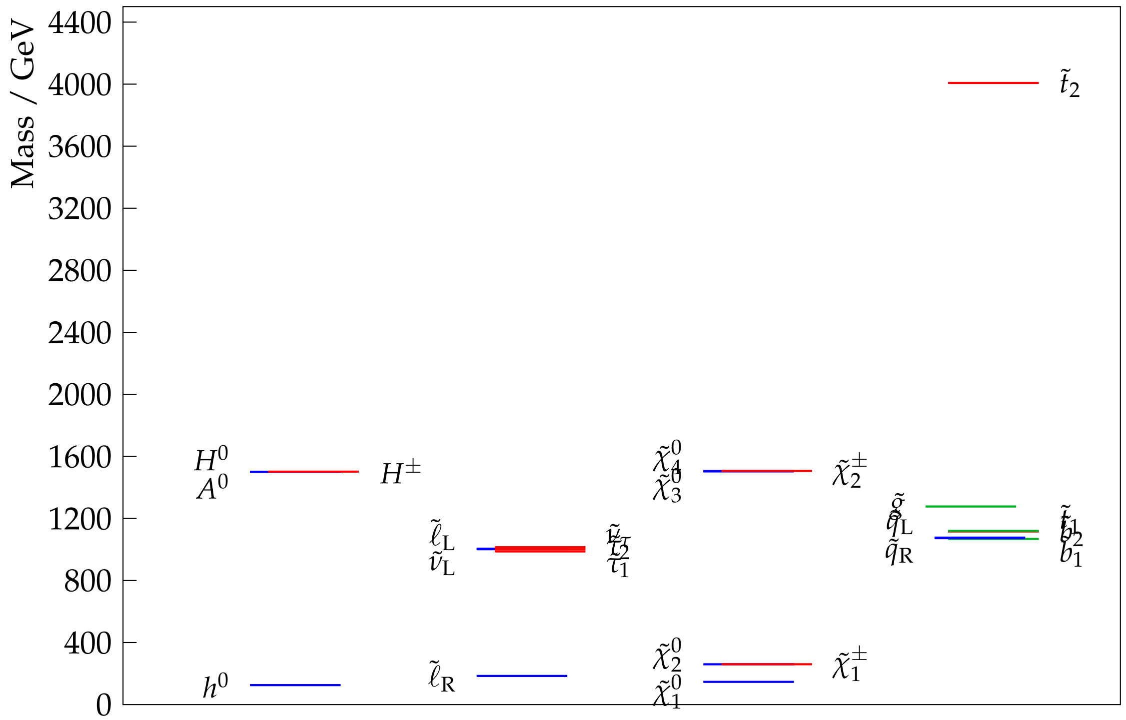

pMSSM scenario under investigation in Chapter 3.

Bibliography

[1] S. Glashow, "Partial Symmetries of Weak Interactions," *Nucl.Phys.*, vol. 22, pp. 579–588, 1961.

[2] S. Weinberg, "A Model of Leptons," *Phys.Rev.Lett.*, vol. 19, pp. 1264–1266, 1967.

[3] A. Salam, "Weak and Electromagnetic Interactions," *Conf.Proc.*, vol. C680519, pp. 367–377, 1968.

[4] G. Arnison *et al.*, "Experimental Observation of Isolated Large Transverse Energy Electrons with Associated Missing Energy at s**(1/2) = 540-GeV," *Phys.Lett.*, vol. B122, pp. 103–116, 1983.

[5] G. Arnison *et al.*, "Experimental Observation of Lepton Pairs of Invariant Mass Around 95-GeV/c**2 at the CERN SPS Collider," *Phys.Lett.*, vol. B126, pp. 398–410, 1983.

[6] G. Aad *et al.*, "Observation of a new particle in the search for the Standard Model Higgs boson with the ATLAS detector at the LHC," 2012, 1207.7214.

[7] S. Chatrchyan *et al.*, "Observation of a new boson at a mass of 125 GeV with the CMS experiment at the LHC," *Phys.Lett.B*, 2012, 1207.7235.

[8] P. W. Higgs, "Broken Symmetries and the Masses of Gauge Bosons," *Phys.Rev.Lett.*, vol. 13, pp. 508–509, 1964.

[9] F. Englert and R. Brout, "Broken Symmetry and the Mass of Gauge Vector Mesons," *Phys.Rev.Lett.*, vol. 13, pp. 321–323, 1964.

[10] G. Guralnik, C. Hagen, and T. Kibble, "Global Conservation Laws and Massless Particles," *Phys.Rev.Lett.*, vol. 13, pp. 585–587, 1964.

[11] N. Jarosik, C. Bennett, J. Dunkley, B. Gold, M. Greason, *et al.*, "Seven-Year Wilkinson Microwave Anisotropy Probe (WMAP) Observations: Sky Maps, Systematic Errors, and Basic Results," *Astrophys.J.Suppl.*, vol. 192, p. 14, 2011, 1001.4744.

[12] E. Komatsu *et al.*, "Seven-Year Wilkinson Microwave Anisotropy Probe (WMAP) Observations: Cosmological Interpretation," *Astrophys.J.Suppl.*, vol. 192, p. 18, 2011, 1001.4538.

[13] D. Clowe, M. Bradac, A. H. Gonzalez, M. Markevitch, S. W. Randall, *et al.*, "A direct empirical proof of the existence of dark matter," *Astrophys.J.*, vol. 648, pp. L109–L113, 2006, astro-ph/0608407.

[14] N. Arkani-Hamed, A. G. Cohen, and H. Georgi, "Electroweak symmetry breaking from dimensional deconstruction," *Phys.Lett.*, vol. B513, pp. 232–240, 2001, hep-ph/0105239.

[15] N. Arkani-Hamed, A. G. Cohen, T. Gregoire, and J. G. Wacker, "Phenomenology of electroweak symmetry breaking from theory space," *JHEP*, vol. 0208, p. 020, 2002, hep-ph/0202089.

[16] Y. Golfand and E. Likhtman, "Extension of the Algebra of Poincare Group Generators and Violation of p Invariance," *JETP Lett.*, vol. 13, pp. 323–326, 1971.

[17] D. Volkov and V. Akulov, "Is the Neutrino a Goldstone Particle?," *Phys.Lett.*, vol. B46, pp. 109–110, 1973.

[18] J. Wess and B. Zumino, "Supergauge Transformations in Four-Dimensions," *Nucl.Phys.*, vol. B70, pp. 39–50, 1974.

[19] R. Haag, J. T. Lopuszanski, and M. Sohnius, "All Possible Generators of Supersymmetries of the s Matrix," *Nucl.Phys.*, vol. B88, p. 257, 1975.

[20] M. A. Luty, "2004 TASI lectures on supersymmetry breaking," pp. 495–582, 2005, hep-th/0509029.

[21] S. P. Martin, "A Supersymmetry primer," 1997, hep-ph/9709356.

[22] J. L. Hewett and M. Spiropulu, "Particle physics probes of extra space-time dimensions," *Ann.Rev.Nucl.Part.Sci.*, vol. 52, pp. 397–424, 2002, hep-ph/0205106.

[23] C. Csaki, “TASI lectures on extra dimensions and branes,” pp. 605–698, 2004, hep-ph/0404096.

[24] N. Arkani-Hamed, S. Dimopoulos, and G. Dvali, “The Hierarchy problem and new dimensions at a millimeter,” *Phys.Lett.*, vol. B429, pp. 263–272, 1998, hep-ph/9803315.

[25] I. Antoniadis, N. Arkani-Hamed, S. Dimopoulos, and G. Dvali, “New dimensions at a millimeter to a Fermi and superstrings at a TeV,” *Phys.Lett.*, vol. B436, pp. 257–263, 1998, hep-ph/9804398.

[26] N. Arkani-Hamed, S. Dimopoulos, and G. Dvali, “Phenomenology, astrophysics and cosmology of theories with submillimeter dimensions and TeV scale quantum gravity,” *Phys.Rev.*, vol. D59, p. 086004, 1999, hep-ph/9807344.

[27] T. Kaluza, “On the Problem of Unity in Physics,” *Sitzungsber.Preuss.Akad.Wiss.Berlin (Math.Phys.)*, vol. 1921, pp. 966–972, 1921.

[28] O. Klein, “Quantum Theory and Five-Dimensional Theory of Relativity. (In German and English),” *Z.Phys.*, vol. 37, pp. 895–906, 1926.

[29] T. Appelquist, H.-C. Cheng, and B. A. Dobrescu, “Bounds on universal extra dimensions,” *Phys.Rev.*, vol. D64, p. 035002, 2001, hep-ph/0012100.

[30] H.-C. Cheng, K. T. Matchev, and M. Schmaltz, “Radiative corrections to Kaluza-Klein masses,” *Phys.Rev.*, vol. D66, p. 036005, 2002, hep-ph/0204342.

[31] H.-C. Cheng, K. T. Matchev, and M. Schmaltz, “Bosonic supersymmetry? Getting fooled at the CERN LHC,” *Phys.Rev.*, vol. D66, p. 056006, 2002, hep-ph/0205314.

[32] N. Arkani-Hamed, H.-C. Cheng, B. A. Dobrescu, and L. J. Hall, “Selfbreaking of the standard model gauge symmetry,” *Phys.Rev.*, vol. D62, p. 096006, 2000, hep-ph/0006238.

[33] M. Drees, R. Godbole, and P. Roy, “Theory and phenomenology of sparticles: An account of four-dimensional N=1 supersymmetry in high energy physics,” 2004.

[34] H. Baer and X. Tata, “Weak scale supersymmetry: From superfields to scattering events,” 2006.

[35] G. R. Farrar and P. Fayet, “Phenomenology of the Production, Decay, and Detection of New Hadronic States Associated with Supersymmetry,” *Phys.Lett.*, vol. B76, pp. 575–579, 1978.

[36] P. Fayet and J. Iliopoulos, “Spontaneously Broken Supergauge Symmetries and Goldstone Spinors,” *Phys.Lett.*, vol. B51, pp. 461–464, 1974.

[37] L. O’Raifeartaigh, “Spontaneous Symmetry Breaking for Chiral Scalar Superfields,” *Nucl.Phys.*, vol. B96, p. 331, 1975.

[38] E. Witten, “Dynamical Breaking of Supersymmetry,” *Nucl.Phys.*, vol. B188, p. 513, 1981.

[39] A. Barr, “Determining the spin of supersymmetric particles at the LHC using lepton charge asymmetry,” *Phys.Lett.*, vol. B596, pp. 205–212, 2004, hep-ph/0405052.

[40] J. M. Smillie and B. R. Webber, “Distinguishing spins in supersymmetric and universal extra dimension models at the large hadron collider,” *JHEP*, vol. 0510, p. 069, 2005, hep-ph/0507170.

[41] A. Alves, O. Eboli, and T. Plehn, “It’s a gluino,” *Phys.Rev.*, vol. D74, p. 095010, 2006, hep-ph/0605067.

[42] A. Barr, “Measuring slepton spin at the LHC,” *JHEP*, vol. 0602, p. 042, 2006, hep-ph/0511115.

[43] G. Moortgat-Pick, K. Rolbiecki, and J. Tattersall, “Early spin determination at the LHC?,” *Phys.Lett.*, vol. B699, pp. 158–163, 2011, 1102.0293.

[44] G. L. Kane, A. A. Petrov, J. Shao, and L.-T. Wang, “Initial determination of the spins of the gluino and squarks at LHC,” *J.Phys.G*, vol. G37, p. 045004, 2010, 0805.1397.

[45] K. Hagiwara, W. Kilian, F. Krauss, T. Ohl, T. Plehn, *et al.*, “Supersymmetry simulations with off-shell effects for CERN LHC and ILC,” *Phys.Rev.*, vol. D73, p. 055005, 2006, hep-ph/0512260.

[46] D. Berdine, N. Kauer, and D. Rainwater, “Breakdown of the Narrow Width Approximation for New Physics,” *Phys.Rev.Lett.*, vol. 99, p. 111601, 2007, hep-ph/0703058.

[47] A. J. Barr and C. G. Lester, “A Review of the Mass Measurement Techniques proposed for the Large Hadron Collider,” *J.Phys.G*, vol. G37, p. 123001, 2010, 1004.2732.

[48] L.-T. Wang and I. Yavin, “A Review of Spin Determination at the LHC,” *Int.J.Mod.Phys.*, vol. A23, pp. 4647–4668, 2008, 0802.2726.

[49] B. Allanach, C. Lester, M. A. Parker, and B. Webber, “Measuring sparticle masses in nonuniversal string inspired models at the LHC,” *JHEP*, vol. 0009, p. 004, 2000, hep-ph/0007009.

[50] C. G. Lester, “Model independent sparticle mass measurements at ATLAS,” 2001.

[51] B. Gjelsten, . Miller, D.J., and P. Osland, “Measurement of SUSY masses via cascade decays for SPS 1a,” *JHEP*, vol. 0412, p. 003, 2004, hep-ph/0410303.

[52] B. Gjelsten, . Miller, D.J., and P. Osland, “Measurement of the gluino mass via cascade decays for SPS 1a,” *JHEP*, vol. 0506, p. 015, 2005, hep-ph/0501033.

[53] A. Rajaraman and F. Yu, “A New Method for Resolving Combinatorial Ambiguities at Hadron Colliders,” *Phys.Lett.*, vol. B700, pp. 126–132, 2011, 1009.2751.

[54] P. Baringer, K. Kong, M. McCaskey, and D. Noonan, “Revisiting Combinatorial Ambiguities at Hadron Colliders with M_{T2},” *JHEP*, vol. 1110, p. 101, 2011, 1109.1563.

[55] K. Choi, D. Guadagnoli, and C. B. Park, “Reducing combinatorial uncertainties: A new technique based on MT2 variables,” *JHEP*, vol. 1111, p. 117, 2011, 1109.2201.

[56] C. Lester and D. Summers, “Measuring masses of semiinvisibly decaying particles pair produced at hadron colliders,” *Phys.Lett.*, vol. B463, pp. 99–103, 1999, hep-ph/9906349.

[57] W. S. Cho, K. Choi, Y. G. Kim, and C. B. Park, “Gluino Stransverse Mass,” *Phys.Rev.Lett.*, vol. 100, p. 171801, 2008, 0709.0288.

[58] M. M. Nojiri, Y. Shimizu, S. Okada, and K. Kawagoe, “Inclusive transverse mass analysis for squark and gluino mass determination,” *JHEP*, vol. 0806, p. 035, 2008, 0802.2412.

[59] G. Bayatian *et al.*, “CMS technical design report, volume II: Physics performance,” *J.Phys.G*, vol. G34, pp. 995–1579, 2007.

[60] J. Alwall, K. Hiramatsu, M. M. Nojiri, and Y. Shimizu, “Novel reconstruction technique for New Physics processes with initial state radiation,” *Phys.Rev.Lett.*, vol. 103, p. 151802, 2009, 0905.1201.

[61] D. Curtin, “Mixing It Up With MT2: Unbiased Mass Measurements at Hadron Colliders,” *Phys.Rev.*, vol. D85, p. 075004, 2012, 1112.1095.

[62] J. Reuter and D. Wiesler, “A Fat Gluino in Disguise,” 2012, 1212.5559.

[63] C. Uhlemann, “Narrow-width approximation in the Minimal Supersymmetric Standard Model,” *Diploma thesis*, 2007.

[64] A. Denner, S. Dittmaier, M. Roth, and L. Wieders, “Complete electroweak O(alpha) corrections to charged-current e+e- 4 fermion processes,” *Phys.Lett.*, vol. B612, pp. 223–232, 2005, hep-ph/0502063.

[65] J. Reuter, W. Kilian, K. Hagiwara, F. Krauss, S. Schumann, *et al.*, “Next generation multi-particle event generators for the MSSM,” 2005, hep-ph/0512012.

[66] N. Kauer, “A Threshold-improved narrow-width approximation for BSM physics,” *JHEP*, vol. 0804, p. 055, 2008, 0708.1161.

[67] C. Uhlemann and N. Kauer, “Narrow-width approximation accuracy,” *Nucl.Phys.*, vol. B814, pp. 195–211, 2009, 0807.4112.

[68] B. Allanach, M. Battaglia, G. Blair, M. S. Carena, A. De Roeck, *et al.*, “The Snowmass points and slopes: Benchmarks for SUSY searches,” *Eur.Phys.J.*, vol. C25, pp. 113–123, 2002, hep-ph/0202233.

[69] B. Allanach, “SOFTSUSY: a program for calculating supersymmetric spectra,” *Comput.Phys.Commun.*, vol. 143, pp. 305–331, 2002, hep-ph/0104145.

[70] A. Djouadi, M. Muhlleitner, and M. Spira, “Decays of supersymmetric particles: The Program SUSY-HIT (SUspect-SdecaY-Hdecay-InTerface),” *Acta Phys.Polon.*, vol. B38, pp. 635–644, 2007, hep-ph/0609292.

[71] B. Allanach, C. Balazs, G. Belanger, M. Bernhardt, F. Boudjema, *et al.*, “SUSY Les Houches Accord 2,” *Comput.Phys.Commun.*, vol. 180, pp. 8–25, 2009, 0801.0045.

[72] W. Beenakker, R. Hopker, M. Spira, and P. Zerwas, "Squark and gluino production at hadron colliders," *Nucl.Phys.*, vol. B492, pp. 51–103, 1997, hep-ph/9610490.

[73] M. Moretti, T. Ohl, and J. Reuter, "O'Mega: An Optimizing matrix element generator," 2001, hep-ph/0102195.

[74] W. Kilian, T. Ohl, and J. Reuter, "WHIZARD: Simulating Multi-Particle Processes at LHC and ILC," *Eur.Phys.J.*, vol. C71, p. 1742, 2011, 0708.4233.

[75] M. Dobbs and J. B. Hansen, "The HepMC C++ Monte Carlo event record for High Energy Physics," *Comput.Phys.Commun.*, vol. 134, pp. 41–46, 2001.

[76] I. Antcheva, M. Ballintijn, B. Bellenot, M. Biskup, R. Brun, *et al.*, "ROOT: A C++ framework for petabyte data storage, statistical analysis and visualization," *Comput.Phys.Commun.*, vol. 182, pp. 1384–1385, 2011.

[77] C. Lester and A. Barr, "MTGEN : Mass scale measurements in pair-production at colliders," *JHEP*, vol. 12, p. 102, 2007, 0708.1028.

[78] N. D. Christensen and C. Duhr, "FeynRules - Feynman rules made easy," *Comput.Phys.Commun.*, vol. 180, pp. 1614–1641, 2009, 0806.4194.

[79] N. D. Christensen, C. Duhr, B. Fuks, J. Reuter, and C. Speckner, "Introducing an interface between WHIZARD and FeynRules," *Eur.Phys.J.*, vol. C72, p. 1990, 2012, 1010.3251.

[80] N. Pietsch, J. Reuter, K. Sakurai, and D. Wiesler, "Extracting gluino endpoints with event topology patterns," *JHEP*, vol. 1207, p. 148, 2012, 1206.2146.

[81] S. Heinemeyer, O. Stal, and G. Weiglein, "Interpreting the LHC Higgs Search Results in the MSSM," *Phys.Lett.*, vol. B710, pp. 201–206, 2012, 1112.3026.

[82] T. Plehn, D. Rainwater, and P. Z. Skands, "Squark and gluino production with jets," *Phys.Lett.*, vol. B645, pp. 217–221, 2007, hep-ph/0510144.

[83] M. M. Nojiri and K. Sakurai, "Controlling ISR in sparticle mass reconstruction," *Phys.Rev.*, vol. D82, p. 115026, 2010, 1008.1813.

[84] B. Dutta, T. Kamon, N. Kolev, and A. Krislock, "Bi-Event Subtraction Technique at Hadron Colliders," *Phys.Lett.*, vol. B703, pp. 475–478, 2011, 1104.2508.

[85] M. Bahr, S. Gieseke, M. Gigg, D. Grellscheid, K. Hamilton, *et al.*, "Herwig++ Physics and Manual," *Eur.Phys.J.*, vol. C58, pp. 639–707, 2008, 0803.0883.

[86] S. Ovyn, X. Rouby, and V. Lemaitre, "DELPHES, a framework for fast simulation of a generic collider experiment," 2009, 0903.2225.

[87] S. Chatrchyan *et al.*, "Search for New Physics with Jets and Missing Transverse Momentum in pp collisions at sqrt(s) = 7 TeV," *JHEP*, vol. 1108, p. 155, 2011, 1106.4503.

[88] N. Pietsch, "Search for Supersymmetry in Final States with Single Leptons and B-jets at the CMS-Experiment," *PhD thesis*, 2013.

[89] G. Aad *et al.*, "Search for new phenomena in final states with large jet multiplicities and missing transverse momentum using sqrt(s)=7 TeV pp collisions with the ATLAS detector," *JHEP*, vol. 1111, p. 099, 2011, 1110.2299.

[90] S. Chatrchyan *et al.*, "Search for supersymmetry in pp collisions at sqrt(s)=7 TeV in events with a single lepton, jets, and missing transverse momentum," *JHEP*, vol. 1108, p. 156, 2011, 1107.1870.

[91] Y. Bai and H.-C. Cheng, "Identifying Dark Matter Event Topologies at the LHC," *JHEP*, vol. 1106, p. 021, 2011, 1012.1863.

[92] J. L. Hewett and T. G. Rizzo, "Low-Energy Phenomenology of Superstring Inspired E(6) Models," *Phys.Rept.*, vol. 183, p. 193, 1989.

[93] J. Reuter and D. Wiesler, "Distorted mass edges at LHC from supersymmetric leptoquarks," *Phys.Rev.*, vol. D84, p. 015012, 2011, 1010.4215.

[94] W. Kilian and J. Reuter, "Unification without doublet-triplet splitting," *Phys.Lett.*, vol. B642, pp. 81–84, 2006, hep-ph/0606277.

[95] F. Braam, J. Reuter, and D. Wiesler, "The Pati-Salam Supersymmetric SM (PSSSM)," *AIP Conf.Proc.*, vol. 1200, pp. 458–461, 2010, 0909.3081.

[96] P. Athron, S. King, D. Miller, S. Moretti, and R. Nevzorov, "The Constrained Exceptional Supersymmetric Standard Model," *Phys.Rev.*, vol. D80, p. 035009, 2009, 0904.2169.

[97] F. Braam, A. Knochel, and J. Reuter, "An Exceptional SSM from E6 Orbifold GUTs with intermediate LR symmetry," *JHEP*, vol. 1006, p. 013, 2010, 1001.4074.

[98] F. K. Braam, "A supersymmetric standard model from a local E_6 GUT," *PhD thesis*, 2012.

[99] J. A. Aguilar-Saavedra, A. Ali, B. C. Allanach, R. L. Arnowitt, H. A. Baer, *et al.*, "Supersymmetry parameter analysis: SPA convention and project," *Eur.Phys.J.*, vol. C46, pp. 43–60, 2006, hep-ph/0511344.

[100] J. Kang, P. Langacker, and B. D. Nelson, "Theory and Phenomenology of Exotic Isosinglet Quarks and Squarks," *Phys.Rev.*, vol. D77, p. 035003, 2008, 0708.2701.

[101] D. Wiesler, "LHC-phenomenology of Leptoquarks in a Pati-Salam SUSY GUT," *Diploma thesis*, 2009.

[102] W. Porod, "SPheno, a program for calculating supersymmetric spectra, SUSY particle decays and SUSY particle production at e+ e- colliders," *Comput.Phys.Commun.*, vol. 153, pp. 275–315, 2003, hep-ph/0301101.

[103] S. Chatrchyan *et al.*, "Search for new physics in the multijet and missing transverse momentum final state in proton-proton collisions at $\sqrt{s} = 7$ TeV," 2012, 1207.1898.

[104] S. Chatrchyan *et al.*, "Search for supersymmetry in hadronic final states using MT2 in pp collisions at $\sqrt{s} = 7$ TeV," 2012, 1207.1798.

[105] G. Aad *et al.*, "Search for squarks and gluinos using final states with jets and missing transverse momentum with the ATLAS detector in sqrt(s) = 7 TeV proton-proton collisions," *Phys.Lett.*, vol. B710, pp. 67–85, 2012, 1109.6572.

[106] V. Khachatryan *et al.*, "Search for Pair Production of First-Generation Scalar Leptoquarks in pp Collisions at sqrt(s) = 7 TeV," *Phys.Rev.Lett.*, vol. 106, p. 201802, 2011, 1012.4031.

[107] S. Chatrchyan *et al.*, "Search for First Generation Scalar Leptoquarks in the evjj channel in pp collisions at sqrt(s) = 7 TeV," *Phys.Lett.*, vol. B703, pp. 246–266, 2011, 1105.5237.

[108] G. Aad *et al.*, "Search for first generation scalar leptoquarks in pp collisions at sqrts=7 TeV with the ATLAS detector," *Phys.Lett.*, vol. B709, pp. 158–176, 2012, 1112.4828.

[109] G. Aad *et al.*, "Search for pair production of a new quark that decays to a Z boson and a bottom quark with the ATLAS detector," *Phys.Rev.Lett.*, vol. 109, p. 071801, 2012, 1204.1265.

Acknowledgments

First and foremost I would like to thank my supervisor Dr. Jürgen Reuter for invaluable discussions, helpful support and the opportunity to pursue my PhD studies in three different very inspiring places. Furthermore I would like to thank Prof. Dr. Gudrid Moortgat-Pick for acting as the second examiner of this thesis and Prof. Dr. Peter Schleper for acting as the second referee of my defense.

For many enlightening insights and fruitful collaborations I would like to thank Dr. Felix Braam, Dr. Alexander Knochel, Dr. Sebastian Schmidt and Niklas Pietsch. Additionally I would like to thank Christoph Horst and Sarah Andreas for careful proof-reading of the manuscript. Further thanks go to JProf. Dr. Christian Sander and Dr. Matthias Schröder from the CMS group of Hamburg University for helpful comments and in particular to Dr. Kazuki Sakurai for providing me with lots of support and parts of code, which made my life a lot easier! Many thanks are also in place for the theory groups in Freiburg, Edinburgh and DESY Hamburg for a warm hospitality and nice working atmospheres, e.g. the delicious Franzbrötchen and coffee breaks with Elina Fuchs, Vaclav Tlapak and Valerie Domcke.

Last but the opposite of least I am deeply in debt to my family, my friends and especially to Hanna, who supported me in many ways during the time of preparation of this thesis.